Constraining Variations in the Stellar Initial Mass Function with the Fornax3D Survey

By

Bronwyn Reichardt Chu

A thesis submitted to Macquarie University

for the degree of Master of Research

Department of Physics and Astronomy

December 2018

MACQUARIE
University
SYDNEY·AUSTRALIA

Typeset in $\LaTeX\,2_\varepsilon$.

Except where acknowledged in the customary manner, the material presented in this thesis is, to the best of my knowledge, original and has not been submitted in whole or part for a degree in any university.

Reichardt

Bronwyn Reichardt Chu

Acknowledgements

I would like to thank:

My supervisor, Richard McDermid, for being an awesome supervisor, providing a myriad of beautifully worded comments, and giving me an opportunity to remember how much I love Munich.

The Fornax3D team for providing the reduced data used within this thesis.

Nacho Martín-Navarro, without whom a large part of the third chapter would not be possible, for a huge amount of help, friendly chats and advice.

Glenn van de Ven and Mariya Lyubenova for hosting me at ESO, and for being generally helpful and encouraging in the middle of a very busy summer.

My husband Terence, for keeping me well fed, and for reminding me that the outside world does still exist.

My family, for (pretending to be) interested in what I was doing, and for attempting to understand even a small part, even if they do still think IMF stands for 'International Monetary Fund'.

Abstract

The stellar initial mass function (IMF) describes the distribution of stellar masses when a population of stars first forms. It is a particularly crucial property connecting many different phenomena within a galaxy. Defining the IMF of a galaxy is therefore critical for helping us to understand how galaxies evolve over cosmic time. However, defining the IMF has been the subject of vigorous debate over the past few decades. Recent evidence from early-type galaxies which appear to become more dwarf star rich as galactic mass increases supports a variable rather than universal IMF. With improvements in technology, the question of whether the IMF varies spatially within galaxies has also begun to be investigated, with no clear result as yet. This thesis presents preliminary results from the Fornax3D survey using the MUSE integral field spectrograph. Two techniques for finding the IMF are compared here for the lenticular galaxy FCC167: full spectral fitting, and a more constrained approach focusing on a few key features. While the two methods agree reasonably well on radial variations for the age and abundance parameters in common, the derived IMF shape and its variation within the galaxy differ.

Contents

'Begin at the beginning,' the King said, very gravely, 'and go on till you come to the end: then stop.'

Lewis Carroll, Alice in Wonderland

1

Introduction

1.1 A (Brief) History of the IMF

The first paper introducing the idea of an Initial Mass Function was that of E.E. Salpeter, a theoretical nuclear physicist. Salpeter recalls the circumstances and motivations 50 years later at a conference celebrating his work (Salpeter 2005). With a book to write (which he never finished) about nuclear energy production within stars, mainly focused on nuclear physics with a little basic astronomy to explain the context, Salpeter had to teach the basic astronomy to himself. At the 1953 Ann Arbor Summer School George Gamow remarked that "not enough stars have contributed much to interstellar matter during the age of the universe. The interstellar matter is of original pre-stellar matter". The inference was that all of the elements up to iron had to have been formed during the Big Bang nucleosynthesis. Salpeter did not agree. He had an intuition that the birth-rate of massive main sequence stars was high enough and their lifetimes short enough to produce medium and heavy elements in the quantities we now observe in the Interstellar Medium (ISM). Motivated by this, Salpeter defined a relation for the number of stars in each mass bin at their birth (Salpeter 2005).

The "original mass function" was defined by Salpeter (1955) as:

$$dN = \xi(M) d(\log_{10} M) \frac{dt}{T_0} \tag{1.1}$$

where dN is the number of stars created in time dt within the mass range dM, for each cubic parsec. $\xi(M)$ is the original mass function, such that:

$$\xi(M) = \frac{dN}{d\log_{10} M} \propto M^{-\Gamma} \tag{1.2}$$

Salpeter (1955) based his equation on empirical functions describing the luminosity and spectral class of an extensive observational database of stars. Salpeter drew his luminosity function from the early observational work done by van Rhijn (1925, 1936), Luyten (1941) and others, summarised in Trumpler & Weaver (1953). From the empirical luminosity function, the mass and bolometric luminosity of stars can be calculated, and a mass function created. Salpeter (1955) counted only main sequence stars and assumed that there are no stars older than the galaxy and that all stars above a limiting luminosity M_L have burnt through 12% of their mass and have moved off of the main sequence. Using these assumptions, he was able to calculate the mass function given in Eq. 1.1. Salpeter (1955) approximated the logarithmic original mass function for stars between 0.4 and 10$M_\odot$ as:

$$\xi(M) \approx 0.03(\frac{M}{M_\odot})^{-\Gamma} = 0.03(\frac{M}{M_\odot})^{-1.35} \tag{1.3}$$

This equation can also be written in a linear form:

$$\Xi(m) = \frac{dN}{dm} \propto m^{-\alpha} \tag{1.4}$$

where $\alpha = \Gamma + 1$, such that a Salpeter IMF has $\alpha = 2.35$.

Despite Salpeter's emphasis on the limitations and inaccuracies of his calculations in both his original (Salpeter 1955) paper and his 50th anniversary seminar (Salpeter 2005), the Salpeter Original or Initial Mass Function (IMF) is still one of the major IMF forms in use today.

Following Salpeter (1955), at least three separate papers tested his original luminosity function. The luminosity function is the foundation of Salpeter's IMF and is the most easily observationally testable part of his theory. Jaschek & Jaschek (1957), Sandage (1957) and van den Bergh (1957) all used open clusters to find luminosity distributions which agreed well with the distribution Salpeter found using field stars. Open clusters form all of their stars at once and can be assumed to have the same luminosity function as when they were originally formed, making them ideal testing grounds for an IMF. In the same year, Sandage (1957) extended the luminosity function from stars between -4 and 13 M_v (Salpeter 1955) to include stars between -6 and 20 M_v. This extension allowed Warner (1961) to extend Salpeter's IMF to lower and higher stellar masses. Warner found an IMF that agreed well with Salpeter's, although differing somewhat at low and high masses. He suggested that Salpeter's law might be the fundamental law, working well for stellar masses between 0.25 and 10$M_\odot$. Outside these ranges, Warner proposed that different physics may contribute to star formation, producing a different IMF shape.

Further investigation into Salpeter's IMF over the next couple of decades was motivated by the various subfields of astrophysics in which it is useful. The papers in which it is tested and developed were generally written with another aim in mind, and the IMF as a side point. For example, Schmidt (1959) utilised Salpeter's luminosity function and IMF in his work on the relationship between interstellar gas density and the Star Formation Rate (SFR). He found that if gas density is related to the SFR, as long as you know the gas density, you don't need a constant birthrate such as Salpeter assumed to find the Salpeter IMF. Searle & Sargent (1972) considered how changing the shape of the IMF would change the rate at which a galaxy produces elements, using this to investigate two dwarf galaxies that were discovered to be bluer and smaller than expected. They suggested that either the galaxies follow a Salpeter IMF and are now undergoing a burst of star formation; or the galaxies do not follow a Salpeter IMF and instead have a top-heavy IMF (more high mass stars than expected). Shields & Tinsley (1976) investigate the temperature and metallicity gradients across a galaxy, and whether these have an effect on the upper star formation mass limit. Changes in the IMF would change the number of ionising stars, and therefore their contribution to the observed luminosity. They conclude that there may well be a connection between IMF shape and metallicity as well as the connection between metallicity and upper mass limit. These are just three examples of how research into the IMF was continued as an incidental issue.

Star counts have played a formative part in observational research into the IMF, particularly during the first few decades. A study done by Becker et al. (1977) counted more long-period Cepheids in the Milky Way, Magellanic Clouds and M31 than predicted from a Salpeter IMF. They suggested that since Salpeter used the solar neighbourhood population of low-mass, old stars to formulate his IMF, it may misrepresent the number of high mass stars in the rest of the galaxy. The extra observed high-mass stars could be explained by a two-component function of the IMF, which would predict more of them than Salpeter's original one-component function. Applying star counts to field stars to study elemental abundance ratios, Tinsley (1977) found that using a model with a constant IMF predicted more stars with a lower metallicity than was observed. An IMF with more than one component was also needed to predict her observations. In contrast to these results, Lequeux (1979) found that there was no evidence that the IMF would differ strongly between the Magellanic Clouds and the solar neighbourhood, in good agreement with a Salpeter IMF. Dennefeld & Tammann (1980) had results that support this conclusion for high mass stars, finding a similar IMF to Salpeter even though Salpeter found the IMF using main sequence stars, not high mass stars. The astronomical community was split over whether or not Salpeter's IMF fit the observational data.

The shape and slope of the IMF became a greater topic for investigation in the 1970's. There was a general movement towards dividing the IMF into components dependent on mass. Low-mass stars have lifetimes longer than the age of the galaxy, and so their numbers are not reliant on current star formation rates. High-mass stars live fast and die young, so the high-mass stars we observe have formed relying on the current star formation rate. This means that an IMF calculated from star counts will be proportional to the present star formation rate at high masses, and proportional to the average past star formation rate for lower masses. Summarising recent observational data at the time, Audouze & Tinsley (1976) suggested a steeper than Salpeter (1955) slope for the upper IMF and a shallower slope for the lower IMF, with $2\mathrm{M}_\odot$ as the dividing mass. Later, Tinsley (1977) derived a three-component power law using data from Wielen (1974) and Burki (1977). She required that the IMF did not change abruptly between 1 and $2\mathrm{M}_\odot$, and defined it as:

$$\Gamma = \begin{cases} 0.25 & 0.7\mathrm{M}_\odot \leq m < 1\mathrm{M}_\odot \\ 1.0 & 1\mathrm{M}_\odot \leq m < 2\mathrm{M}_\odot \\ 1.3 & 2\mathrm{M}_\odot \leq m < 50\mathrm{M}_\odot \end{cases} \tag{1.5}$$

where Γ is the slope of the IMF as in Equation 1.2, and m is the mass of the stars in $\mathrm{M}_\odot$. This definition of the IMF was one of the first attempts to prevent it from being discontinuous and yet still have more than one component. Discontinuity had been caused in previous attempts by counting both low mass stars, which are not affected by current star formation rates; and high mass stars, which are reliant on current star formation rates. The break generally occurs between 1 and $2\mathrm{M}_\odot$, which is where Tinsley (1977) enforced continuity. Soon after this, Miller & Scalo (1979) reviewed the field with the purpose of redetermining the IMF in the solar neighbourhood. After reviewing observational data up to that date, they found the best fit to be a three-component power law with the slopes:

$$\Gamma = \begin{cases} 0.4 & 0.1\mathrm{M}_\odot \leq m < 1\mathrm{M}_\odot \\ 1.5 & 1\mathrm{M}_\odot \leq m < 10\mathrm{M}_\odot \\ 2.3 & m \geq 10\mathrm{M}_\odot \end{cases} \tag{1.6}$$

This approximation of the IMF roughly agrees with a Salpeter IMF between 1 and 10$\mathrm{M}_\odot$, but predicts a steeper upper IMF and a shallower lower IMF. Overall it is steeper than Tinsley's IMF (Eq. 1.5) and closer to Salpeter's original IMF (Eq. 1.3). Tinsley (1981) added to the discussion again a few years later, suggesting that the Salpeter IMF should not be extrapolated below 0.1$\mathrm{M}_\odot$ to predict low mass substellar objects. This is now known as the 'low-mass cut-off', and its value is still uncertain. The work by Tinsley (1977) and in particular Miller & Scalo (1979) constrained the IMF in mass ranges beyond Salpeter's original limits and showed that the slope of the IMF does change with stellar mass.

As the use of CCDs in astronomical instrumentation was developed in the late 1970s and larger telescopes were built, the ability of astronomers to investigate the IMF beyond our own galaxy also developed. Spectroscopy began to be utilised as a tool to look at galaxies where individual stars cannot be resolved. Comparing UBV colours of disk galaxies, Searle et al. (1973) and Larson & Tinsley (1978) both found that a Salpeter-like IMF best fit the luminosity functions that they observed. Although they found no evidence for large variations in the IMF, Larson & Tinsley (1978) discuss how variations in the upper IMF slope would affect a galaxy's UBV colours, expecting galaxies with a steeper IMF to be redder. A steep IMF slope implies less high mass stars, producing a galaxy with a lower temperature and therefore appearing redder. Observing this effect would rely on finding galaxies of similar ages with varying IMFs as young star-forming galaxies naturally appear far bluer than old quenched galaxies.

Improvements in observational technology also offered more opportunities for disagreement. The development of astronomical instruments allowed Kennicutt Jr (1983) to observe HII regions in other galaxies, and use these as tracers of star formation providing the star formation rate. Kennicutt Jr compared three different IMFs when fitting his data: the Miller & Scalo (1979) review IMF; an extended version similar to Salpeter (1955); and a shallow (top-heavy) IMF. He disagreed with the Miller & Scalo (1979) review IMF, finding it to be a bad fit to the galaxies observed while the Salpeter-like IMF fit well. Contrary to Searle et al. (1973) and Larson & Tinsley (1978), Kennicutt Jr also found that his results suggested there could possibly be variations in the shape of the IMF between galaxy types.

In an important and comprehensive review of studies into the IMF, Scalo (1986) summarised data from the preceding decades to find an IMF with a 'bimodal' shape, by which he meant that it has two peaks - at $0.3M_\odot$ and $1.2M_\odot$. He found the IMF index for high mass stars to be:

$$\Gamma \approx \begin{cases} 1.7 & 2M_\odot \leq m < 10M_\odot \\ 1.3 - 2.4 & m \geq 10M_\odot \end{cases} \tag{1.7}$$

where the shape above $10M_\odot$ is uncertain. Scalo made several observations about the field of research in this review. Firstly, he thought it was unlikely that the relationship between a galaxy's metallicity, element abundances, magnetic field strength, age and other parameters would be constrained either theoretically (given the computational abilities at the time) or observationally. For this knowledge, they would need to wait for the 'distant future'. Secondly, Scalo found that using star counts and the newly developed CCD technology, the very high mass end of the IMF did not appear to vary between several nearby galaxies studied, suggesting a universal IMF at least for high-mass stars. Astronomers were waiting for Space Telescope observations to enable them to compare the high-mass IMF to one found using a count of intermediate-mass stars. Thirdly, studies using integrated light to determine the IMF of galaxies where the individual stars are not resolvable were found to be problematic, but in general agreement with star count studies in finding very little variance in the IMF slope, particularly at high stellar masses. Scalo noted that studies using integrated light depend on far more variables than just the IMF, which adds to the problematic nature of using these techniques to find the IMF. Lastly, Scalo suggested that future studies treat the upper mass limit as another physical parameter since its choice appeared to make an impact on the IMF slope determined. Overall Scalo (1986) found very little evidence for a non-universal IMF shape, and almost no evidence for an IMF that varies radially within galaxies.

A decade later Scalo (1998) revisited this work and came to a different conclusion. Either the uncertainties in determining the IMF slope are so large that it is not possible to know whether a universal IMF exists or not, or there are strong indications of IMF variations. This almost backflip in his conclusion illustrates how far the field had progressed. Advances in instrumentation, with IR cameras and the *Hubble Space Telescope (HST)*, as well as more advanced techniques such as using the spectra of high-mass stars to identify the type and mass of the star, had enabled observational astronomers to apply their research methods in galaxies further away than the Magellanic Clouds. Hunter et al. (1996a,b) utilised the *HST*'s high-resolution photometry to conduct star counts of

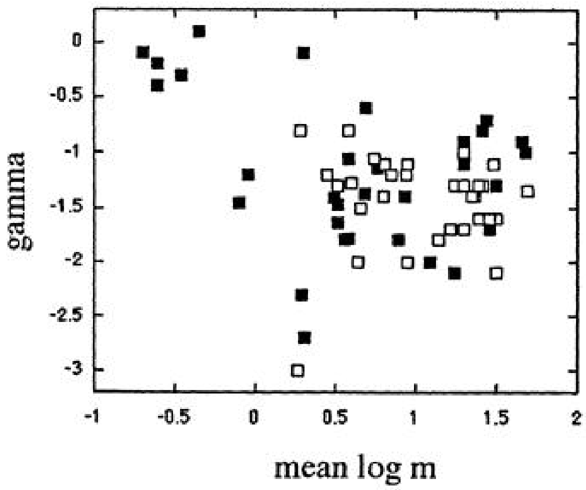

Figure 1.1: The IMF index Γ plotted against the average logarithmic mass for 61 clusters and associations. Filled symbols are objects belonging to the Milky Way, open symbols objects in the LMC. The objects are discussed in Scalo (1998). Error bars are not shown, but range from 0.1 to 0.4 in Γ, with higher error for more massive stars. It can be seen that there is no obvious average IMF for these objects. *Fig. 5 from Scalo (1998)*

intermediate-mass stars in clusters and associations in nearby galaxies. They found an IMF by using a least-squares fit to four mass bins between $6M_\odot$ and $18M_\odot$ for NGC604, a giant HII region in M33 (Hunter et al. 1996a) and NGC206, an OB association in M31 (Hunter et al. 1996b). From these two very different regions, they determine IMFs that within the uncertainties are very similar to each other. However, also using *HST* data, Grillmair et al. (1998) found a range of IMFs for the dwarf spheroidal galaxy Draco which are dependent on the assumed age of the galaxy. This research showed that the constrained IMF depends heavily on the age assumed for a galaxy. The older the assumed age, the steeper the observed IMF. So, if Hunter et al. (1996a,b) assumed incorrect ages for M31 and M33, the derived IMFs may not be quite so similar after all.

As a part of his second review, Scalo (1998) reassessed his Scalo (1986) IMF and concluded that it is only valid in the $1.5M_\odot$ to $15M_\odot$ range, possibly extending to $20M_\odot$, if it is valid at all. Scalo averaged the results from the previous decade of research into a three-segmented power-law form of the IMF:

$$\Gamma = \begin{cases} 0.2 \pm 0.3 & 0.1M_\odot \leq m < 1M_\odot \\ 1.7 \pm 0.5 & 1M_\odot \leq m < 10M_\odot \\ 1.3 \pm 0.5 & 10M_\odot \leq m < 100M_\odot \end{cases} \tag{1.8}$$

with a caveat that he does not think the data can be said to show evidence for an average IMF. This is illustrated in Figure 1.1 (Scalo 1998), where the derived IMF slopes for 61 clusters and associations in the Milky Way and Large Magellanic Cloud (LMC) are plotted. A large spread of values can be seen, and no obvious density of points around an average IMF slope value. Either the uncertainties are so large that the average IMF slope is lost in the noise, or the IMF varies greatly but not systematically. What would cause it to vary? At the time, there was no clear way to break the degeneracy between age, metallicity, star formation history, abundances and IMF slope.

The last contributions of considerable importance in the pre-2010 history of the IMF came from Kroupa (2001) and Chabrier (2003), who revised the IMF by taking unresolved binaries and low mass stars into consideration, respectively. The Kroupa (2001) IMF is in the form of a multi-component power-law, with an IMF index of:

$$\Gamma = \begin{cases} -0.7 \pm 0.7 & 0.01\mathrm{M}_\odot \leq m < 0.08\mathrm{M}_\odot \\ 0.8 \pm 0.5 & 0.08\mathrm{M}_\odot \leq m < 0.5\mathrm{M}_\odot \\ 1.7 \pm 0.3 & 0.50\mathrm{M}_\odot \leq m < 1.00\mathrm{M}_\odot \\ 1.3 \pm 0.7 & m \geq 1.00\mathrm{M}_\odot \end{cases} \tag{1.9}$$

Kroupa expects that any variations in the IMF would rely on the pressure, temperature and metallicity of the original star-forming cloud since these parameters affect the mass of the stars formed. Chabrier (2003) agrees with these possible variation causing parameters, adding that the initial turbulence and density of a gas cloud can affect the low-mass end of the IMF. Unlike Kroupa (2001), who finds no convincing evidence for a variable IMF, Chabrier (2003) finds a weak dependence of the IMF on galaxy environment and cosmic time. As the universe becomes enriched with metals, the temperature of any gas and the way that heat can be transferred also changes, affecting the formation of stars. Baldry & Glazebrook (2003) attempt to break the degeneracy between age and IMF by using a cosmic SFH from high redshift observations which are less sensitive to the slope of the assumed IMF. They assume a universal IMF, and vary the high-mass end to find the best fit, finding a slope that is compatible with the Salpeter IMF (while keeping $\Gamma = 0.5$ for masses between 0.1 and $0.5\mathrm{M}_\odot$). The different parametrisations used can be seen in Figure 1.2.

A summary of the most influential forms of the IMF derived is given graphically in Figure 1.2 (Baldry & Glazebrook 2003), excluding the Chabrier IMF, which can be found in Table 1 of Chabrier (2003). The forms most commonly referenced today are the Salpeter, Kroupa and Chabrier IMFs. For a more detailed overview of the history of the IMF, see Miller & Scalo (1979) or Scalo (1986).

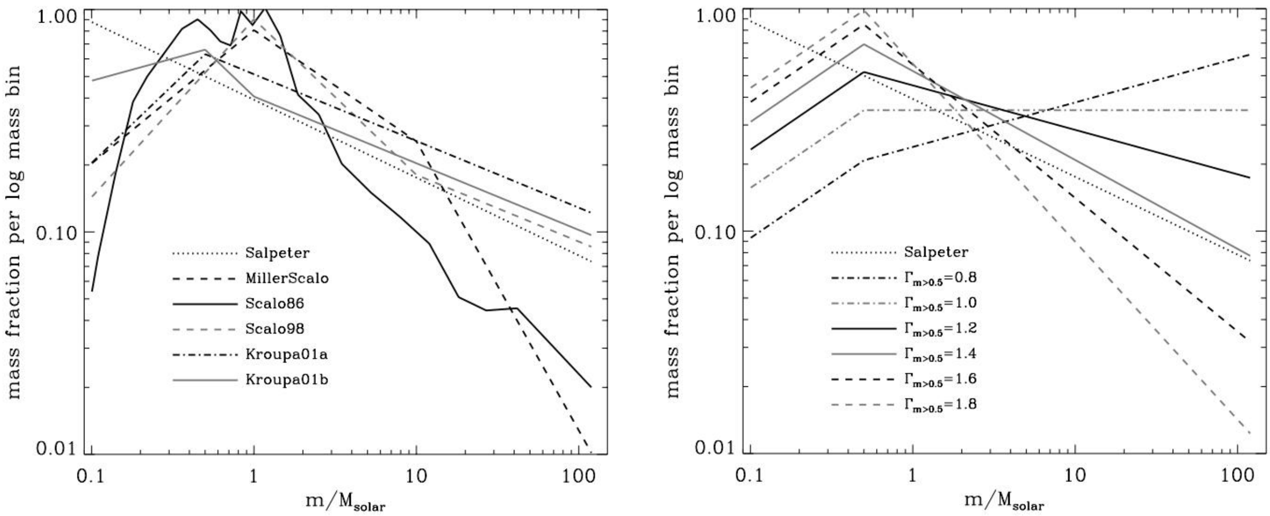

Figure 1.2: Mass fraction per logarithmic mass bin plotted against mass, for masses between 0.1-120 $M_\odot$. *Left hand panel:* compares the Salpeter (1955) (Γ = 1.35), Miller & Scalo (1979) (Γ = 1.5; 2.3), Scalo (1986) (Γ = 2.05; 1.5), Scalo (1998) (Γ = 1.7; 1.3) IMFs and two IMFs from Kroupa (2001) (Γ = 1.3). *Right hand panel:* compares IMF parametrisations using a double power law with Γ from equation 1.3 equal to 0.5 for masses between 0.1 and 0.5, and Γ varying above that. *Fig. 1 from Baldry & Glazebrook (2003)*

1.2 Three Major Techniques

As illustrated in the history of the IMF above, the IMF of the Milky Way had been pretty well constrained by the early 2000s (Kroupa 2001, Chabrier 2003). In more recent years, the focus has turned to other galaxies, where stars cannot be resolved and the IMF is far more difficult to measure. Among the many techniques used to infer the IMF, the principal methods include dynamical modelling, gravitational lensing and stellar population modelling, or a mixture of these.

1.2.1 Dynamical Modelling

The mass-to-light ratio (M/L) is an important parameter of galaxies allowing the calculation of a galaxy's total mass from its luminosity. The M/L ratio is reliant on the IMF to determine the distribution of low-mass, faint stars to high-mass luminous stars to link the luminosity and the mass. Dynamical modelling of a galaxy approaches the problem of galaxy mass from a different angle, using the stellar kinematics to constrain the mass within a particular radius.

Dynamical models are created for a galaxy by fitting for the dark matter halo and the stellar component (dependent on the IMF used) and then comparing to the kinematics to find the most likely combination. A dynamical M/L ratio is calculated using the mass found from these models and the

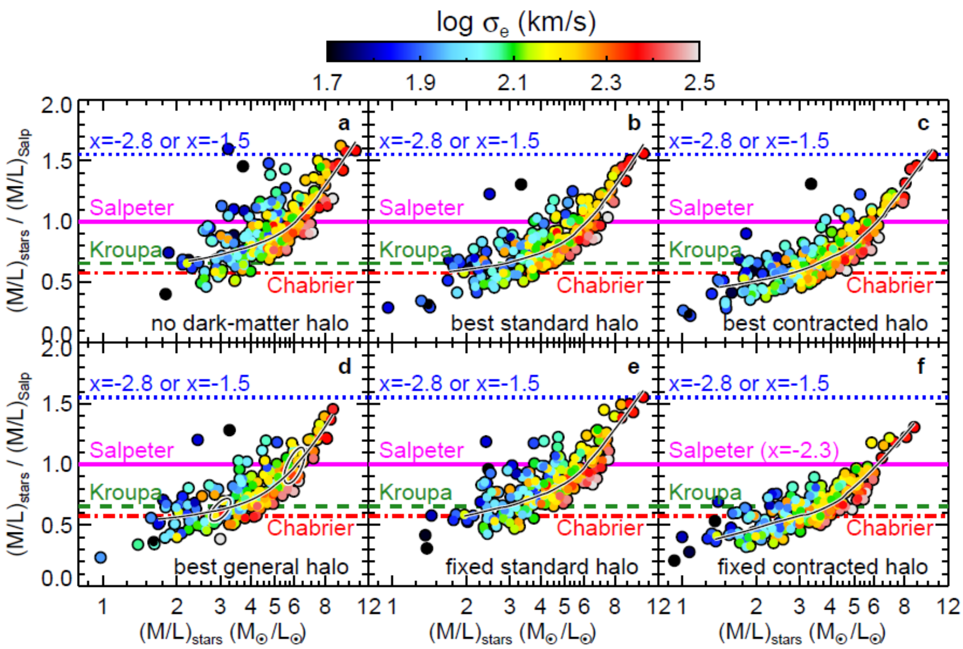

Figure 1.3: The IMF mismatch parameter against the mass-to-light ratio found using dynamical models. Horizontal lines show the expected values for particular IMF values. Each panel assumes a different shape for the dark matter halo. Velocity dispersion is included using a colour scale. There is a strong trend of increasing IMF variations with increasing velocity dispersion which is not dependent on the shape of the dark matter halo. *Fig. 2 from Cappellari et al. (2012)*

total luminosity within the dynamical radius. Using the spectra of the galaxy, a stellar population model with a fixed reference IMF is also fitted optimising age and metallicity for either the full spectrum or particular age, metallicity and abundance sensitive indices. A population or reference M/L ratio is calculated using the luminosity. From both of these models, the IMF mismatch parameter can be calculated:

$$\alpha = \frac{(M/L)_{dyn}}{(M/L)_{pop}} \tag{1.10}$$

where $(M/L)_{dyn}$ is the M/L ratio found from the dynamical model, and $(M/L)_{pop}$ is the M/L ratio found from the stellar population model with a fixed reference IMF. Since both are working with the same luminosity, this mismatch parameter represents the difference in mass calculated from each method. The dynamical M/L ratio should always be greater than the stellar population M/L ratio since the dynamical is affected by the mass of objects not observable in the luminosity (Lyubenova et al. 2016). The IMF mismatch parameter is plotted in Figures 1.3, 1.4 and the right hand panel of 1.6.

The dynamics rely on the total enclosed mass, which includes objects which are not able to be otherwise observed. For example, stellar remnants, low-mass stars, pre-stellar objects and dark matter all contribute greatly to the mass of a galaxy but are not able to be observed in the luminosity. These

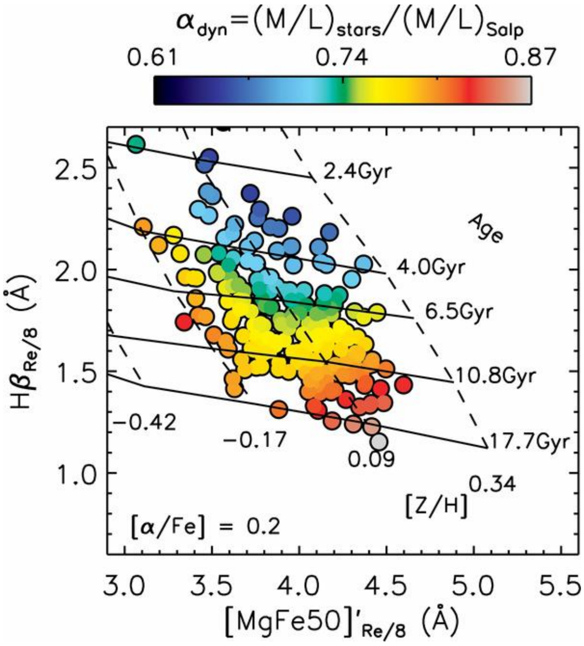

Figure 1.4: Example of a metallicity-age grid made using the Lick index Hβ and combined index [MgFe50]' for a super-solar abundance ratio of [α/Fe] = 0.2. Solid lines indicate constant age, dashed lines indicate constant metallicity. The IMF mismatch parameter α_{dyn}, (the ratio of mass-to-light ratios found using dynamical modelling and stellar population modelling with a fixed IMF) is included using a colour scale. A higher α_{dyn} corresponds to a heavier IMF. *Fig. 1 from McDermid et al. (2014)*

objects can be described by two types of models: dark matter halo shape models; and stellar population models, dependent on the IMF. Although it was unclear even by 2010 whether the IMF was universal (Bastian et al. 2010), the M/L ratio of galaxies was found to vary more than expected. Since the M/L depends so much on both the dark matter and IMF models chosen, this was evidence that either the dark matter fraction changed between galaxies or the IMF was not universal (Treu et al. 2010). Here is another degeneracy, between the universality of either the dark matter fraction or the IMF.

Cappellari et al. (2012) used the dynamical modelling method to find 'unambiguous evidence for a strong systematic variation of the IMF in early-type galaxies (ETGs) as a function of their stellar mass-to-light ratio' for a large sample of galaxies. By keeping the IMF used to fit the stellar population models fixed as a Salpeter IMF and allowing the dark matter halo shape and IMF to be free parameters of the dynamical models, they were able to compare the two using the IMF mismatch parameter, α. When α was plotted against the dynamical M/L ratio, a strong systematic variation of the IMF was shown. The result was not affected by changing the dark matter shape used in the models, breaking this degeneracy, but was related to age and metallicity (see Fig. 1.3).

There was a general consensus by the early 2010s that massive ETGs have different IMFs to MW-like galaxies, and that higher velocity dispersion tends to correlate with a heavier IMF. However, there was little agreement on which parameters were the main driving influences behind IMF variations. The dynamical modelling method has been extended to compare results with absorption line strengths from aperture measurements of multiple galaxies (McDermid et al. 2014) as well as with gas kinematics and stellar populations spatially within galaxies (Davis & McDermid 2016), thereby comparing dynamical results with age, metallicity and abundance ratios for galaxies from the ATLAS^{3D} survey (Cappellari et al. 2011). It was found that on average, older and more alpha-enhanced galaxies had heavier IMFs, but no major correlations between IMF mismatch parameter variations and velocity dispersion, age, metallicity or alpha-enhancement were found either spatially within (Davis & McDermid 2016) or between galaxies (McDermid et al. 2014) (see Fig. 1.4). These results contrast with some results found using stellar population modelling (see Section 1.2.3), for example Martín-Navarro et al. (2015) find a clear relationship correlating metal rich populations with more bottom-heavy IMF slopes. More recently, Oldham et al. (2017) have found that M87 has a stellar M/L ratio that declines as a function of radius. This is most likely consistent with a Salpeter-like IMF at the galaxy centre changing to a Chabrier-like IMF by ~3kpc, agreeing with results for M87 from Oldham & Auger (2017), as well as those from Sarzi et al. (2018a) using stellar population methods. More generally, this picture of bottom-heavy galaxy centres also agrees with results from stellar population methods for other ETGs (e.g. Martín-Navarro et al. 2014, La Barbera et al. 2016a,b)

One issue with finding the IMF using the dynamical mass is that it is impossible to tell if it is bottom- or top-heavy. Bottom-heavy IMFs are dominated by dwarf stars, top-heavy IMFs by stellar remnants (black holes, neutron stars and white dwarfs), and both could produce the same dynamical M/L ratio (Cappellari et al. 2012). This is why in Figure 1.3, the IMF slopes -2.8 (bottom-heavy) and -1.5 (top-heavy) are indistinguishable. The only way to distinguish the two cases is by using the stellar spectra.

1.2.2 Gravitational Lensing

Gravitational lensing is an alternative method used to find the mass of a galaxy within a specific radius. The mass of a foreground lensing galaxy within the Einstein radius is found using the geometry of the gravitational lens. This is then used to find a M/L ratio and applied similarly to the method used for dynamical models above. Gravitational lensing has similar drawbacks to the dynamical models. The dark matter halo mass fraction must be separated from the stellar mass component, and the difference between mass from a dwarf star dominated population (bottom-heavy IMF) and a stellar remnant dominated population (top-heavy IMF) cannot be distinguished. Gravitational lensing has the added difficulty of relying on the full integrated mass along a sight line. This means that the assumed shape for the galaxy dark matter halo plays a much larger role than in dynamical modelling. However, the estimations for total mass within a galaxy that gravitational lensing provides are very precise and can be applied to non-local galaxies, improving our understanding of the IMF at higher redshifts. Examples using gravitational lensing are Treu et al. (2010), Spiniello et al. (2012), Posacki et al. (2014), Spiniello et al. (2015b) and Leier et al. (2016).

1.2.3 Stellar Population Modelling

The mass of a star determines its evolutionary track and the elements that it produces in its lifetime, producing characteristic mass-dependent spectral features. The integrated spectra of a galaxy population can, therefore, be used to find a ratio between low- and high-mass stars. For example, the Na I doublet (Faber & French 1980) and the Wing-Ford molecular FeH band (Wing & Ford Jr 1969) both appear strongly in the spectra of stars with masses less than $0.3M_{\odot}$, but are weak or absent in stars with greater masses; whereas the Ca triplet lines (hereafter CaT, Cenarro et al. 2003) are strong in giants and extremely weak in dwarf stars (van Dokkum & Conroy 2012). Using gravity sensitive absorption lines in this way was first proposed by Spinrad (1962). Early work in this area was beset by problems including low S/N and low resolution data as well as small sample sizes and uncertain stellar models. Two main camps developed - those attributing changing feature strength to dwarf-enrichment (eg. Spinrad & Taylor 1971, Faber & French 1980, Carter et al. 1986, Cenarro et al. 2003) and those concluding it was a metallicity-caused effect (eg. Cohen 1978, Hardy & Couture 1988, Delisle & Hardy 1992). It is only in the past decade that the quality of data has improved enough that the strength of particular absorption features can be measured accurately.

More recently, the NaI line and Wing-Ford band were detected by van Dokkum & Conroy (2010) in all eight of their sample of massive, luminous ETGs, suggesting a large population of low mass stars and a bottom-heavy IMF (more low mass stars than expected). This is an important result, which shows that massive elliptical galaxies don't necessarily have the same IMF as our Milky Way. Van Dokkum & Conroy (2010) conclude that the IMF is not universal and that it depends on the conditions at the time of star formation, with quiet star-forming disks producing a Kroupa-like (Milky Way-like) IMF, and the progenitors of massive ellipticals producing dwarf-rich IMFs. The idea that elliptical galaxies have very different IMFs to present-day star-forming spiral galaxies is supported by a follow-up paper studying a much larger sample of galaxies, where they find that bottom-heavy IMFs fit their galaxies well (van Dokkum & Conroy 2012). Adding the Ca II triplet (Cenarro et al.

2003), which is strong in giant stars but weak in dwarfs, they find a possible correlation between increasing velocity dispersion and increasing dwarf population. Spiniello et al. (2012) also report a steepening of the low-mass IMF with increasing velocity dispersion in ETGs, and likewise propose that the IMF steepens between Spirals and ETGs. More recent research focusing on M87 suggests that the different IMF in ETGs is confined to the galaxy centre, where it tends to be bottom-heavy, with a more Milky-Way like IMF at greater radii (Sarzi et al. 2018a).

The correlation between IMF and velocity dispersion is also dependent on metallicity, abundance variations and age. To break this degeneracy, Spiniello et al. (2014) suggest a group of new indices based on TiO and CaH molecular lines which have the advantage of avoiding sky lines and tellurics. One of these, CaH1 (6380Å), is apparent in cool dwarves, not dependent on age and is anti-correlated with [α/Fe]. Using this line in combination with others more dependent on age, metallicity and alpha abundances, the degeneracies between these parameters and the IMF can be broken (Spiniello et al. 2014, Spiniello 2016). Similarly applying combinations of indices to break the degeneracies, La Barbera et al. (2013) also find a trend between the IMF and central velocity dispersion.

There are two main ways to use the stellar population modelling method: by measuring the line strengths of particular indices sensitive to particular galaxy parameters as just described (van Dokkum & Conroy 2010, 2012, Spiniello et al. 2014, Lyubenova et al. 2016, Spiniello 2016, La Barbera et al. 2016b, Rosani et al. 2018, Parikh et al. 2018) or by fitting a model to the entire galaxy spectrum (Conroy & van Dokkum 2012a,b, Conroy et al. 2017, Vaughan et al. 2018). Two main sets of simple stellar population (SSP) models have been developed to model ETGs - the Conroy & van Dokkum (2012a) models, recently updated (Conroy et al. 2018); and the MILES (Vazdekis et al. 2010, 2015), and their extended versions MIUSCAT (Vazdekis et al. 2012) and E-MILES (Vazdekis et al. 2016). Comparing these two regimes, Spiniello et al. (2015a) found that although the quantitative results did not agree, qualitatively both SSP models produce results requiring a non-universal IMF.

Fitting the entire spectrum of a galaxy while leaving age, metallicity, alpha abundances and the IMF slope as free variables is heavy on computational power and time, so using line strengths is most common. From both methods, however, the degeneracy between age, metallicity, abundance variations and variations in the IMF, all of which have similar effects on spectral features, still needs to be dealt with.

1.2.4 Comparing Dynamical and Stellar Population Modelling

Dynamical and stellar population modelling methods produce similar results, showing that massive ETGs typically have more bottom-heavy IMFs than the MW, becoming more bottom-heavy with greater galaxy mass. However, some discrepancies between the two methods were pointed out by Smith (2014), who compared work using spectroscopic stellar population modelling by Conroy & van Dokkum (2012b) and dynamical models by ATLAS3D (Cappellari et al. 2013). These two papers have 34 galaxies in common so their results can be compared on a galaxy-by-galaxy basis. Smith (2014) finds that there is no correlation on a galaxy-by-galaxy basis between the two methods. He suggests that abundance patterns or dark matter contributions may not have been properly accounted for when finding the IMF. However, this conclusion depends on the comparison of two papers using very different data sets, covering different areas of the galaxies.

Lyubenova et al. (2016) counter by comparing dynamical and stellar population modelling using the same data set, and by enforcing the rule that the stellar M/L ratio must always be smaller than or equal to the dynamical M/L ratio, otherwise the IMF used is unphysical. The differences between the two methods can be used to constrain the IMF and will be particularly useful for studying the radial IMF and not just the integrated light over an area (Lyubenova et al. 2016). Using the two methods together may help break or circumnavigate some of the degeneracies which plague both dynamical and stellar population modelling. For example, Treu et al. (2010) used a combination of gravitational lensing, dynamical and population modelling to disentangle the contributions of dark and stellar mass to the total galaxy mass.

1.3 Variables affecting the IMF

There is a growing consensus that the IMF is not universal between galaxies, but becomes more bottom-heavy in more massive galaxies, which have a higher velocity dispersion (Treu et al. 2010, Cappellari et al. 2012, van Dokkum & Conroy 2012, Conroy & van Dokkum 2012b, Ferreras et al. 2012, Spiniello et al. 2015a, La Barbera et al. 2015, Davis & McDermid 2016, Rosani et al. 2018). However, Smith (2014) finds in his comparison of stellar population and dynamical methods that a correlation between varying IMF and velocity dispersion is only found using the dynamical modelling method. Similarly, he finds a correlation between alpha-element abundances and varying IMF only when using the stellar population modelling method.

Other possible contributing parameters are the metallicity (Martín-Navarro et al. 2014), although

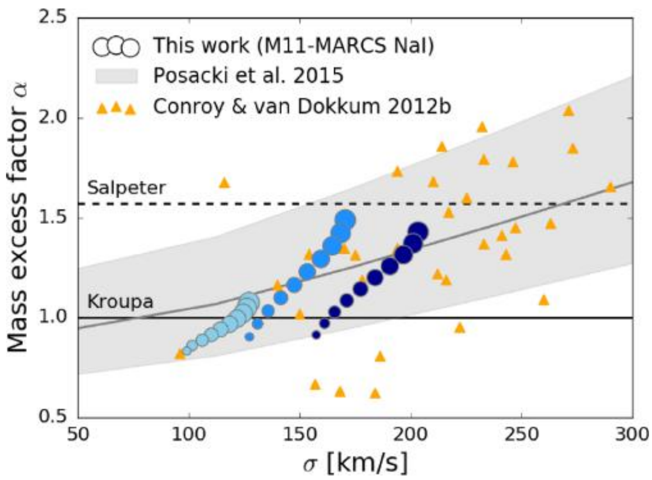

Figure 1.5: The mass excess factor, or IMF mismatch parameter α calculated with an assumed Kroupa IMF plotted against velocity dispersion. Light, mid and dark blue circles represent the mass bins $logM/M_{\odot}$ = 9.9-10.2; 10.2-10.5; and 10.5-10.8 respectively. Decreasing circle size represents increasing galaxy radius (distance from galaxy centre). This shows increasing bottom-heaviness with increasing velocity dispersion and mass, and decreasing distance from the galaxy centre. Comparison papers are Conroy & van Dokkum (2012b), Posacki et al. (2014). *Fig. 16 from Parikh et al. (2018)*

it has been found that this cannot be the only cause of variation (Villaume et al. 2017b); the alpha-element abundances (Conroy & van Dokkum 2012b, McDermid et al. 2014); the age (McDermid et al. 2014); or the total dynamic mass density (Spiniello et al. 2015b). However, most of these parameters have generally only been found to have very weak correlations with variation in IMF. In a study considering age, metallicity, alpha element abundances and velocity dispersion, Rosani et al. (2018) find that any variation in IMF for early type galaxies is not dependent on their environment or their hierarchy in relation to the galaxies around them.

1.4 Spatial variation of the IMF within galaxies

Whether the IMF is universal or varies between galaxies has been a controversial topic in the literature for decades. With the advent of technology that allows us to resolve sections of galaxies has arisen the question of whether the IMF also varies radially within galaxies. The majority of the literature focuses on ETGs when considering this question, due to higher homogeneity in their stellar populations. It should be noted that this very reason for using ETGs also prevents useful investigation into the high-mass end of the IMF, since these stars have already disappeared from the population. In order to study the high-mass end of the IMF, it is necessary to look at star forming galaxies. Although we have not been able to detect these IMF variations within the Milky Way (Scalo 1986, Kroupa 2001, Bastian et al. 2010), perhaps this is because we cannot see the whole picture.

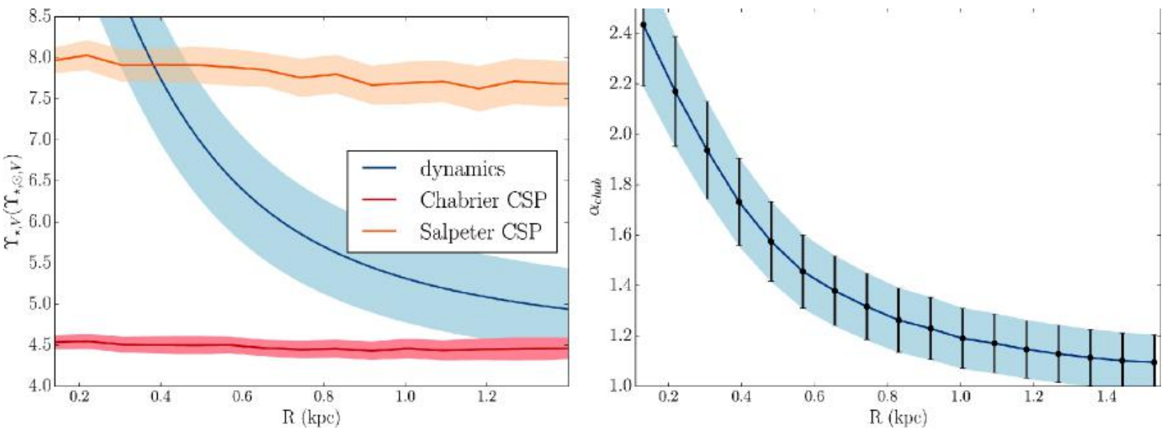

Figure 1.6: *Left:* The mass-to-light ratio derived for a fixed Chabrier and Salpeter IMF, compared to the dynamically derived mass-to-light ratio. This shows that fixed IMFs cannot explain the gradient, suggesting a radially varying IMF. *Right:* The IMF mismatch parameter, α, with an assumed fixed Chabrier IMF (see Eq. 1.10) plotted against radius. A fixed IMF does not match the gradients seen here, suggesting an IMF varying from bottom-heavy at the centre to MW-like. *Fig. 4 from Oldham & Auger (2017)*

The development of high-resolution spectrographs such as MUSE (Bacon et al. 2010) has allowed more spatially resolved studies within galaxies. For example Sarzi et al. (2018a) and Oldham & Auger (2017) using stellar population and dynamical modelling respectively both find that there is an IMF gradient in M87. Using high-resolution spectroscopy from MUSE, they were able to identify a bottom-heavy IMF at the galactic centre, transitioning to a Milky-Way-like IMF by $0.4R_e$. This gradient can be seen in Figure 1.6. The galaxy property which best traced this change was metallicity, while local velocity dispersion surprisingly appeared to play less of a role (Sarzi et al. 2018a). In another recent study, Parikh et al. (2018) have extensively researched the spatially resolved variations of the IMF within galaxies, finding that the radial gradient of the IMF becomes more apparent in higher mass galaxies. Velocity dispersion and local metallicity appear to be the main contributing factors from their study (see Fig. 1.5). Contrarily, La Barbera et al. (2016b) found that [Na/Fe] element abundances are coupled to the radial IMF slope, with a change in IMF strongly affecting the Na line strengths.

The current stage of technology and research in the field of extra-galactic IMF studies produces a few key questions. How can we relate the internal, spatial variations of the IMF with any trends observed between galaxies? Do these trends hold for galaxy types other than ETGs, or how else do they fit in? Which parameters are most likely to be driving IMF variations both spatially within and more globally comparing galaxies? More resolved studies of the IMF and other galaxy parameters need to be done using contrasting but comparable techniques. Using multiple methods enables the separation of effects and biases proceeding from each method. With these accounted for, it will be possible to constrain potential spatial variations of the IMF within galaxies. These variations can then be compared to variations in environmental features such as velocity dispersion, metallicity and element abundances, enabling our understanding of which parameters are most involved in causing variations of the IMF.

1.5 This Thesis

The data used for this project has been provided by the Fornax3D (F3D) project (Sarzi et al. 2018b). One of the aims of F3D is to provide spatially resolved studies of the stellar populations of ETGs in order to constrain variations in their stellar IMF. F3D used the Multi-Unit Spectroscopic Explorer (MUSE, see Bacon et al. 2010) on ESO's Very Large Telescope (VLT) to observe ETGs in the Fornax cluster. MUSE is an integral-field spectrograph with 24 Integral Field Unit modules producing high signal-to-noise data in both the spectral and spatial directions. With a wavelength range of 480-930nm, MUSE covers a 1 arcminute squared FOV with 0.2 arcsecond per pixel sampling. Such high quality data provides the spatial resolution to map in great detail changes in the spatial structure of stellar population properties in galaxies. MUSE also provides the spectral resolution to more accurately trace changes in abundances, metallicity, age and most importantly, the IMF. This enables the creation of complete spatial maps of stellar population properties in high resolution.

Utilising this high-resolution spatial spectral data, this thesis aims to measure spatial variations in the IMF. Following Vaughan et al. (2018), a new full-spectral fitting routine known as PyStaff is tested. This method enables changes in multiple parameters including the IMF to contribute across the entire spectrum. Comparisons are made to a new method being developed by Martín-Navarro et al. (by private communication) combining spectral fitting and index approaches into a 'selective spectral fitting' method.

Chapter 2 outlines in more detail the data used within this project, methods used in the reduction process and complications within the data highlighted by the reduction. Chapter 3 investigates PyStaff as a method for fitting for the IMF and compares it to the method in development by Martín-Navarro et al.

'The time has come,' the Walrus said,

'To talk of many things:

Of shoes and ships - and sealing wax -

Of cabbages and kings'

Lewis Carroll, Through the Looking-Glass

2

The Data

2.1 Observations and Data Reduction

2.1.1 Fornax3D

The survey completed by F3D included the central regions of spiral galaxies and the central regions and stellar halos of ETGs with a total B-band magnitude less than $m_B = 15mag$ falling within the virial radius of the Fornax cluster ($R_{vir} \approx 0.7Mpc$ or about 2 degrees) (Sarzi et al. 2018b). The number of pointings taken for each galaxy depended on the diameter of the galaxy. While both the central regions and galaxy outskirts of smaller ETGs could be covered by one pointing, some of the larger ETGs required several overlapping pointings. These overlapping pointings were then combined into a single datacube through the MUSE data reduction pipeline. An example of the overlapping pointings is given in Figure 2.1. The placement of the pointings for the remainder of the galaxies can be found in the Appendix.

The MUSE data reduction pipeline provided by ESO includes bias subtraction, flat fielding, wavelength calibration, illumination correction, correction for variation of spectral resolution across

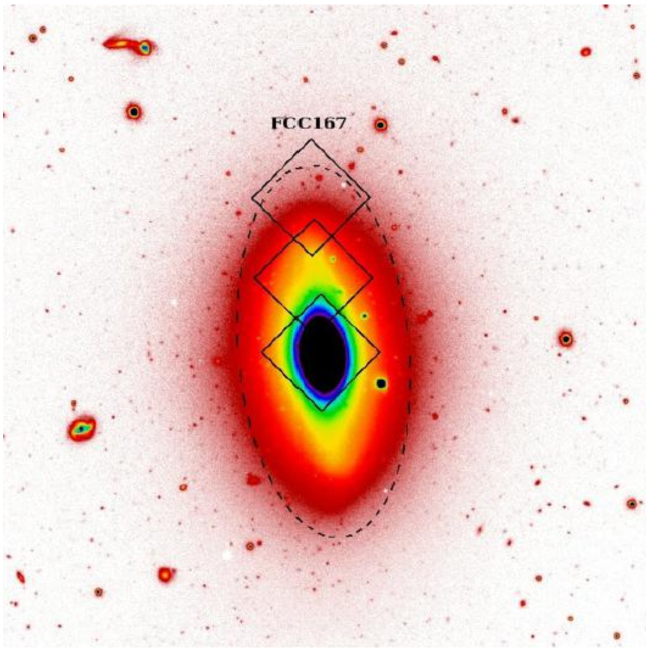

Figure 2.1: An example of multiple pointings across a galaxy, here FCC167. These are then combined into a single datacube.

the FOV and sky subtraction. The F3D team used pipeline version 2.2 (Weilbacher et al. 2012, 2016) within the EsoReflex environment (Freudling et al. 2013) (hereafter 'F3D reduction pipeline') to reduce the data that was then used in this project (Sarzi et al. 2018b). The pipeline first works on the data from individual CCDs in order to make data coming from each separate IFU comparable and then combines these into an exposure. Multiple exposures are optionally combined to create the final cube (MUSE Pipeline Team 2017).

2.1.2 Galaxy Sample for this thesis

The F3D Survey took data for 33 galaxies within the Fornax cluster, 17 of which were made available as fully reduced cubes at the time of writing. These galaxies are detailed in Table 2.1, and are the galaxies on which the initial results pipeline written for this thesis (described in Section 2.2) has been implemented. Observations were made using MUSE's wide field mode configuration, covering the wavelength range 4650-9300Å with 1.25Å pixel^{-1} spectral sampling and a spectral resolution of 2.5Å (FWHM) at 7000Å. The 1 x 1 arcmin^2 field of view was spatially sampled at 0.2 x 0.2 arcsec^2 (Sarzi et al. 2018b).

Chapter 3 focuses on two techniques to investigate the IMF in FCC 167 (NGC 1380), a well resolved and high surface brightness S0/a galaxy with a mosaic of three pointings. This galaxy was chosen because of its high signal-to-noise, which is needed to characterise the slight changes in the

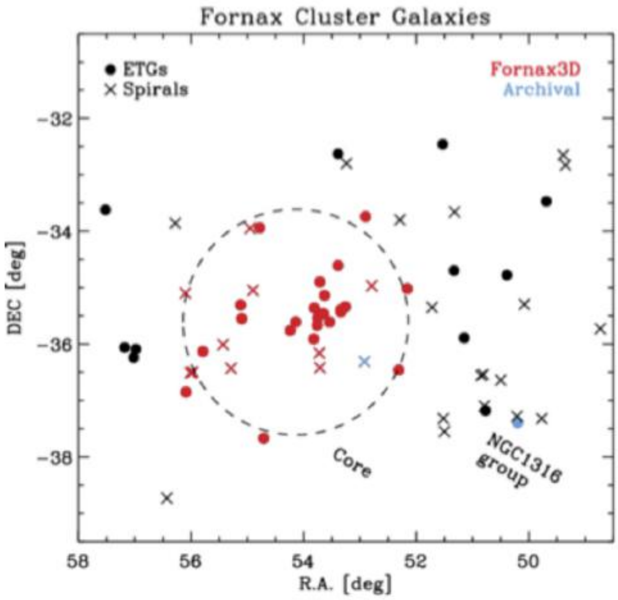

Figure 2.2: The sample of galaxies included in the F3D survey. Circles correspond to ETGs, crosses to LTGs, red symbols to galaxies included in F3D, blue symbols to galaxies with archival MUSE data. The dashed circle shows the Fornax cluster's virial radius (≈ 0.7 Mpc). (Sarzi et al. 2018b, Fig. 1)

spectra caused by variations in the IMF. FCC167 was observed with exposure times of 5 x 720s, 6 x 600s and 9 x 600s for the central, middle and halo pointings respectively (Sarzi et al. 2018b).

2.2 Initial Data Analysis

2.2.1 Voronoi Binning

To reach a target signal-to-noise ratio (S/N) for each galaxy (see Table 2.1) the data was spatially binned. Voronoi binning (Cappellari & Copin 2003, Cappellari 2009) is adaptive, allowing single spaxels (spatial pixels) in the centre of bright galaxies to remain single, while spaxels towards the edge of a galaxy with a lower signal will be combined with nearby spaxels into a bin until the bin reaches the required S/N. The Voronoi Binning method was developed with the requirements that bins are to tessellate with no gaps, be as round as possible to retain spatial resolution, and have as small a scatter around the target S/N as possible (Cappellari & Copin 2003). This results in a pattern of irregularly shaped roundish polygonal bins, generally increasing in size away from the brighter regions of a galaxy.

A S/N of $10Å^{-1}$ is sufficient for mapping the age and metallicity of the galaxies when using full-spectrum fitting (Choi et al. 2014). However, a target S/N of at least $30Å^{-1}$ is needed to reliabley recover chemical abundances (Choi et al. 2014). The S/N of each single spaxel in the F3D data was

Object	Type	Redshift (z)	m_B (mag)	S/N target (Å^{-1})	Bins	Comments
FCC090	E4 pec	0.006261	15.0	50	454	
FCC113	ScdIII pec	0.004625	15.2	50	54	
FCC119	S0 pec	0.005030	15.0	50	207	
FCC143	E3	0.004573	14.3	100	293	
FCC153	S0	0.005480	13.0	200	253	2 combined
FCC167 centre	S0/a	0.006160	...	300	310	
FCC167 middle	S0/a	0.006160	...	300	87	
FCC167 halo	S0/a	0.006160	...	300	4	
FCC167 combined	S0/a	0.006160	11.3	100 / 300	3516 / 363	3 combined
FCC170	S0	0.005917	13.0	100	1462	2 combined
FCC176	SBa	0.004747	13.7	100	154	
FCC177	S0	0.005240	13.2	100	953	2 combined
FCC182	SB0 pec	0.005951	14.9	100	75	
FCC249	E0	0.005551	13.6	100	642	
FCC255	S0	0.004306	13.7	100	327	
FCC263	SBcdIII	0.005856	14.6	100	223	
FCC277	E5	0.005817	13.8	100	407	
FCC285	SdIII	0.002979	14.2	25	62	very low signal
FCC301	E4	0.003386	14.2	100	290	
FCC306	SBmIII	0.004084	15.6	40	80	

Table 2.1: Summary of galaxies included in this project. *Object:* the galaxy's name; *Type:* morphological type (Sarzi et al. 2018b, Ferguson 1989); *Redshift:* information from SIMBAD Astronomical Database; u_B*:* total *B*-band magnitude (Sarzi et al. 2018b); *S/N target:* the target for the Voronoi binning (FCC167 used S/N=100Å^{-1} for the initial pipeline and S/N=300Å^{-1} for IMF full-spectrum fitting); *Bins:* the final number of Voronoi bins; *Comments:* Any comments on the galaxy. Combined indicates more than one pointing combined into the cube.

estimated to be the ratio of the median spectral flux and the square-root of the median variance as provided by the reduction pipeline. Galaxies were binned to a target S/N given for each galaxy in Table 2.1, all exceeding S/N $\approx$ 30Å^{-1} apart from FCC285, a small faint irregular galaxy. Brighter galaxies were binned such that the number of bins created did not become computationally heavy. FCC167 has been binned to two targets, one (S/N = 100Å^{-1}) for comparison with the remainder of the galaxies in the initial pipeline; the second (S/N = 300Å^{-1}) for comparison with other studies measuring the IMF (e.g. Vaughan et al. 2018). The high surface brightness of FCC167 allows this heavy binning with minimal loss in spatial resolution. A threshold S/N of 3Å^{-1} was applied to the unbinned cubes to avoid including spectra dominated by sky background in the outer regions of the galaxies.

2.2.2 PPXF

The Penalised PiXel Fitting (pPXF) full spectrum fitting routine developed by Cappellari & Emsellem (2004) and recently updated (Cappellari 2017) has been used to fit kinematic information to each binned spectrum. Stellar templates from the MILES library (Vazdekis et al. 2010) were used with Padova+00 isochrones (Girardi et al. 2000), an assumed unimodal IMF with a logarithmic slope of 1.3 (standard Salpeter (1955)), a range of ages from 0.063 to 15.85 Gyr, metallicities [M/H] from -1.71 to 0.22, and base (Milky Way-like) solar scaled alpha element abundance [α/Fe]. With gas emission

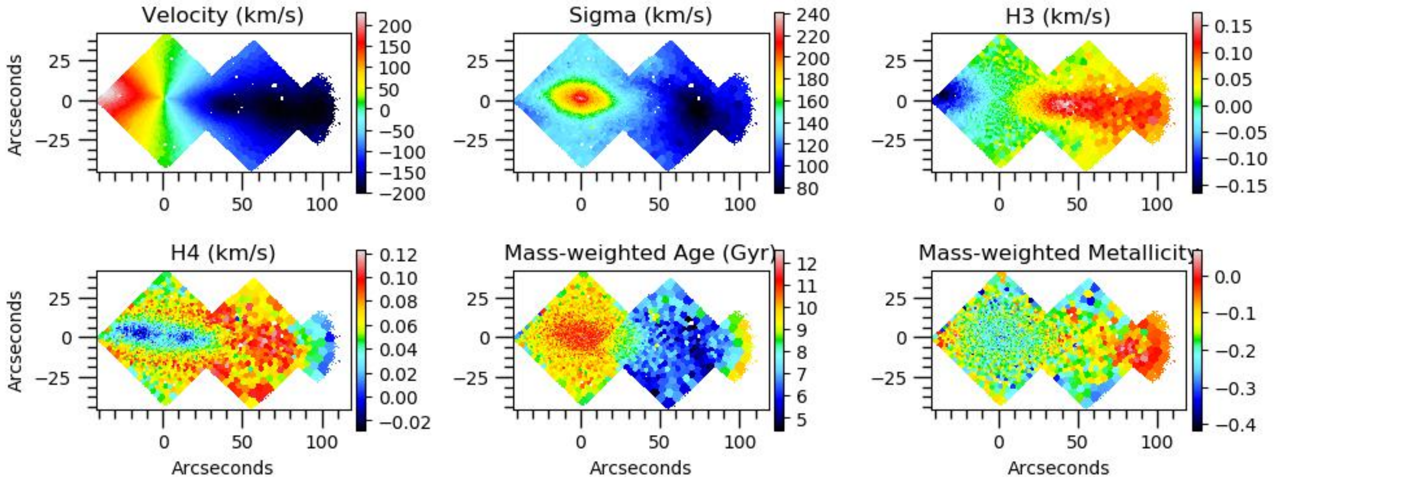

Figure 2.3: The stellar velocity, velocity dispersion (sigma), 3rd and 4th kinematic moments (h3 and h4) as well as the mass-weighted age and metallicity from pPXF for the galaxy FCC167, binned to a target S/N of 100Å^{-1}.

lines masked using the keyword 'goodpixels', pPXF was used to derive the parameterised line-of-sight velocity distribution in terms of the mean velocity (v), velocity dispersion (σ), and higher-order moments h_3 and h_4 (van der Marel et al. 1993, Gerhard 1993). The non-regularised template weights for the combination of fitted models were then used to find the mass-weighted age and metallicity.

Figure 2.3 shows an example of the results from pPXF found for the galaxy FCC167, Voronoi Binned to a target S/N of 100Å^{-1}. From the kinematics, it is apparent that FCC167 is a regularly rotating galaxy, with a significant disk-like structure dominating the outer portion of the MUSE data. The high sigma values in the centre of the galaxy are the signature of the bulge. Using a similar method, Sarzi et al. (2018b) find two disc components - a thin, dynamically cold disc within a thick, dynamically warm disc with weaker rotation. These components can be detected in the h_3 and h_4 maps (Fig. 2.3). Although the mass-weighted age map reveals a mismatch between the pointings (further discussed below), we can still gather that the bulge is older than the rest of the galaxy. Interestingly, FCC167 shows only a very weak radial gradient in the mass-weighted metallicity map. This is quite unlike FCC153, FCC170 and FCC177 (similar galaxies in our sample) where the disk and bulge are clearly younger and more metal rich than the rest of the galaxy (see Appendix Figures 8, 10 and 14). The pPXF results for a selection of the remainder of the galaxies in Table 2.1 can be found in the Appendix. Due to space restrictions, not all galaxies could be included, however the maps are available upon request.

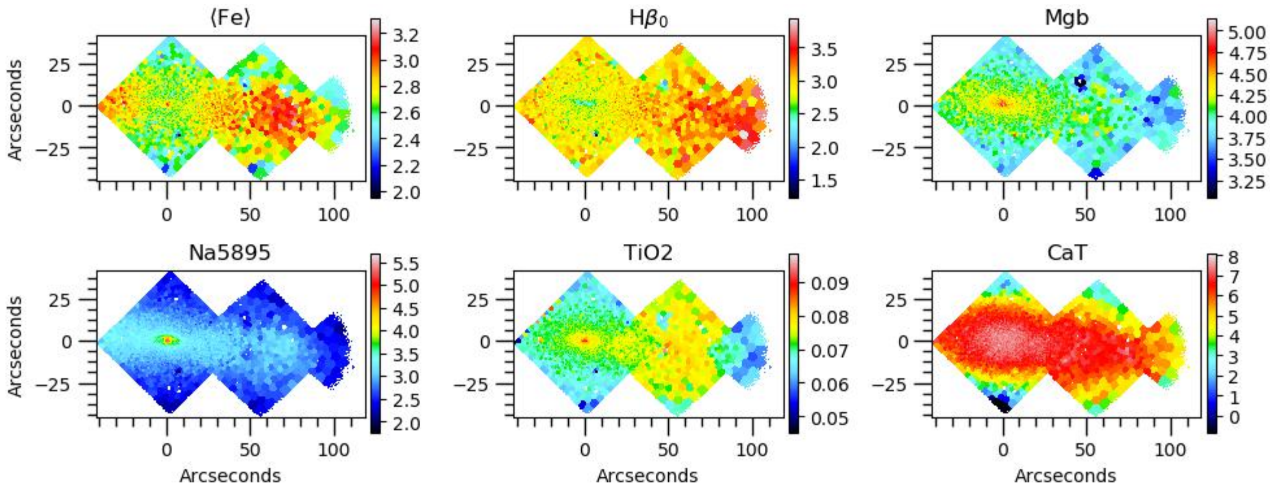

Figure 2.4: Maps of ⟨Fe⟩ *(top left)*, Hβ_0 *(top middle)*, Mgb *(top right)*, NaD [5895] *(bottom left)*, TiO2 *(bottom middle)*, and CaT *(bottom right)* for the galaxy FCC167, binned to a target S/N of 100Å^{-1}.

2.2.3 Line-Strength Indices

To obtain a robust empirical view of the stellar population properties of the galaxy sample, the strength of various absorption features in the spectra is measured using the classic approach of line strength indices (e.g. Worthey et al. 1994). The measured indices are defined in Table 2.2, including indices for NaI (La Barbera et al. 2013, 2016b) and the calcium II triplet (Cenarro et al. 2001). Maps of key indices for FCC167 are presented in Figure 2.4, and for a selection of other galaxies maps are given in the Appendix. These include the composite indices ⟨Fe⟩ (Trager et al. 2000)[1] and CaT (Cenarro et al. 2001)[2].

A full analysis of the line strengths would involve comparing the measured indices to stellar population models, whereas the focus of this thesis is on spectral fitting. However, the measured indices show general agreement with the mass-weighted pPXF age and metallicity maps. Hβ_0 becomes weaker towards the centre, indicating similarly to the mass-weighted age map an older central bulge (though note that Balmer emission affects the most central Hbeta index measurements, so these must be treated with caution). The ⟨Fe⟩ index broadly agrees with the mass-weighted metallicity map, in that the bulge appears slightly metal poor compared to the disk. <Fe> (and other metal indices) does, however, show a strong central peak near the galaxy nucleus that is not apparent in the pPXF results.

Na5895 traces the Na abundance and is useful as a comparison to the NaI line, which, once Na abundance is accounted for, allows us to trace the IMF (La Barbera et al. 2016b). The Na abundance shown in the Na5895 map traces the disc structure in FCC167, with a sharp peak in strength in the

[1] $\langle \mathrm{Fe} \rangle = \frac{1}{2}(\mathrm{Fe5270} + \mathrm{Fe5335})$

[2] $\mathrm{CaT} = \mathrm{Ca1} + \mathrm{Ca2} + \mathrm{Ca3}$

Index	Blue Continuum (Å)	Central Feature (Å)	Red Continuum (Å)	Reference
Fe4668	4611.500-4630.250	4634.000-4720.250	4742.750-4756.500	Lick
Hbeta	4827.875-4847.875	4847.875-4876.625	4876.625-4891.625	Lick
Hbetao	4821.175-4838.404	4839.275-4877.097	4897.445-4915.845	Lick
Hbetap	4815.000-4845.000	4851.320-4871.320	4880.000-4930.000	Gonzalez (p116)
Fe4930	4894.500-4907.000	4903.000-4945.500	4943.750-4954.500	Gonzalez (p34)
OIII1	4885.000-4935.000	4948.920-4978.920	5030.000-5070.000	Gonzalez (p116)
OIII2	4885.000-4935.000	4996.850-5016.850	5030.000-5070.000	Gonzalez (p116)
Fe5015	4946.500-4977.750	4977.750-5054.000	5054.000-5065.250	Lick
Mg1	4895.125-4957.625	5069.125-5134.125	5301.125-5366.125	Lick
Mg2	4895.125-4957.625	5154.125-5196.625	5301.125-5366.125	Lick
Mgb	5142.625-5161.375	5160.125-5192.625	5191.375-5206.375	Lick
Fe5270	5233.150-5248.150	5245.650-5285.650	5285.650-5318.150	Lick
Fe5335	5304.625-5315.875	5312.125-5352.125	5353.375-5363.375	Lick
Fe5406	5376.250-5387.500	5387.500-5415.000	5415.000-5425.000	Lick
Fe5709	5672.875-5696.625	5696.625-5720.375	5722.875-5736.625	Lick
Fe5782	5765.375-5775.375	5776.625-5796.625	5797.875-5811.625	Lick
Na5895	5860.625-5875.625	5876.875-5909.375	5922.125-5948.125	Lick
TiO1	5816.625-5849.125	5936.625-5994.125	6038.625-6103.625	Lick
TiO2	6066.625-6141.625	6189.625-6272.125	6372.625-6415.125	Lick
NaI	8143.000-8153.000	8180.000-8200.000	8233.000-8244.000	La+13, La+16
Ca1	8474.000-8484.000	8484.000-8513.000	8563.000-8577.000	C+01, La+13
Ca2	8474.000-8484.000	8522.000-8562.000	8563.000-8577.000	C+01, La+13
Ca3	8619.000-8642.000	8642.000-8682.000	8700.000-8725.000	C+01, La+13

Table 2.2: Definitions for the indices measured, wavelengths in the air system. Lick indices from Trager et al. (1998), Gonzalez (1993) from his PhD, La+13 from La Barbera et al. (2013), La+16 from La Barbera et al. (2016b) and C+01 from Cenarro et al. (2001).

central bulge. TiO2 and the CaT indices are gravity-sensitive, TiO2 appearing in dwarf stars and giant stars but absent in main-sequence stars (Spiniello et al. 2014), and CaT appearing only in giant stars. They can therefore also be used to trace changes in the IMF (e.g. La Barbera et al. 2016a, Cenarro et al. 2003), particularly in ETGs, where the old stellar population probes the dwarf and main-sequence range of the IMF. In Figure 2.4 the sharp peak in the TiO2 map and the gradual decrease in CaT strength radially outwards suggests a bottom-heavy IMF at the very centre of the galaxy, flattening with increasing radius. However, full consideration of the age, metallicity and abundance properties must be made before this conclusion from the indices can be confirmed. This analysis is deferred to future work.

2.3 Data Reduction Refinements

A clear mismatch between pointings in the mass-weighted age map (Fig. 2.3) as well as the TiO2 (Fig. 2.4) and other index maps motivated a closer investigation into possible differences introduced before the pointings were combined into a single cube. The main differences were found to be caused by sky subtraction and telluric correction issues, as explained further below.

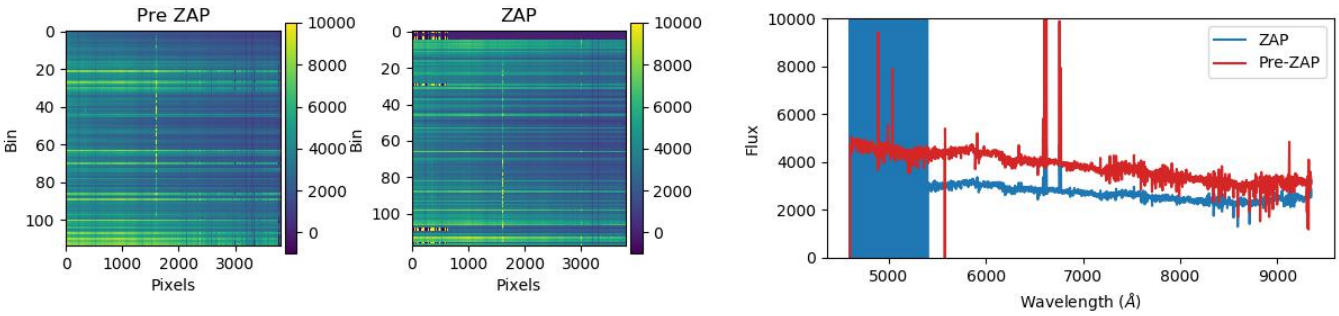

Figure 2.5: A comparison of data from FCC090 before and after being ZAPped. The first two panels show an overview of FCC090 binned to a S/N target of 100Å^{-1} for the data before being ZAPped (*left*) and after being ZAPped (*middle*). The colour scale shows flux intensity. *Right:* Comparing the spectral bin from each data set which was found to have the highest standard deviation, disregarding spatial position. The blue block of colour at the low wavelength end corresponds to actual corrupted pixel values within the spectrum.

2.3.1 Sky Subtraction: ZAP

Emission from our atmosphere is an additive effect overshadowed by bright galaxy regions and causing greater problems in the fainter galaxy outskirts and for faint objects. Sky subtraction is therefore an important part of the F3D reduction pipeline, preventing lines produced by our own atmosphere from interfering with the galaxy data. As mentioned above, individual MUSE IFUs are treated separately and then combined to create the reduced data cube for each pointing, after which multiple pointings can be combined to create the final cube. During this reduction process, 3 minute sky exposures taken before or after each on-source exposure, are used to create a model of the sky spectrum separately for each spaxel which is then subtracted from the data (Sarzi et al. 2018b).

However, residuals caused by differences between the model and the actual sky lines appear as sharp artefacts. The F3D reduction pipeline post-processes the sky-subtracted data using the Zurich Atmosphere Purge algorithm (ZAP, Soto et al. 2016) [3] to clean these residuals from the entire final combined datacube. The difference between running ZAP before and after combination was assessed and no significant advantages to either method were observed, so ZAP was applied to the entire final datacube at once (Sarzi et al. 2018b).

Although in the majority of cases ZAP behaves as expected, it was found that occasionally spuriously high pixel values are introduced. This problem is illustrated in Figure 2.5, which shows the difference in the datacubes provided by the F3D team for FCC090 before and after ZAP version 1.1 was applied, both Voronoi binned to a target S/N of 100Å^{-1}. Pre-ZAP, all of the spectra appear

[3]Code can be found at https://github.com/musevlt/zap

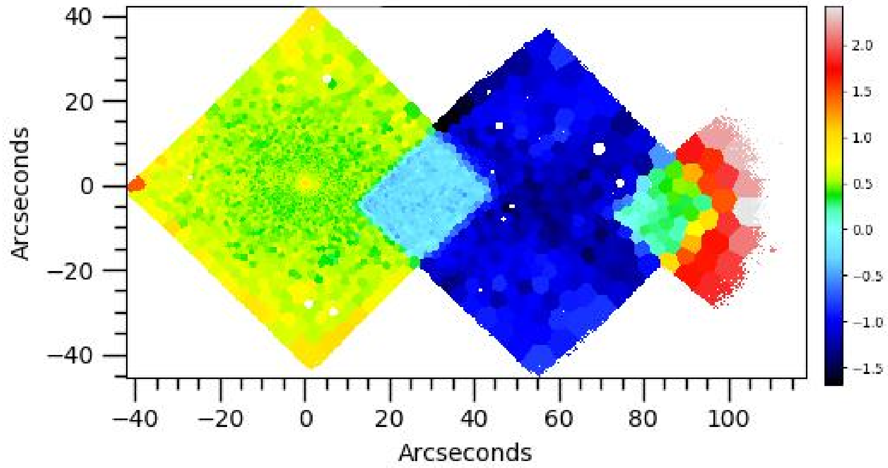

Figure 2.6: Map of the line strength of NaI for FCC167 binned to a S/N target of 100Å^{-1}. The very obvious differences between pointings highlight the differences in the treatment of sky emissions and tellurics for each cube.

smooth, with peaks in the flux where expected for spectral lines. Post-ZAP, several of the spectra have become corrupted, with an extremely high and extremely low intensity pattern occurring at the beginning of these spectra. To illustrate this more clearly, Figure 2.5 also compares the spectra with the highest standard deviation along their length from each cube. Although it needs a little cleaning, the pre-ZAP spectrum still holds its spectral information. However post-ZAP, the spectrum has lost all of its information for wavelengths less than 5400Å. This pattern does not appear in the data before the ZAP algorithm is applied, implying that it is directly caused by ZAP. This problem is currently being addressed by the F3D team, and a fix will be incorporated into the future data reduction pipeline. To reduce the impact of this issue to the current data analysis, an additional selection of the data is imposed such that for each spectrum to be included in a Voronoi bin, the standard deviation of its blue end (4723.5Å-5223.5Å) must be less than 15 times the standard deviation of its red end (7223.5Å-7723.5Å). This excludes any spaxels contaminated by ZAP from contributing to the final Voronoi bins.

2.3.2 Telluric Corrections

Atmospheric (or 'telluric') absorption removes a proportion of light from observations at particular wavelengths, super-imposing the absorption spectrum of Earth's atmosphere on our data. Replacing the data which has been absorbed is a complex process, requiring either a detailed understanding of the absorption spectrum of Earth's atmosphere at the time of observation, or observations of a reference astronomical source with a simple or well-known intrinsic spectrum.

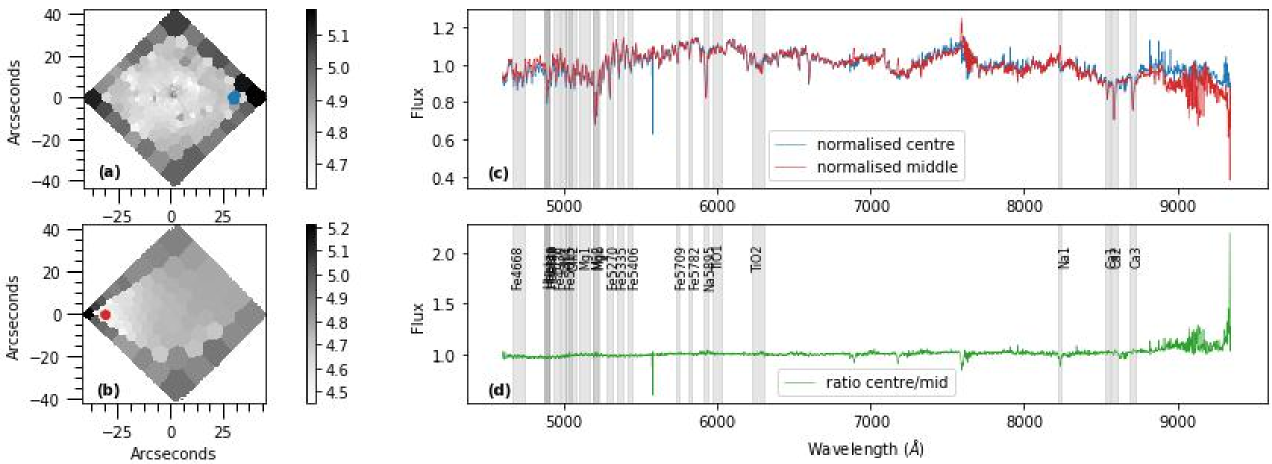

Figure 2.7: *(a)* The central pointing of FCC167 with the bin used for comparison highlighted in blue; *(b)* the middle of the three pointings of FCC167 with the bin used for comparison highlighted in red; these two highlighted bins effectively overlap such that measurements are of the same region on FCC167. *(c)* the normalised spectra for each of these bins, from the centre in blue and middle in red; *(d)* the ratio of these two compared spectra. The indices measured in my pipeline are highlighted in grey. Large differences in the spectra become clear here, particularly towards higher wavelengths.

The F3D reduction pipeline uses the latter approach, taking observations of a spectro-photometric flux calibration star once per observing night. Temporal changes in the atmosphere during the night can, however, introduce differences in telluric absorption between the star and galaxy observations. This means that cubes with combinations of multiple pointings can have very different telluric treatments. The result is an obvious mismatch between the cubes, with an overlapping area combining the differences. The NaI map for FCC167 (Fig. 2.6) shows this issue most noticeably, although it is also apparent in the TiO2 map (Fig. 2.4) and affects the age map (Fig. 2.3).

Taking a bin each (target S/N = 300Å^{-1}) from the overlapping area of FCC167's central and middle pointings before they are combined, Figure 2.7 compares their spectra. The ratio of these two spectra (centre/middle) shows O_2 and H_2O telluric features between 6800Å and 8500Å, which have been over-corrected for in the middle pointing, creating spurious 'emission line' features in the middle pointing spectra. One of these directly affects the NaI line, causing the problems seen in the NaI map. Above 9000Å, spikes in the central pointing may indicate a similar issue due to a different molecular species or vibrational mode, or issues with sky emission subtraction. Since this region is not used in the current analysis, it is not explored further here.

As illustrated here, imperfect correction for telluric absorption and sky emission particularly becomes a problem at the red end of the spectrum. For this reason many astronomers restrict their science to using only up to 7000Å. Unfortunately, this cuts out some interesting indices with respect to the IMF - NaI and the CaT lines. With the large effects from tellurics difficult to account for, these indices are only able to contribute to tracing the IMF if they are used in comparison with other indices. A full-spectrum fitting approach provides information from the cleaner blue end to constrain the fit to the red end, allowing the inclusion of these indices.

The following chapter focuses on the central pointing of FCC167, restricting any errors arising from the treatment of sky emission and tellurics to those from a single pointing which should be self-consistent. The analysis focusses mainly on the wavelengths 4700-7000Å, however tests are also performed on the spectra including the telluric affected red wavelengths up to 9000Å to demonstrate the effects of neglecting red features such as NaI and CaT. A more detailed treatment of telluric absorption (e.g. modelling from first principles using, e.g. MOLECFIT Smette et al. (2015)) is saved for possible future work.

'Curiouser and curiouser!' cried Alice (she was so much surprised, that for the moment she quite forgot how to speak good English).

Lewis Carroll, Alice in Wonderland

3

Constraining the IMF

3.1 From Full Spectrum Fitting: PyStaff

Using a fit for the full spectrum to obtain the IMF is a method that has only become possible relatively recently. The effects of age, metallicity, element abundances and the IMF are now all being routinely considered in stellar population models (Walcher et al. 2009, Vazdekis et al. 2010, Conroy & van Dokkum 2012a, La Barbera et al. 2013, Martín-Navarro et al. 2014, Vazdekis et al. 2015, Spiniello et al. 2015a, Lyubenova et al. 2016, Vazdekis et al. 2016, Spiniello 2016, Sarzi et al. 2018a, Conroy et al. 2018, Vaughan et al. 2018). Spectral information can be spread out over a long wavelength range, so theoretically fitting the entire spectrum allows for the retention of more information than when concentrating on particular localised features. Utilising the full spectrum and allowing for abundance changes enables the correct treatment of blended spectral lines (van Dokkum & Conroy 2012). By including features over a wide range of wavelengths, IMF-insensitive features in the blue can be compared with IMF-sensitive features in the red, separating IMF and abundance effects (Conroy & van Dokkum 2012a). The effects of varying particular element abundances are also allowed to carry through into the line strengths of other elements which would naturally be impacted. For example, since Mg is a major electron donor, changing [Mg/H] affects the ionisation equilibrium, affecting the strength of CaII lines (Conroy et al. 2013).

Python Stellar Absorption Feature Fitting (PyStaff, Vaughan et al. 2018)[1], is a package developed to use the stellar template library of Conroy et al. (2018) to fit the full length of an input spectrum. The Conroy et al. (2018) library contains stellar population synthesis (SPS) models based on the MIST stellar isochrones (Choi et al. 2016, Dotter 2016), and MILES (Sanchez-Blazquez et al. 2006, Falcón-Barroso et al. 2011) and Extended IRTF (Villaume et al. 2017a) stellar spectra libraries. These empirical SPS models cover a range of ages, metallicities and IMFs but are limited to solar neighbourhood abundances. In order to simulate different abundances, theoretical models were used to simulate a new model atmosphere and spectrum for each abundance change. Assuming a Kroupa (2002) IMF, these models are then used to find the relative changes to the spectrum caused by changes in element abundances. These response functions are included in the Conroy models and cover sub- and super-solar abundances for 19 element abundances[2]. They are applied in linear combinations to correct the solar empirical SPS models, mimicking element enhancement or depletion. For more information on how the response functions are created and applied, see Conroy & van Dokkum (2012a) and Conroy et al. (2018).

PyStaff creates a parameter space with the variables recession velocity (v_{syst}) and velocity dispersion (σ); stellar age (1-13.5 Gyr) and metallicity ([Z/H]=-1.5-0.2 dex); IMF slopes x_1 and x_2; all 19 element abundances; emission line velocity, velocity dispersion and strength for Hα, Hβ, NII, SII (6716Å, 6731Å), OIII and OI nebular emission lines; and an error rescaling parameter (denoted ln_f in the plots) giving up to 35 free parameters in total. The error rescaling parameter assumes over- or under-estimated error and scales the noise from the data such that the reduced chi-squared is one and the log likelihood of the fit is maximised (Vaughan et al. 2018). An IMF with a three-part power-law shape is used such that:

$$\Xi(m) = \begin{cases} C_1 m^{-x_1} & 0.08\mathrm{M}_\odot \leq m < 0.5\mathrm{M}_\odot \\ C_2 m^{-x2} & 0.5\mathrm{M}_\odot \leq m < 1\mathrm{M}_\odot \\ C_3 m^{-2.3} & m \geq 1\mathrm{M}_\odot \end{cases} \tag{3.1}$$

[1]Available at https://github.com/samvaughan/PyStaff

[2]Na, Ca, Fe, C, N, Ti, Mg, Si, Ba, [α_s/Fe], Cr, Mn, Ni, Co, Eu, Sr, K, V and Cu; where [α_s/Fe] is a combination of O, Ne and S written as as_Fe in the plots

where the constants C_i are chosen to ensure the continuity of the IMF at all m; x_1 and x_2 vary between 0.5 and 3.5; and the third part is fixed to x_3=2.3 (Salpeter 1955). As an example, a Milky-Way like IMF would have x_1=1.3 and x_2=x_3=2.3 (Kroupa 2002). The Markov-chain Monte-Carlo (MCMC) code **emcee** (Foreman-Mackey et al. 2013) is used to sample this parameter space. A more detailed discussion of PyStaff is presented in Vaughan et al. (2018), where it is used to investigate the IMF within NGC 1399 with MUSE data.

The remainder of this section will describe the tests used to explore the reliability of results obtained from PyStaff, and the code's subsequent application to FCC167 data from F3D. Section 3.2 examines an alternate more selective method for finding the IMF, and lastly Section 3.3 compares the results of the two methods.

3.1.1 Simulating input parameter recovery

In order to establish the reliability of results obtained using PyStaff, the code's ability to recover input values of the different parameters was tested. A few changes to Vaughan et al. (2018)'s usage of PyStaff were made to keep the fit simple. Motivated by the break mass between the Salpeter (1955) IMF and most other Milky Way IMFs occuring at 1M$_\odot$, the IMF powers x_1 and x_2 (Eq. 3.1) were set to be equal. PyStaff is therefore fitting an IMF with only one slope free below 1M$_\odot$, above that being fixed to 2.3. This decision was maintained through all of the following tests, including the application to FCC167. Emission lines were not included in the fit for this test, since the Conroy models are based on empirical stellar spectra and do not include the emission lines caused by ionised gas in galaxies.

Four SSPs from Conroy's models were input into PyStaff, with age 13.5 Gyr, metallicity [Z/H] = +0.2, solar-scaled element abundances, no noise added and varying only the low-mass IMF slope with x_1 = 0.5, 1.3, 2.3 and 3.3 where x_1=2.3 is the Salpeter (1955) IMF. PyStaff was run with 200 walkers taking 10,000 steps, 8000 of which are "burn-in" steps; leaving 4x10^5 samples of the posterior for each spectrum. This test was run twice, once for the full usable wavelength spectrum of the F3D MUSE data, 4700Å-9000Å; and once for a shortened wavelength range, 4700Å-7000Å. The shortened range excludes the red end of the spectra where the MUSE data are most strongly affected by telluric absorption and OH emission. This allows us to test the importance of including or excluding the reddest spectral features (for example NaI and CaT). These wavelength ranges were further split into four shorter ranges which are fit simultaneously: [4700-5600Å, 5600-6800Å, 6800-8000Å, 8000-9000Å] for the red-inclusive spectra, and [4700-5275Å, 5275-5850Å, 5850-6425Å, 6425-7000Å] for

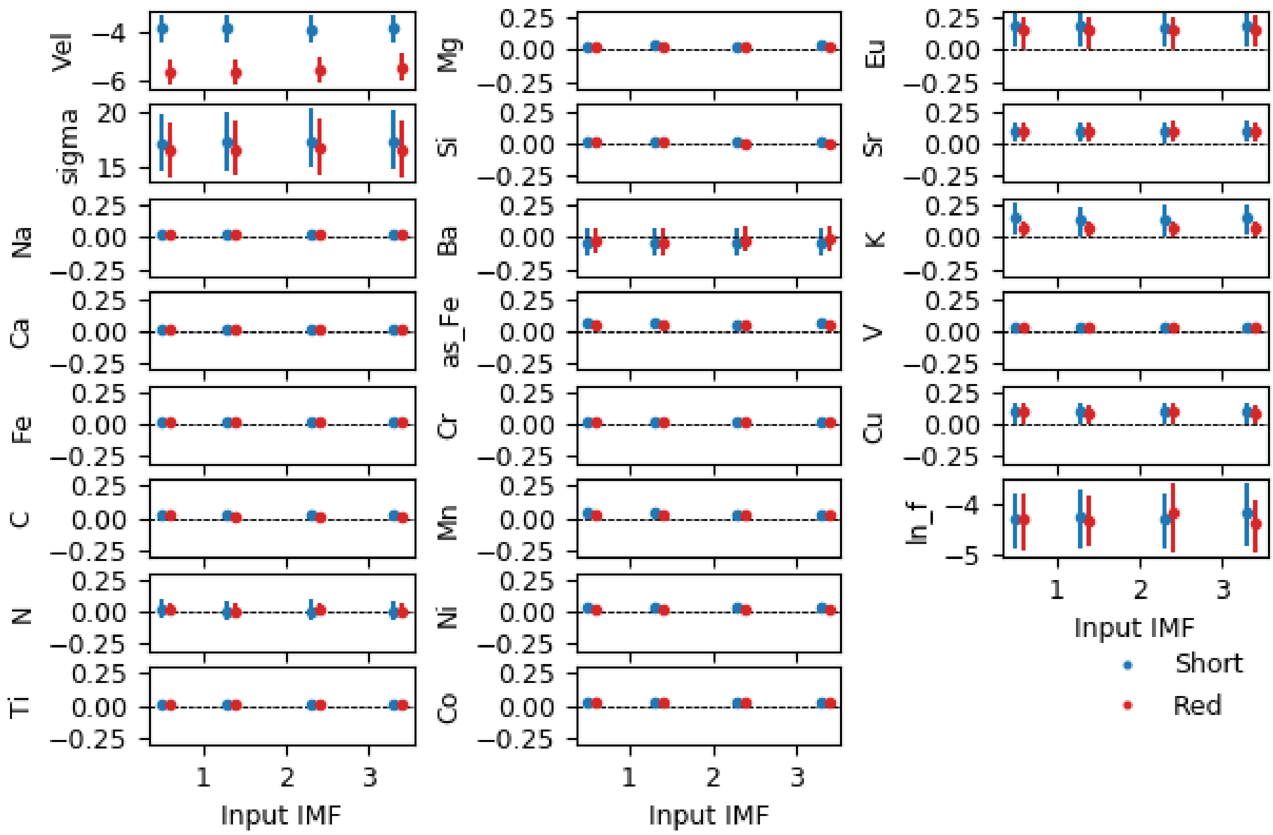

Figure 3.1: PyStaff results (excluding age, metallicity and IMF) for Conroy SSPs with age 13.5Gyr, [Z/H]=+0.2, solar-scaled element abundances and varying low-mass IMF slope (x_1 = 0.5, 1.3, 2.3, 3.3). Results for a shorter wavelength range, 4700-7000Å (blue points) are compared to those for the full wavelength range, 4700-9000Å (red points); both plotted against the input IMF, horizontally offset for clarity. The element abundance expected for a solar-scaled SSP is shown by the black dashed lines in the first two columns. Errors are given by the 1 sigma spread of the MCMC posteriors, though note that, in order to explore systematic fitting issues, no measurement noise was added to the input spectra.

the shortened spectra. Each of these shorter wavelength windows is fit separately, undergoing their own continuum correction.

The results are given in Figures 3.1 and 3.2 and are plotted against the known input Conroy model IMFs with the two wavelength ranges horizontally offset for clarity. In a stellar population with solar-abundances such as in the input Conroy models, the expected element abundance for all elements is zero, which is shown as a black dashed line across all subplots of element abundance in Figure 3.1. The fits for the short (blue points) and red-inclusive (red points) spectra are both consistent with the expected abundance within 1 sigma for the majority of elements, excepting [α_s/Fe], Eu, Sr, K and Cu. Although these element abundances are typically overestimated by PyStaff for both wavelength ranges, the red-inclusive spectrum approaches the expected value more closely. Age, metallicity and the low-mass IMF slope have been plotted as the difference between the expected value from the input

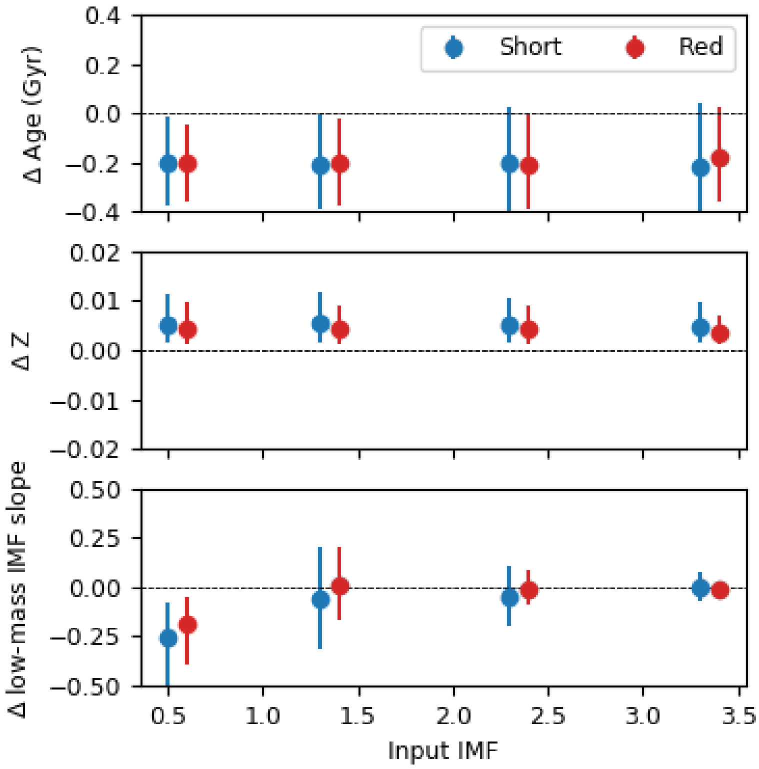

Figure 3.2: PyStaff age, metallicity and IMF results for Conroy SSPs with age 13.5Gyr, [Z/H]=+0.2, solar-scaled element abundances and varying IMF slope (x_1 = 0.5, 1.3, 2.3, 3.3). Results for a shorter wavelength range, 4700-7000Å (blue points) are compared to those for the full wavelength range, 4700-9000Å (red points); both plotted against the input IMF, horizontally offset for clarity. The difference between expected and returned results is plotted. Errors are given by the 1 sigma spread of the MCMC posteriors, though note that, as in Fig. 3.1, no measurement noise was added to the input spectra for these tests.

Conroy model and the retrieved value from PyStaff in Figure 3.2. PyStaff consistently returns an age approximately 0.2 Gyr older than expected, and a metallicity 0.05 dex less than expected. However, PyStaff is very well able to return the expected low-mass IMF for values greater than $x_1 \approx 1.0$. Below this value PyStaff tends to overestimate the low-mass IMF slope, returning a more bottom-heavy IMF than expected. Since the contribution of low mass stars to the integrated light is at most a few percent, at the very shallow IMF slopes below $x_1 \approx 1.0$, this contribution decreases to minuscule amounts and the low-mass IMF becomes more and more uncertain. Due to the greater amount of information included in the red-inclusive spectrum, it is affected less than the shorter spectrum. We can conclude that in the absence of significant systematic errors (e.g. due to telluric absorption or sky emission), including the red end does have a positive affect on PyStaff's ability to fit the spectrum, although it is not necessary for finding more bottom-heavy low-mass IMFs.

3.1.2 Testing with published reference data

The second test applies PyStaff to relatively well-known, clean data obtained from stacked SDSS (York et al. 2000) spectra. La Barbera et al. (2013) defined a sample of nearby ETGs (bulge-dominated systems) with absolute B-band magnitude brighter than -19, central velocity dispersion $\sigma_0 \geq 100\,\mathrm{km\,s^{-1}}$, and low internal extinction from SDSS Data Release 6 (Adelman-McCarthy et al. 2008). 24,781 ETGs were stacked in 18 bins of σ_0 with width 10 km s^{-1}. The stacked spectra for the σ_0 = 120-130, 180-190 and 240-250 km s^{-1} bins which have been created using 2452, 1711 and 340 ETGs respectively (La Barbera et al. 2013) have been obtained (La Barbera, by private communication).

By applying PyStaff to this well-tested data, its ability to recover similar results to previous work using different methods was evaluated. As in Section 3.1.1, the low-mass IMF powers x_1 and x_2 were set to be equal, and the test was applied to both a shortened wavelength range (4700Å-7000Å) and a longer red-inclusive range (4700Å-8700Å). The slightly shorter wavelength range for the red-inclusive spectrum as compared to the test in Section 3.1.1 is due to PyStaff's requirement for a buffer between the fit length and the end of the shorter SDSS spectra. Since the SDSS data are comprised of stacked galaxies which may contain ionised gas, emission lines were introduced into the fit in this test.

Figure 3.3 displays the results from PyStaff for the tests on SDSS spectra compared with results from Conroy et al. (2013, Table 1) and La Barbera et al. (2013, Fig. 14). Conroy et al. (2013) similarly use full-spectrum fitting to fit passive galaxies from the SDSS Main Galaxy Survey (Strauss et al. 2002) Data Release 7 (Abazajian et al. 2009) which are stacked into seven velocity dispersion bins. The fit is based on the SPS models developed by Conroy & van Dokkum (2012a), precursors to the Conroy et al. (2018) models used by PyStaff, allowing for varying abundance patterns[3] and age. Each of the element abundances have been plotted on the appropriate PyStaff results panel. Conroy et al. (2013) found that their error budget was dominated by systematic rather than statistical errors, but that these were probably < 0.05 dex, which is smaller than the symbol size in many instances in Figure 3.3. Note that since [α_s/Fe] in PyStaff is dominated by oxygen, the [O/Fe] abundances from Conroy et al. (2013) have been compared with this variable. The results in general agree very well. The most significant difference is the overall lower N abundances found by PyStaff (by ≈0.3 dex). C and V as found by PyStaff also differ on a less substantial scale (by ≈0.1-0.2 dex). Interestingly, unlike in the tests from Section 3.1.1, it is the shorter spectrum (blue points in Fig. 3.3) which agrees best with the Conroy et al. (2013) results.

[3]Including the elements Na, Ca, Fe, C, N, Ti, Mg, Si, O, Cr, Mn, N, Co and V

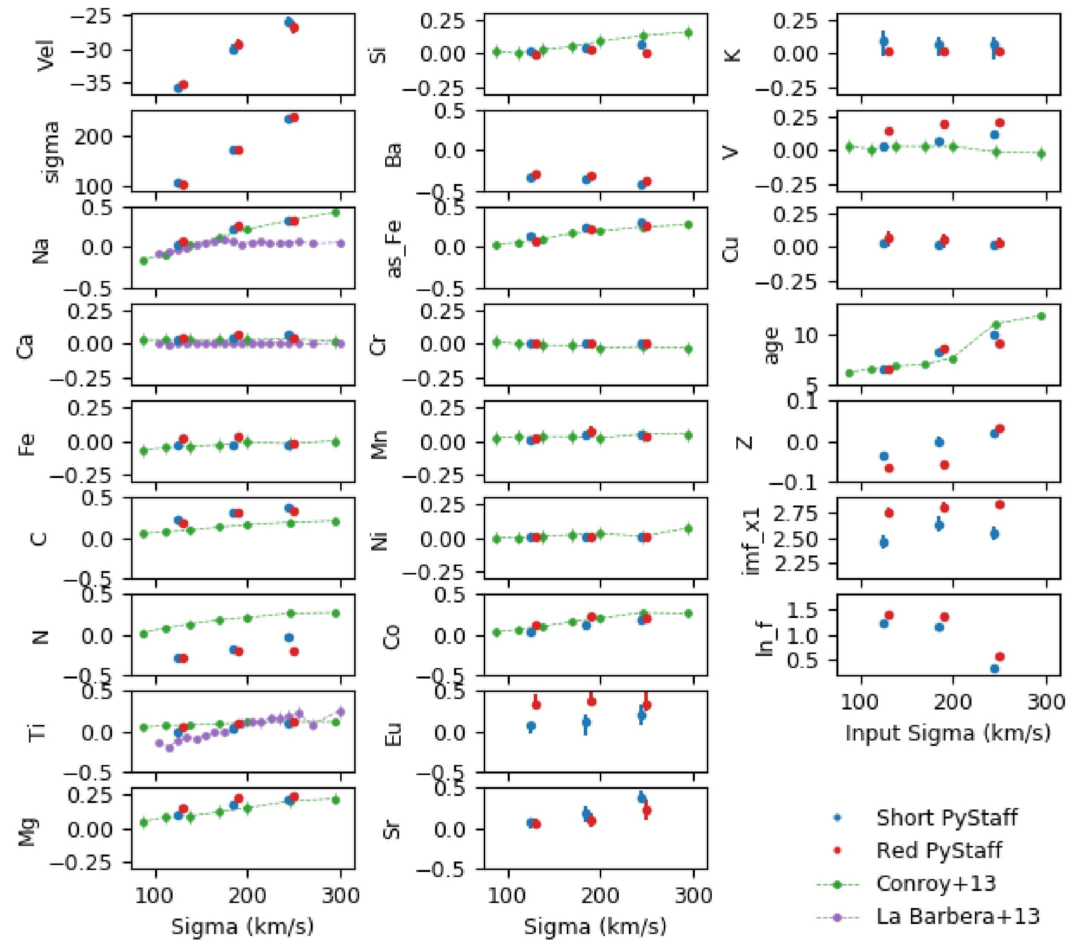

Figure 3.3: PyStaff results for SDSS binned spectra with varying sigmas (σ=120-130, 180-190 and 240-250 km s^{-1}). Results for the short 4700-7000Å (blue points) and red-inclusive 4700-9000Å (red points) wavelength ranges are plotted against the input σ, horizontally offset for clarity. PyStaff errors are given by the 1 sigma spread of the MCMC posteriors. Comparison is made to results from Conroy et al. (2013) (green points) and La Barbera et al. (2013) (purple points). Conroy et al. (2013) find systematic errors < 0.05 dex. La Barbera et al. (2013) give errors < 0.1 dex. Most of the formal errors are smaller than the symbol size here. Note that [O/Fe] from Conroy & van Dokkum (2012b) has been plotted in the as_Fe panel.

La Barbera et al. (2013) use 10 spectral indices[4] to obtain results using stacked spectra in 18 different sigma bins including the same three stacked spectra as input here into PyStaff. Any differences between these results should therefore be associated with the difference in method. First correcting their spectral indices to solar abundances ([α/Fe] = 0), La Barbera et al. (2013) then fit each index using a linear combination of two extended MILES (MIUSCAT; Vazdekis et al. 2012, Ricciardelli et al. 2012) simple stellar population models with the same IMF, but different ages and metallicities, and model the abundances using the Conroy models. The residual element abundances from this

[4] IMF sensitive indices Mg4780, TiO1, TiO2$_{SDSS}$, Na8190$_{SDSS}$ and CaT; abundance sensitive indices NaD and Ca H&K; and age and metallicity sensitive indices Hβ_0, Hγ_F and [MgFe]'. For definitions see La Barbera et al. (2013).

process for [Na/Fe], [Ca/Fe] and [Ti/Fe] have been compared with the results from PyStaff in Figure 3.3. Errors were given by La Barbera et al. (2013) at the 1 sigma level, most of which are smaller than the symbol size in Figure 3.3. All of the results for [Ca/Fe] agree well; however those found for [Ti/Fe] and [Na/Fe] have some differences. The results for [Ti/Fe] are consistent both with PyStaff and Conroy et al. (2013) for velocity dispersions greater than 200 km s^{-1}, but have a slightly stronger trend towards greater Ti depletion below this value. Similarly, [Na/Fe] agrees well with both PyStaff and Conroy et al. (2013) for velocity dispersions less than about 200 km s^{-1}, however the values from La Barbera et al. (2013) flatten at greater sigma while PyStaff and Conroy et al. (2013) find a stronger positive trend. PyStaff's greater agreement with Conroy et al. (2013) is likely due to the use of similar SSP models when fitting the spectra. Spiniello et al. (2015a) find that due to different underlying assumptions when the models were created, MILES and Conroy models treat Na and, to a lesser extent, Ti differently, causing different predictions of their abundance patterns. These differences contribute to the inconsistencies in the published results that we see in Figure 3.3.

The overall agreement of PyStaff with published results indicates its reliability. Combining the results of this test on known SDSS data with the results from the above test on known Conroy models, we conclude that except for data with very shallow IMF slopes, the results returned by PyStaff are reliable and compare well with other similar studies. We also conclude that very little information is lost when shortening the spectrum to avoid the systematic errors caused by telluric absorption and sky lines.

3.1.3 Establishing a reduced set of free parameters

Although PyStaff does a reliable job of fitting all 35 of its free parameters, the fit takes on average 4 hours per spectrum to complete using parallelisation on a modern 50-core server. While this time frame is acceptable when only fitting a few spectra as done in the tests above, it is not practical for use on MUSE data cubes containing hundreds or thousands of spectra. To use the F3D MUSE data to its fullest capacity, producing spatially resolved maps of changes in the IMF, requires a process with a shorter run time. With this in mind, we have fixed to solar abundances all elements which, for a +0.3 dex change in abundance (except for Carbon, where we used a change of +0.15 dex), cause variations less than 2% from a solar-scaled SSP (see Fig. 3.4). This leaves 11 varying elements, decreasing the number of free parameters to 27. With a smaller parameter space to explore, we are also able to decrease the number of MCMC walkers.

We verified that decreasing the number of free variables in this manner did not introduce bias in the recovered values whether using the shortened or red-inclusive wavelength ranges (see Appendix

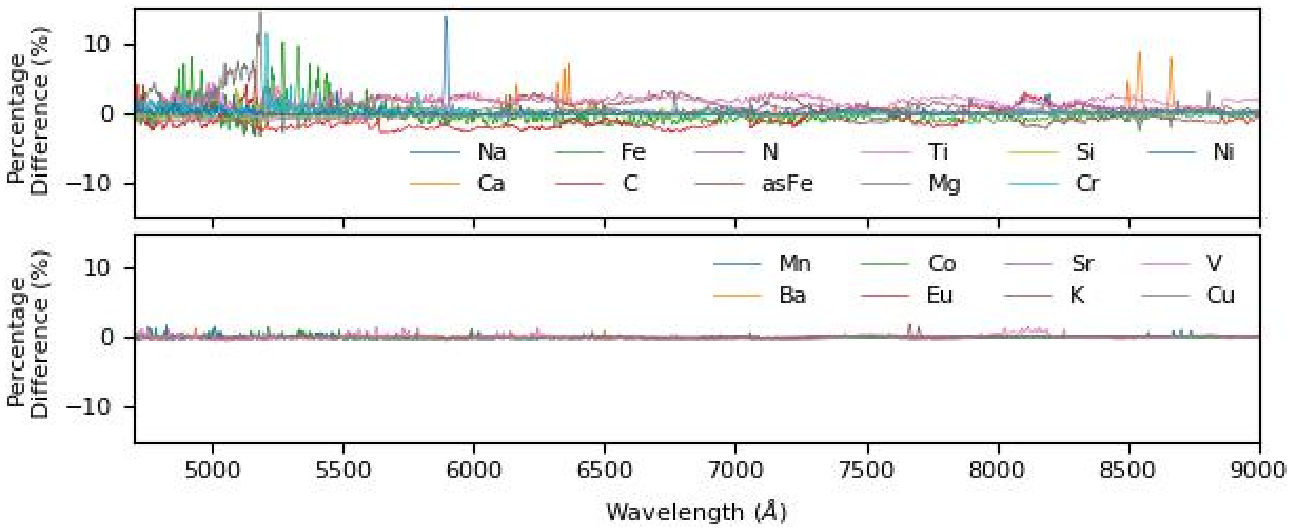

Figure 3.4: Percentage difference between each element abundance response function (+0.3 dex; except for C where +0.15 dex was used) and a solar-scaled SSP of the same age and metallicity across the MUSE wavelength range. *Top:* Response functions varying at a greater than 2% level. *Bottom:* Response functions varying less than 2%.

Fig. 24 and 25). Computational time was decreased by over 80% on average. This is therefore a feasible method for application to FCC167, and in particular in future to the remainder of the F3D data in a more practical time frame.

3.1.4 Application to FCC167

Having tested PyStaff on both models and well-known data and concluded that it recovers known parameters well, we now apply it to FCC167, one of the F3D galaxies. Nine bins have been chosen to fit using PyStaff. These bins are taken only from the central pointing of FCC167 to avoid problems caused by differences in the treatment of tellurics and sky lines across the combined cube (see Chapter 2.3). The selected bins are portrayed in Figure 3.5. Chosen such that bulge, disk and off-disk locations are all represented, each bin apart from the central one has a pair on a similar isophote. Using bins off the plane of the disk enables us to probe the fainter extents of the galaxy without needing to use other pointings that may suffer from different systematic errors due to telluric absorption or sky emission corrections (see Chapter 2.3).

As in the tests above, we have kept the low-mass IMF powers x_1 and x_2 set to be equal, and have performed the fit using both the shortened (4700-7000Å) and red-inclusive (4700-9000Å) wavelength ranges. Emission lines were also included in this fit. We have chosen to set eight of the element abundance variables to solar abundance as described in Section 3.1.3 above, as this significantly

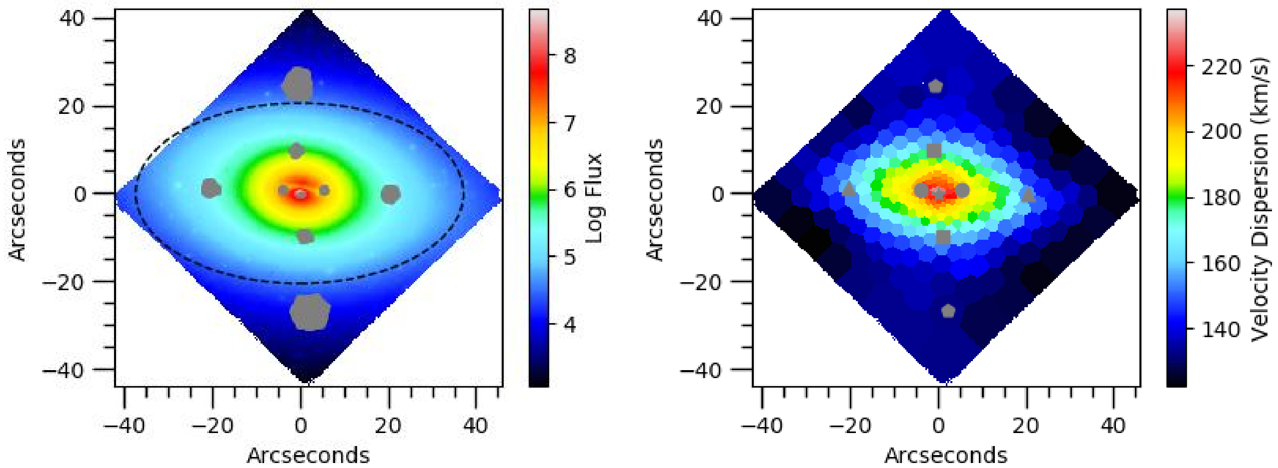

Figure 3.5: Positions of the nine bins from FCC167 fit with PyStaff. *Left:* the shape and size of the bins are imposed on an unbinned, logarithmic image of the total flux of the galaxy. The black dashed ellipse gives the B-band effective radius of FCC167 of 0.62 arcmin (Ferguson 1989, Sarzi et al. 2018b). *Right:* the position of the bins are given on a map of the velocity dispersion, binned to a S/N of 300. Isophote paired bins are given the same marker shapes, so that we have five distinct markers to carry into the following plots.

decreased the computation time. Examples of the fit that PyStaff returns are given in Figures 3.6 and 3.7 for the short and red-inclusive wavelength ranges respectively.

The results are given in Figures 3.8 and 3.9 plotted against the velocity dispersion, σ found for each bin using pPXF (Chapter 2.2.2). The error bars show the 1 sigma spread of the MCMC posteriors. The large difference between the velocity dispersion found by PyStaff and pPXF is likely due to different assumptions within the codes made for the instrument resolution when comparing the models and the data. PyStaff and pPXF are based on two separate models and this may have had an effect on the velocity dispersion calculated. As the focus of this thesis is on the stellar population parameters rather than the kinematics, we simply apply a constant correction offset value of 120 $\mathrm{km\,s^{-1}}$ in quadrature to the PyStaff dispersion values in all following plots to bring them into line with the pPXF values. The figures show remarkably similar results for each isophote pair, illustrating that although the bins are on opposite sides of the galaxy, the environments are quite similar. The shortened spectra are plotted along with the red-inclusive spectra, showing good agreement with each other despite the issues caused by telluric absorption and sky emission which affect the red end of the spectrum. The biggest differences occurred in the returned age, metallicity and IMF slope for some high sigma bins, and in Ca and Ti for low sigma bins. A difference in the Ca results was expected, as the Ca triplet lines are included in the red-inclusive spectra but excluded from the shorter spectra.

From Figure 2.3, we know that velocity dispersion increases towards the centre of FCC167.

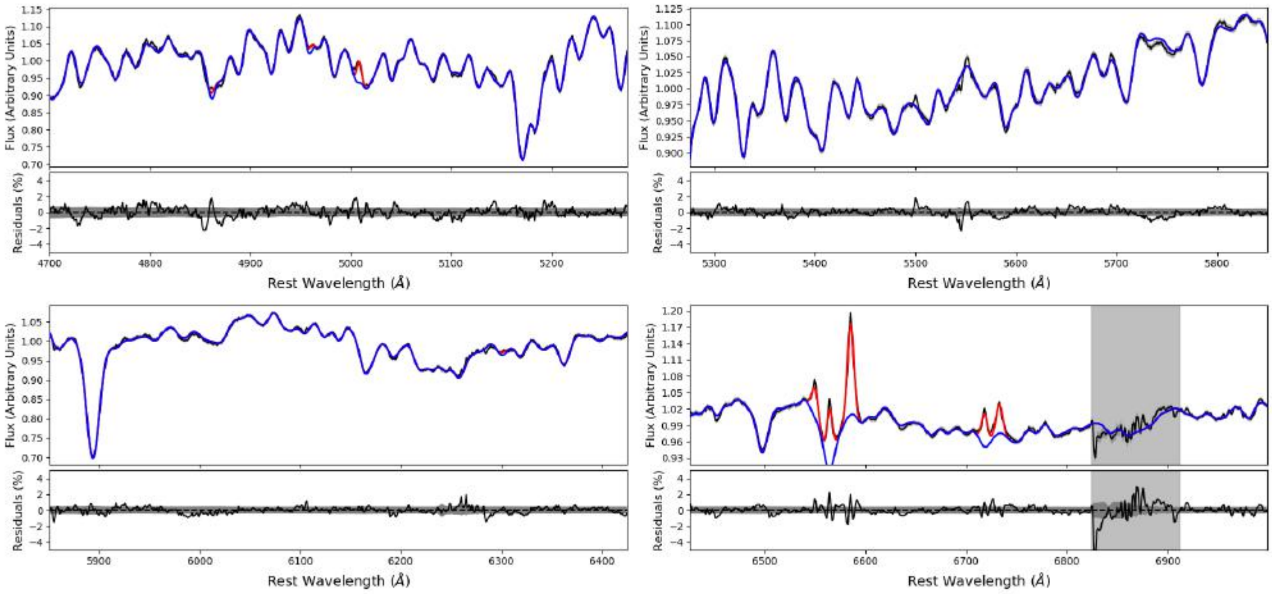

Figure 3.6: Example of PyStaff's fit for the central bin of FCC167 using the short wavelength range (4700-7000Å). Grey shaded regions are areas of particularly intense residual telluric absorption or emission which have been excluded from the fit. Where PyStaff has fit emission lines are given in red.

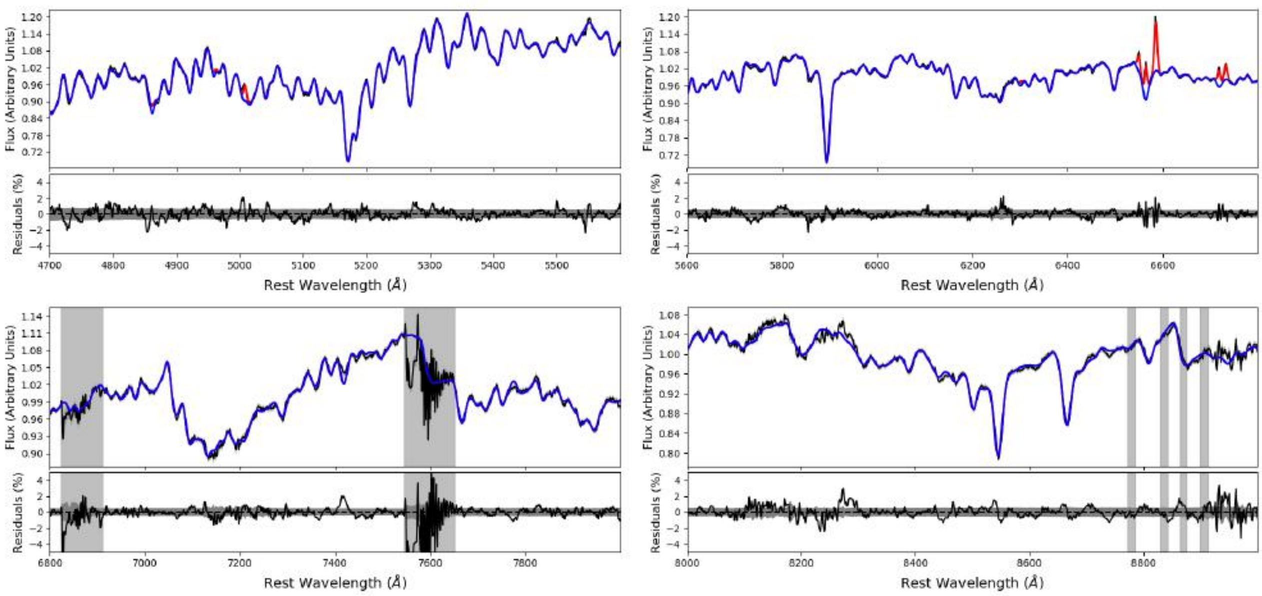

Figure 3.7: Example of PyStaff's fit for the central bin of FCC167 using the red-inclusive wavelength range (4700-9000Å). The effects from telluric absorption and sky emission can be clearly seen around 8200Å and towards the end of the spectrum. Grey shaded regions are areas of particularly intense residual telluric absorption or emission which have been excluded from the fit. Where PyStaff has fit emission lines are given in red.

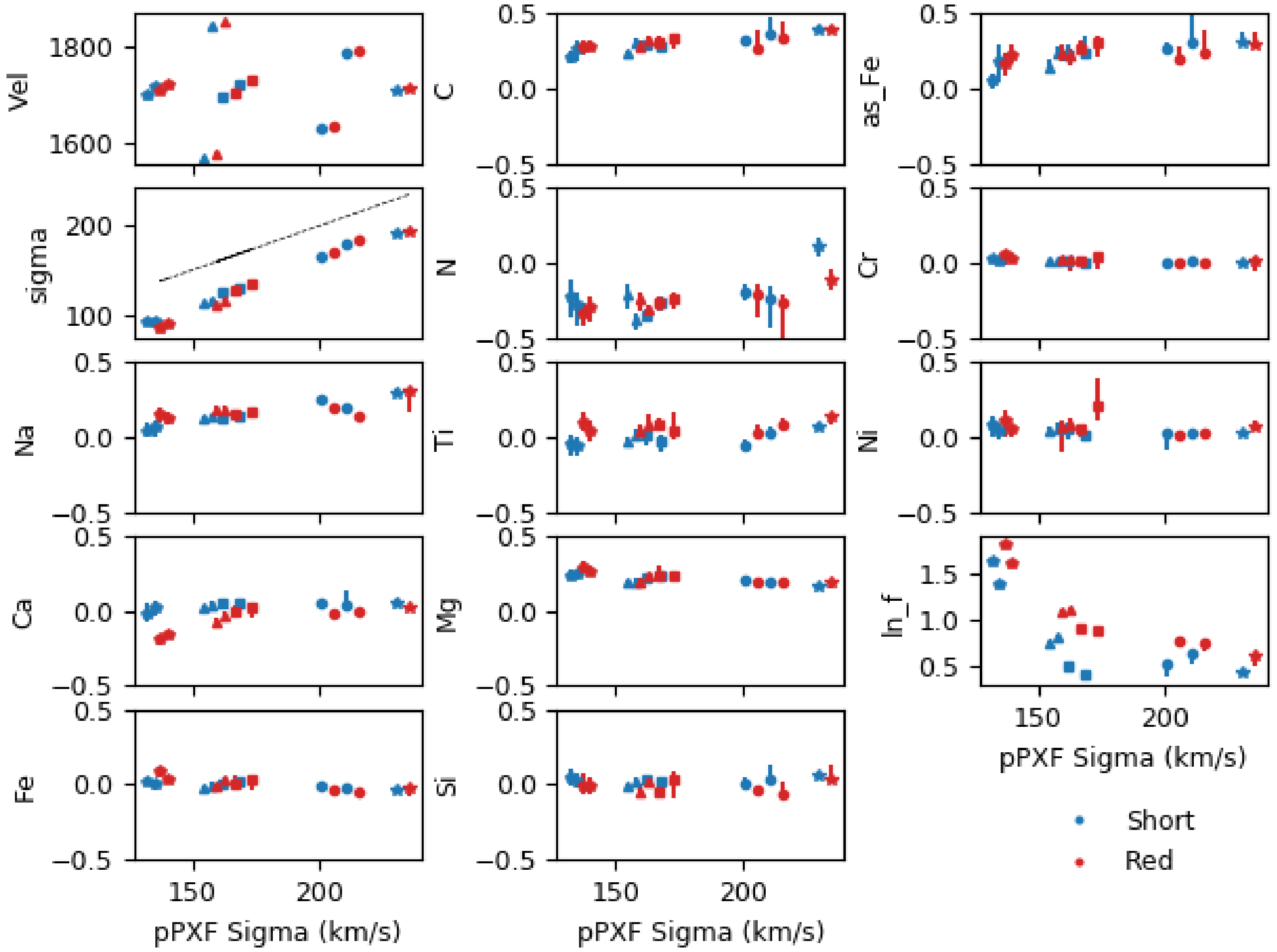

Figure 3.8: PyStaff results for nine bins from FCC167. Results for the shorter wavelength range, 4700-7000Å (blue points) are compared to those for the full wavelength range, 4700-9000Å (red points); both plotted against the velocity dispersion found using pPXF (Chapter 2), horizontally offset for clarity. Isophote paired bins are given the same marker shapes. Errors are given by the 1 sigma spread of the MCMC posteriors. Black dashed line in the sigma subplot represents the values found for each bin using pPXF (more detail in text).

Assuming then that increasing sigma can be equated to decreasing radius we can compare to the mass-weighted age and metallicity maps presented from pPXF. PyStaff agrees with a relative increase in age towards the centre of FCC167. However, contrary to the mass-weighted metallicity map which suggests only a very weak radial gradient decreasing in metallicity towards the centre of the galaxy, PyStaff suggests a strong increasing metallicity gradient towards the galactic centre.

Overall, the steepest trends in element abundances occur for Na, N and [α_s/Fe], all of which increase in strength towards the galactic centre. Interestingly, the low-mass IMF slope appears to decrease towards the galactic centre. Figure 3.9 shows a clear trend towards a flatter than Salpeter low-mass IMF at the centre, with a more bottom-heavy result at larger radii.

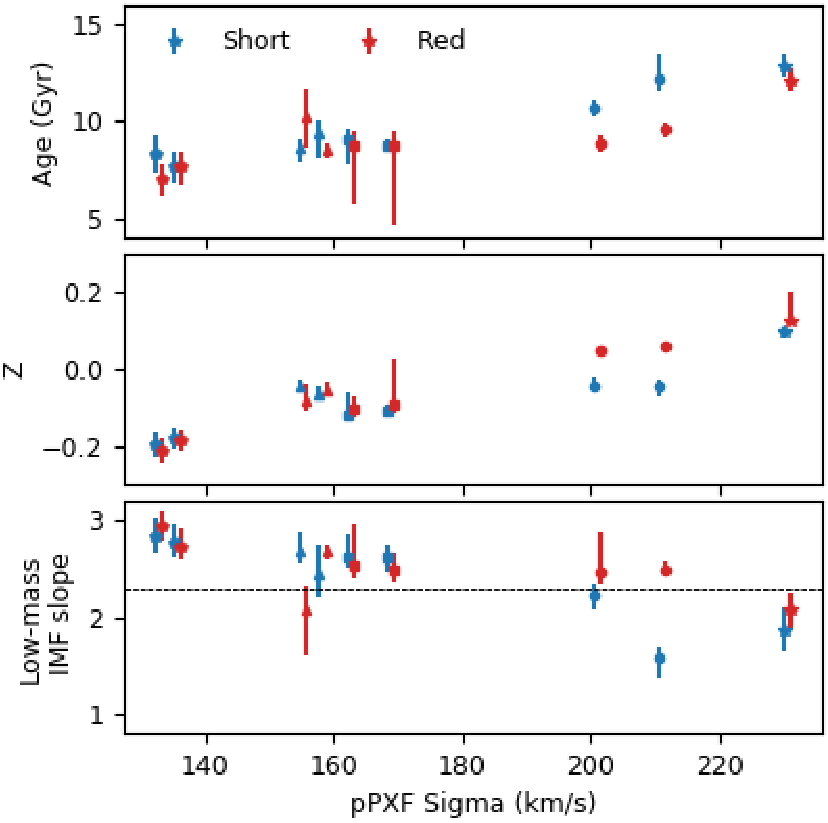

Figure 3.9: PyStaff results of age, metallicity and low-mass IMF slope for nine bins from FCC167. Results for the shorter wavelength range, 4700-7000Å (blue points) are compared to those for the full wavelength range, 4700-9000Å (red points); both plotted against the velocity dispersion found using pPXF (Chapter 2), horizontally offset for clarity. Isophote paired bins are given the same marker shapes. Black dashed line in low-mass IMF slope subplot shows the Salpeter IMF value. Errors are given by the 1 sigma spread of the MCMC posteriors.

3.2 Selective Spectral Fitting

The majority of IMF studies to date have restricted their consideration of spectra to the use of specific absorption features due to the majority of spectral information being concentrated in these regions (e.g. van Dokkum & Conroy 2010, Ferreras et al. 2012, Spiniello et al. 2012, La Barbera et al. 2013, Spiniello et al. 2014, Martín-Navarro et al. 2014, La Barbera et al. 2016a,b, Sarzi et al. 2018a, Vaughan et al. 2017, Rosani et al. 2018, Parikh et al. 2018). For this reason, we have chosen to compare our results, based on fitting the largest number of spectral pixels possible with maximum freedom of parameters, with those from a second method based on a much more restricted fitting approach focussing on a few select features.

This second method, under development by Martín-Navarro et al. (by private communication), concentrates on fitting particular regions of the spectrum which are considered to be most impacted by changes in the stellar population parameters, hence we refer to this approach as 'Selective Spectral

Fitting' (SSF). Well-known index bandpasses are used to define the wavelength boundaries of the fitted regions. Here, 6 separate wavelength regions containing the standard indices Mgb5177, Fe5270, Fe5335, TiO2, TiO1 and aTiO are used to constrain the free parameters of the final fit.

As a preliminary step, the template weights from a regularised solution of pPXF are used to find the age and metallicity (with the IMF slope also left free), velocity and velocity dispersion of a spectrum. The age, velocity and velocity dispersion are then fixed to these resulting values in the next stage of the process, while the derived metallicity and IMF slope are used as Gaussian priors, with standard deviations of around 0.05 and 0.1 respectively. The selected index-defined spectral regions are then fitted with MILES models (Vazdekis et al. 2015) combined with Conroy's response functions (Conroy & van Dokkum 2012a), using an MCMC approach (Foreman-Mackey et al. 2013)[5] with the aim of minimising the difference between the best-fitting model and the data for all spectral regions simultaneously. The free parameters of this fit are the IMF, [Z/H], [Mg/Fe] and [Ti/Fe]. The IMF shape assumed here is the bimodal form of the MILES models (Vazdekis et al. 1996):

$$\Xi(m) = \begin{cases} \beta 0.4^{-\mu} & m < 0.2\mathrm{M}_\odot \\ \beta p(m) & 0.2\mathrm{M}_\odot < m < 0.6\mathrm{M}_\odot \\ \beta m^{-\mu} & m \geq 0.6\mathrm{M}_\odot \end{cases} \tag{3.2}$$

where $p(m)$ is a spline (see Vazdekis et al. 1996). This restrictive version of the IMF was originally based on fitting the observational results from Scalo (1986) and Kroupa et al. (1993).

Concentrating on particular short regions of the spectrum in this way focuses the fit on areas where a changing IMF ought to have the greatest impact. The computing time is also decreased considerably, bringing the total time down to a few minutes per spectrum. SSF was applied by Ignacio Martín-Navarro to the same nine spectral bins from FCC167, and the results provided by private communication. We compare the results from these two approaches in the following section.

3.3 Comparing results from the two methods

In Figure 3.10, the recovered parameters in common between PyStaff and Selective Spectral Fitting (SSF) (velocity dispersion, age, metallicity, [Mg/Fe] and [Ti/Fe]) are compared as a function of the velocity dispersion derived in Chapter 2 using pPXF for each respective bin. There is reasonable

[5]http://dfm.io/emcee/current/user/line/

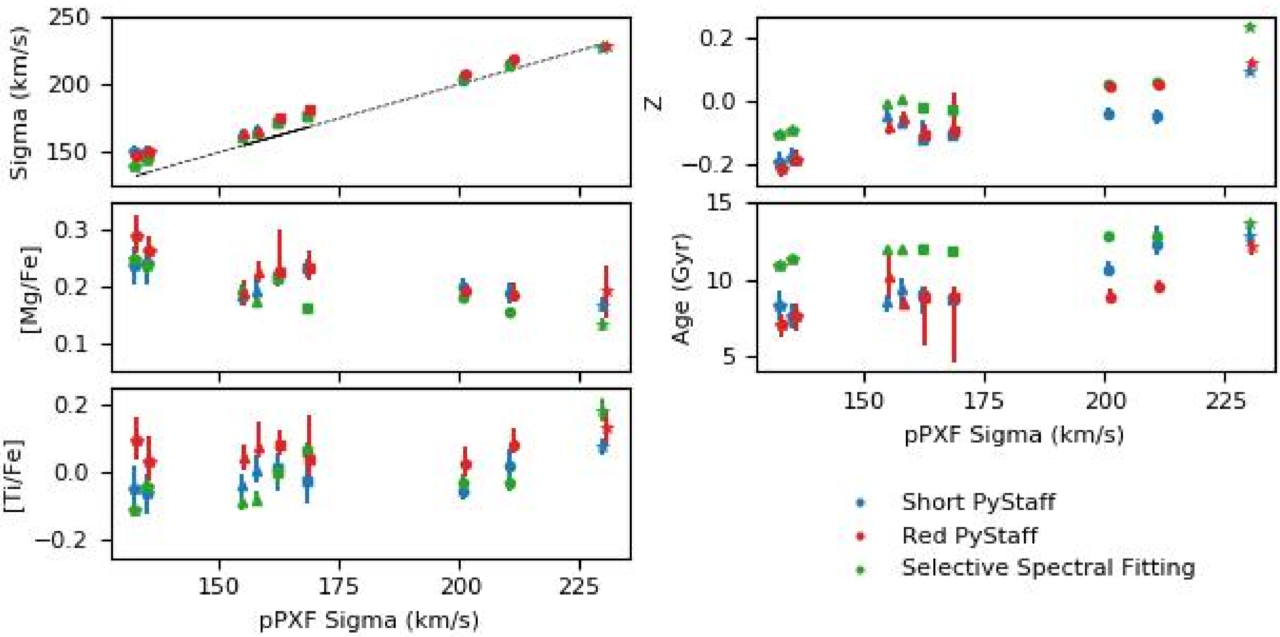

Figure 3.10: Results from both PyStaff and Selective Spectral Fitting (SSF, Martín-Navarro et al.), comparing the two wavelength ranges from PyStaff with a slight horizontal offset for clarity. All results have been plotted against the velocity dispersion found with pPXF (Chapter 2). Isophote paired bins are given the same marker shapes. Error bars represent the 1 sigma uncertainty, being smaller than the symbol size in many cases. Sigma values from PyStaff have been corrected in quadrature to adjust for differences in the assumed instrument resolution. The dashed line in the sigma subplot (top left) shows the values found using pPXF.

agreement between the two methods, with the strongest agreement generally occurring for the shorter wavelength range fitted with PyStaff. This should be expected, as SSF focuses on index bandpasses within the 4700Å to 7000Å wavelength range and does not include any from the extended red-inclusive spectral range (see Fig. 3.13). However this is not the case for metallicity, where the red-inclusive PyStaff fit agrees best with SSF for high sigma bins. An explanation for this anomaly is that SSF uses a metallicity found from pPXF as a prior, therefore utilising more of the spectrum bringing it more in line with PyStaff. The greatest disagreement for the general results occurs for the ages below a velocity dispersion of 200 km/s, where PyStaff returns ages younger by roughly 3 Gyr. This is consistent with the difference found between PyStaff and pPXF results, where pPXF also finds ages older by 3 Gyr than PyStaff (note that SSF utilises an assumed age derived from pPXF). However, despite this discrepancy in the numerical values, the trend of increasing age with increasing velocity dispersion agrees very well across both PyStaff and SSF.

Although both methods return an IMF ‘slope’ parameter, due to the different IMF shapes assumed (Equations 3.1 and 3.2) these values cannot be directly compared. Instead, the ratio of the IMF at $0.4M_{\odot}$ and $4M_{\odot}$ has been calculated for each using their respective equations, and the results

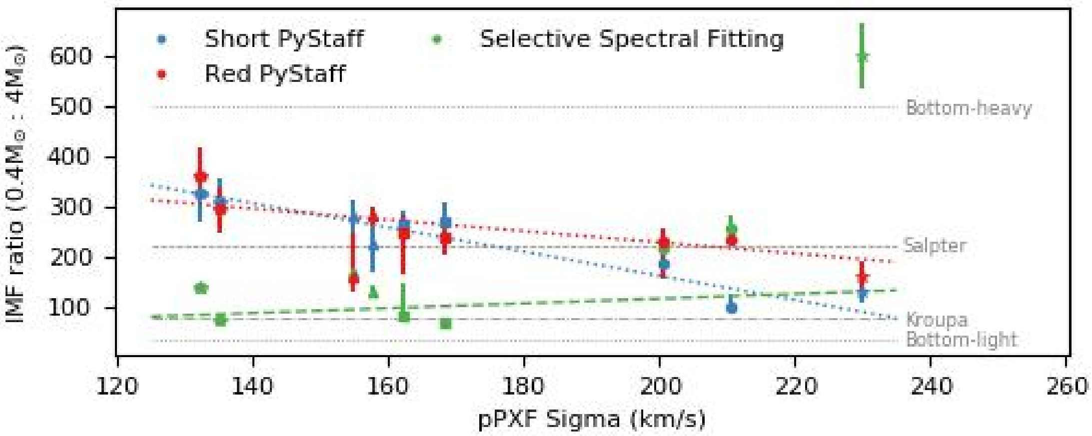

Figure 3.11: The ratio of the IMF at 0.4M$_\odot$ and 4M$_\odot$ calculated using Equation 3.1 for the PyStaff results (blue and red points) and Equation 3.2 for the SSF results (green points) for each bin plotted against the velocity dispersion found using pPXF (Chapter 2). Isophote paired bins are given the same marker shapes. These points have then been fit with an error-weighted polynomial of degree one with gradients of -2.38 ± 0.47, -1.11 ± 0.42 and 0.47 ± 1.15 for the short PyStaff (blue dotted line), red-inclusive PyStaff (red dotted line) and SSF (green dashed line) slopes respectively. The ratios for bottom-heavy (x=3.3 below 1M$_\odot$, x=2.3 above 1M$_\odot$), Salpeter (x=2.35), Kroupa (x=1.3 below 0.5M$_\odot$, x=2.3 above 0.5M$_\odot$) and bottom-light (x=0.5 below 1M$_\odot$, x=2.3 above 1M$_\odot$) IMFs have been plotted and labelled in grey for comparison.

plotted in Figure 3.11. Error weighted one degree polynomial fits to these results recover gradients of -2.38 ± 0.47, -1.11 ± 0.42 and 0.47 ± 1.15 for the short PyStaff (blue dotted line), red-inclusive PyStaff (red dotted line) and SSF (green dashed line) slopes respectively. The SSF polynomial fit is consistent with either a single IMF value across the galaxy or a shallow increase in bottom-heaviness of the IMF towards the galactic centre. This is in contradiction to the PyStaff results, which show a decreasing dwarf to giant star ratio. Although the slopes of both cases are mild, there is a 6 sigma difference between the gradient of the short range PyStaff fit points and the gradient from SSF. The results are not consistent with each other.

To confirm whether the ratio is representing the entire shape of the IMF accurately, the entire IMF shape of the first, seventh and last bins from Figure 3.11 has been plotted in Figure 3.12 from both PyStaff (short range) and SSF. Along with the low-mass IMF slope, the velocity dispersion is given for each line. The spread of the 1 sigma error is represented using transparency, where the denseness of the lines causes a darker colour marking the mean value of the Gaussian. The different shapes used for the IMF does affect the ratio of 0.4M$_\odot$ to 4M$_\odot$. While the PyStaff slope is fixed above 1M$_\odot$, the IMF definition used for SSF is not fixed above 1M$_\odot$. This means that as the velocity dispersion decreases and the low-mass SSF IMF slope flattens, its high-mass IMF slope also flattens, giving a higher number of stars per logarithmic mass bin at any given mass above 1M$_\odot$. The net result is that

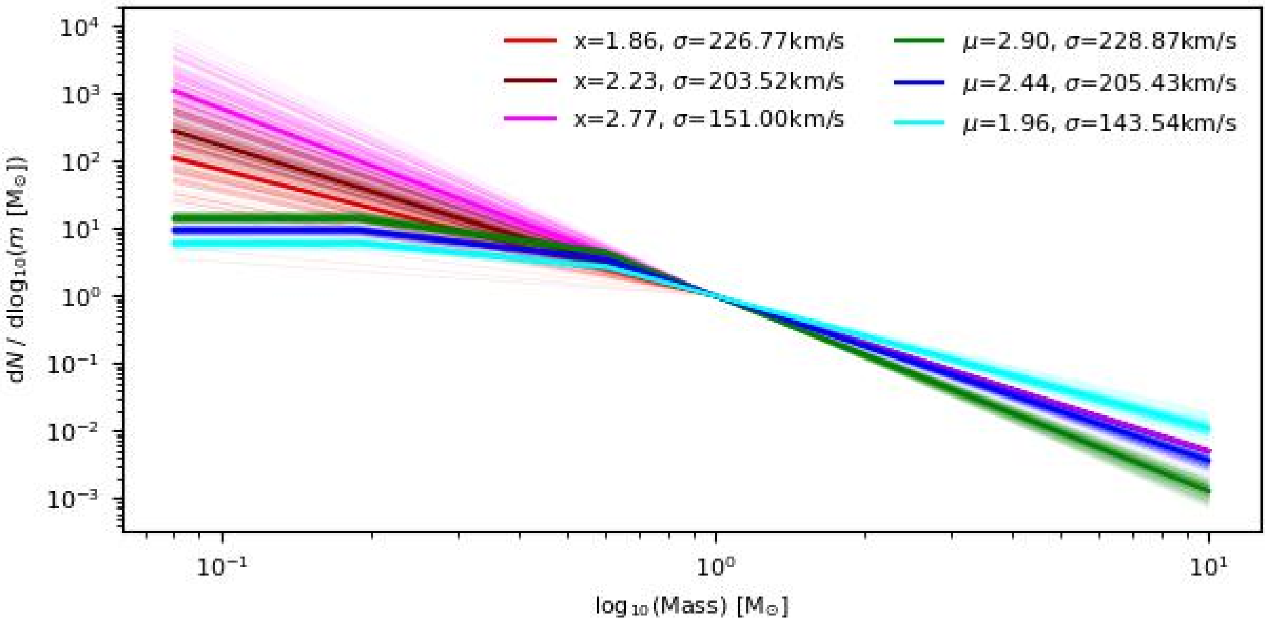

Figure 3.12: The shapes of the returned IMFs from PyStaff (red, maroon and fuchsia) and SSF (green, blue and cyan) normalised at $1M_\odot$ to 1 for three of the FCC167 bins. Each line has its one sigma error shape shaded around it. Velocity dispersions given for the PyStaff lines have been corrected in quadrature to adjust for differences in the assumed instrument resolution. Note that 'x' and 'μ' refer to the slope parameters of Eq. 3.1 for PyStaff and Eq. 3.2 for SSF respectively.

the ratio we calculated for Figure 3.11 changes far faster with changing velocity dispersion for the SSF IMF model than for PyStaff. The dwarf to giant ratio also depends somewhat arbitrarily on the values chosen for calculation; if smaller mass values had been chosen, the ratio would be much greater for PyStaff where it would stay quite similar for SSF. Notwithstanding these comments, Figure 3.12 shows that the low-mass slope of the IMF is steepening with decreasing sigma for PyStaff (becoming more bottom-heavy at larger radii), and flattening with decreasing sigma for SSF (becoming more bottom-heavy towards the centre of the galaxy). This is an interesting contradiction considering that the remainder of the results (i.e. metallicity, [Mg/Fe], [Ti/Fe] and the shape of the age curve) agreed well.

One explanation may be that although the indices used by Martín-Navarro et al. are designed to capture the majority of the spectral information available to determine the IMF, there is still some information left in the spectrum which PyStaff utilises to fit its IMF. Figure 3.13 shows three Conroy SPS models of the same age and metallicity with varying low-mass IMF slopes (x_1=0.5, 1.3 and 3.3) continuum subtracted as in PyStaff and compared to a SPS model with Salpeter (x_1=2.3) low-mass IMF slope. The ratio shows where most information from variations in the IMF resides within the spectrum. Grey shaded regions highlight which index bandpasses are used in SSF. Most noticeably, the NaD [λ5895] line contains much information which is not included by Martín-Navarro et al. but

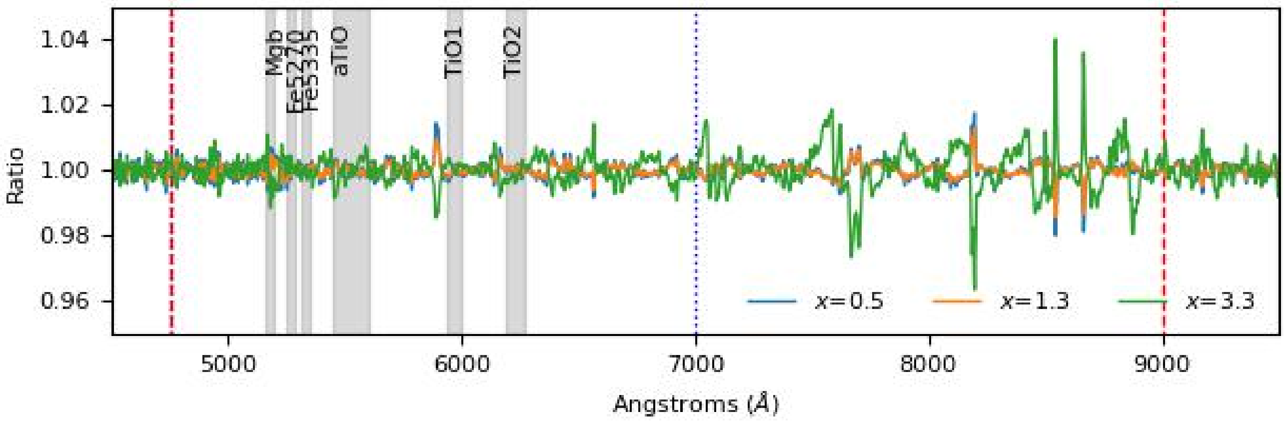

Figure 3.13: The ratio of three continuum subtracted SPS models with age 13.5Gyr, metallicity +0.2 and varying low-mass IMF slope (PyStaff $x_1 = x_2$) against a 13.5Gyr, +0.2dex SPS with Salpeter (2.3) IMF. Grey bands are wavelength regions used in SSF. The beginning and end of the short (4700-7000Å) and red-inclusive (4700-9000Å) wavelength ranges used in PyStaff are marked by blue dotted and red dashed vertical lines respectively.

which is included even in the PyStaff shortened wavelength fit. Beyond 7000Å are a host of lines which, once the uncertainties caused by telluric absorption and sky emission have been taken into account in more detail, are of great value in the red-inclusive PyStaff fit.

Although some recent studies find no evidence of IMF radial variations within galaxies, attributing small trends in changes in the spectra to abundance variations (e.g. Spiniello et al. 2015c, McConnell et al. 2016, Alton et al. 2017, Zieleniewski et al. 2017), others have begun to discover radial variations. Using IMF sensitive absorption features to map radial changes in ETGs, Martín-Navarro et al. (2014) and La Barbera et al. (2016a) both found trends with a more bottom-heavy IMF in the central regions of galaxies transitioning towards a Milky Way-like IMF at larger radii. Martín-Navarro et al. (2014) found that gradients in the IMF were more prominent in two high velocity dispersion galaxies, with the remaining low velocity dispersion galaxy showing no significant gradient. Using a full-spectrum fitting approach similar to PyStaff, van Dokkum et al. (2017) also found a bottom-heavy IMF in the central regions of 6 massive ETGs, with a more more bottom-light IMF at larger radii. Results for the IMF from gravitational lensing likewise constrain a heavier IMF in the centre of ETGs (e.g. Auger et al. 2010, Leier et al. 2016, Collett et al. 2018). While these studies seem to support the central bottom-heavy IMF with shallow gradient found in FCC167 by SSF, it should be noted that these studies were generally on high-mass ETGs. FCC167 is a lower-mass lenticular galaxy comparable in velocity dispersion to the third galaxy analysed in Martín-Navarro et al. (2014), where no significant gradient was found. The current picture explaining the difference in IMF between the bulge and disk in massive ETGs relies on different formation processes for these galaxy components (Martín-Navarro et al. 2014). This story may be different for lower-mass galaxies, such as FCC167.

The first published application of PyStaff (Vaughan et al. 2018) also studied a massive ETG - NGC 1399, the central galaxy of the Fornax galaxy cluster. Although they found a radial decrease in the IMF, this decrease did not occur until ~0.7 R_e. Interior to this radius, the IMF mismatch parameter exhibits evidence of a shallow positive gradient (Vaughan et al. 2018, Fig. 6), similar to the results found here for FCC167 using the same methods. Ignoring the first two lowest velocity dispersion bins from FCC167 which are outside the effective radius (see Fig. 3.5), the bins studied from the centre to just inside 1 R_e using PyStaff show a shallow increase in bottom-heaviness towards greater radii. The main difference between the two galaxies is that at or outside 1 R_e PyStaff returns opposite results. Interestingly, two of the galaxies studied by van Dokkum et al. (2017), NGC 1600 and NGC 2695, could also be consistent with a slight increase in the IMF before it ultimately drops to Milky Way-like at greater radii (see their Fig. 11). Given that the literature presents such a variety of results, it is unclear which of the two methods presented here is correct, further highlighting the importance of considering any systematic effects inherent in the methods used as well as the overall data quality.

Further work is needed to understand the variety of IMF gradients in galaxies. The comparison of different approaches to measuring these gradients, as presented here, is also an area for exploration. While studies to date have generally considered simple radial profiles, MUSE provides the opportunity to generate full 2D maps of IMF properties. Realising the full potential of integral field spectroscopy is the next step for the research presented here, and it is hoped that this will shed light on the true nature of spatial variations of the IMF in galaxies in the near future.

'Would you tell me, please, which way I ought to go from here?'
'That depends a good deal on where you want to get to,' said the Cat.

Lewis Carroll, Alice in Wonderland

4 Conclusion

This thesis has contemplated the history of the IMF and the gradual move of the field through many technological advances to its current state today. Using the spectrum of a galaxy to find the ratio of dwarfs to giants has been a suggested method for decades (Spinrad 1962), however it is only relatively recently that this has become a reliable method, with improvements in both observations and stellar population models. The exquisite spatial and spectral resolution of the data that instruments such as MUSE provide now allows for study of the IMF not just between galaxies, but spatially within galaxies.

We have presented kinematic and index strength spatial maps for a sample of galaxies from the Fornax cluster using new Fornax3D Survey data from MUSE. Concentrating on the lenticular galaxy FCC167, two methods for finding the IMF have been compared. A recent method using full-spectrum fitting and variation simultaneously of multiple element abundances (PyStaff, Vaughan et al. 2018) has been tested. PyStaff was found to reproduce known input model parameters (Conroy et al. 2018) and recover similar results for reference data as published studies (Conroy et al. 2013, La Barbera et al. 2013). It was further tested against a second method currently under development by Martín-Navarro et al. which concentrates on limiting the degrees of freedom in the model fit through stepwise constraints on age, metallicity and abundance, and fitting particular regions of the spectrum (Selective Spectral Fitting, SSF). The two methods were found to produce relative trends of metallicity, age and element abundances that were in agreement, although small differences in the absolute values can be seen. However, the IMF results did not agree. While Pystaff suggests an increasingly bottom-heavy IMF with increasing radius and decreasing velocity dispersion, SSF results are consistent with either a flat IMF across the galaxy or a bottom-heavy IMF in the galactic centre mildly decreasing at greater radii.

The cause of these differences may be the inclusion in the full-spectral fitting PyStaff of a greater amount of spectral information, in particular the NaD line, which is not included in SSF. Next steps towards resolving the conflict in results will include running PyStaff using the same wavelength ranges as used for SSF. This will allow investigation into whether the inclusion of more spectral information is the driving factor producing such disparate results. Another contributing factor to the disagreement between PyStaff and SSF results may be the use of separate SSP models. The different handling of isochrones, stellar libraries, metallicity and important elements such as Na and Ti between the MILES and Conroy models (Spiniello et al. 2015a) as well as their underlying IMF shape assumptions may well have an important impact on the IMF returned when fitting data. A future step is to swap best-fitting models between the two methods, comparing the results when fit to these models instead of the data. This test will probe how far the underlying model assumptions contribute to the results. Further analysis of the inclusion and modelling of Na abundances and their affect on the IMF within SSF is also needed to address the question of whether dissimilar treatment of Na could drive the differences shown in this thesis.

An application of PyStaff to entire galaxies is now possible, with the aim of producing high spatial resolution maps of the variations. Application to more galaxies both within the Fornax3D Survey sample and to other galaxies is planned. A focus on more massive galaxies will be taken initially, as these are the galaxies expected to have a noticeable IMF gradient. This work will enable direct comparison between IMF and stellar population properties, facilitating our understanding of the galaxy characteristics driving variations in the IMF.

A

Appendix

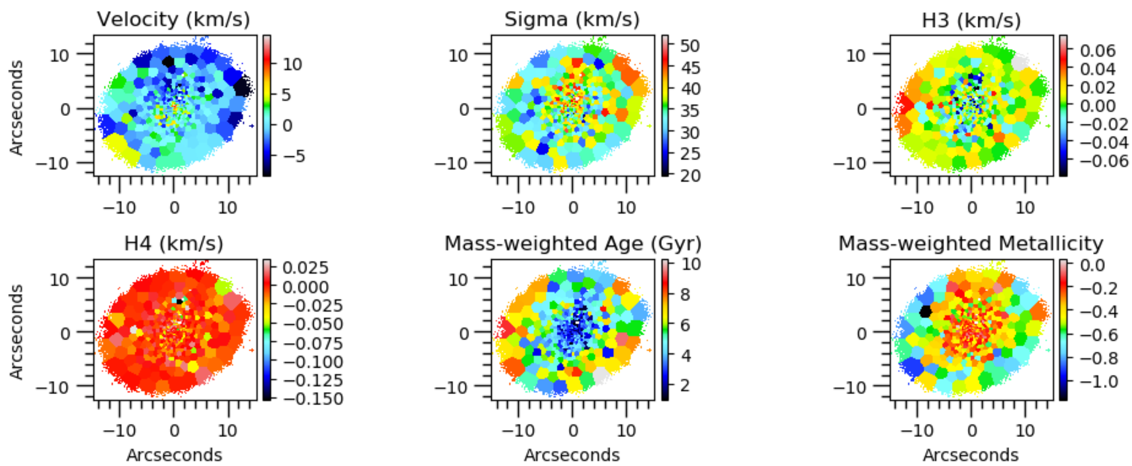

Figure A.1: FCC090 - velocity, velocity dispersion, 3rd and 4th kinematic moments as well as the non-regularised age and metallicity found from pPXF (Chapter 2.2.2)

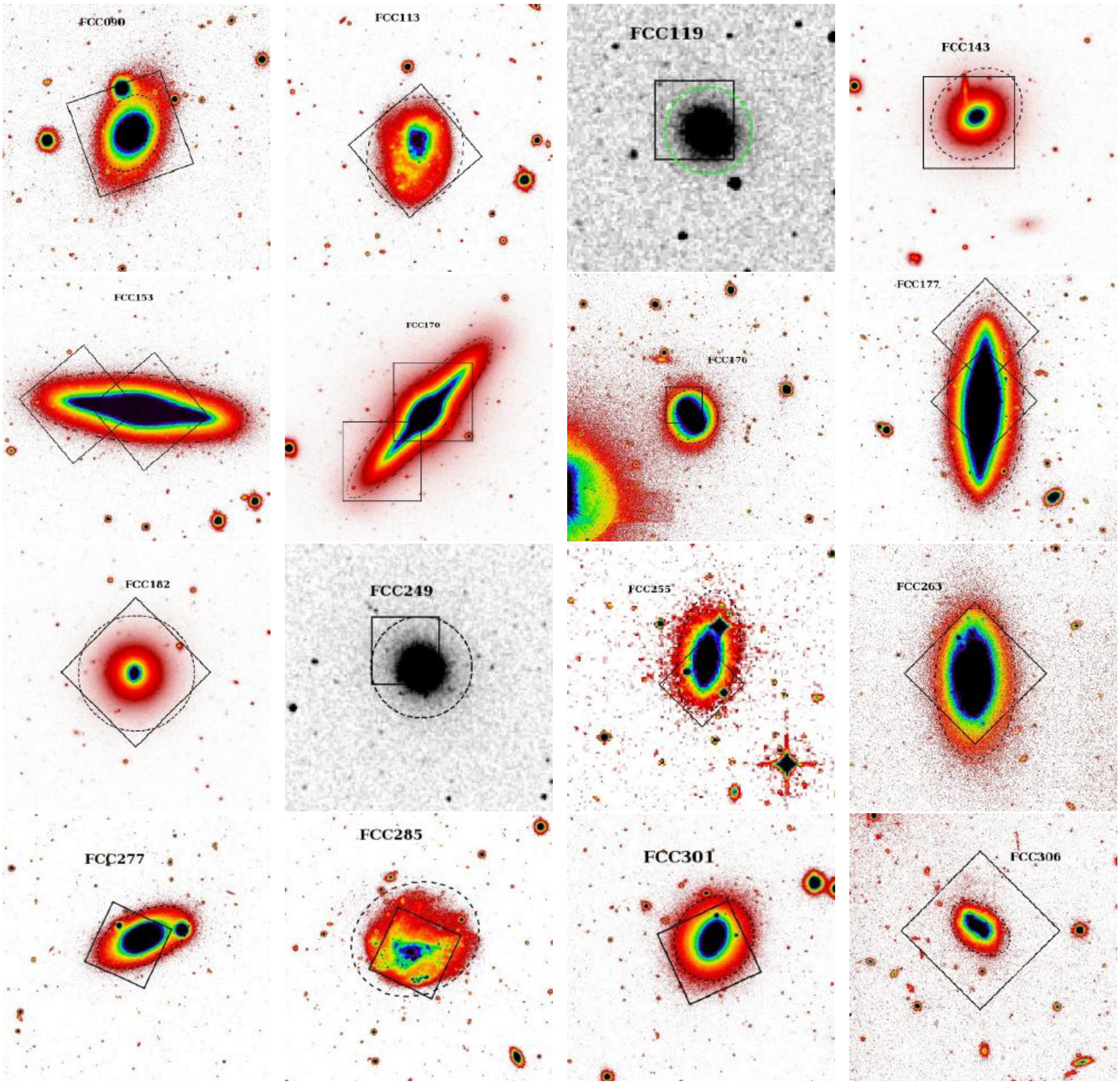

Figure A.2: Thumbnails showing the pointings for each galaxy taken in the F3D survey (except for FCC167, see Chapter 2). From the left: *Top row* - FCC090, FCC113, FCC119 and FCC143; *2nd row* - FCC153, FCC170, FCC176 and FCC177; *3rd row* - FCC182, FCC249, FCC255 and FCC263; and *4th row* - FCC277, FCC285, FCC301 and FCC306.

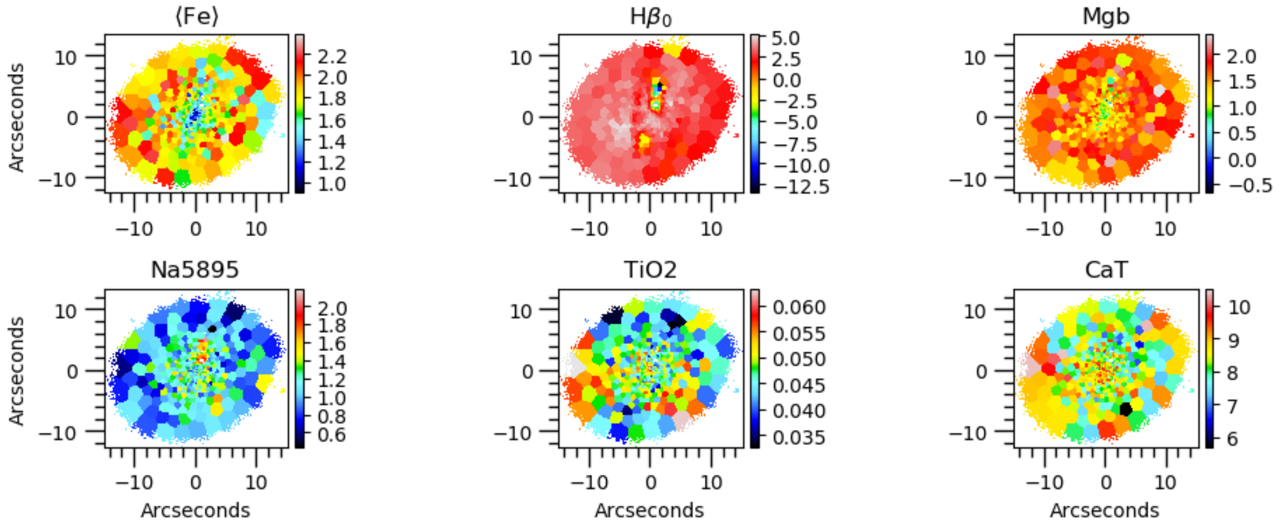

Figure A.3: FCC090 - maps of ⟨Fe⟩ *(top left)*, Hβ_0 *(top middle)*, Mgb *(top right)*, NaD [5895] *(bottom left)*, TiO2 *(bottom middle)*, and CaT *(bottom right)* (Chapter 2.2.3)

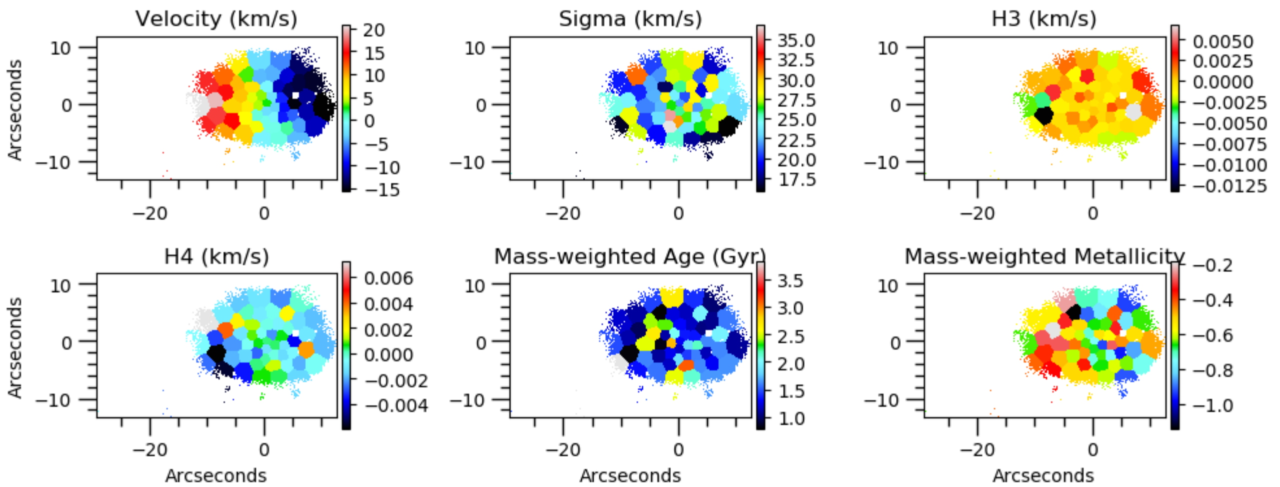

Figure A.4: FCC113 - velocity, velocity dispersion, 3rd and 4th kinematic moments as well as the non-regularised age and metallicity found from pPXF (Chapter 2.2.2)

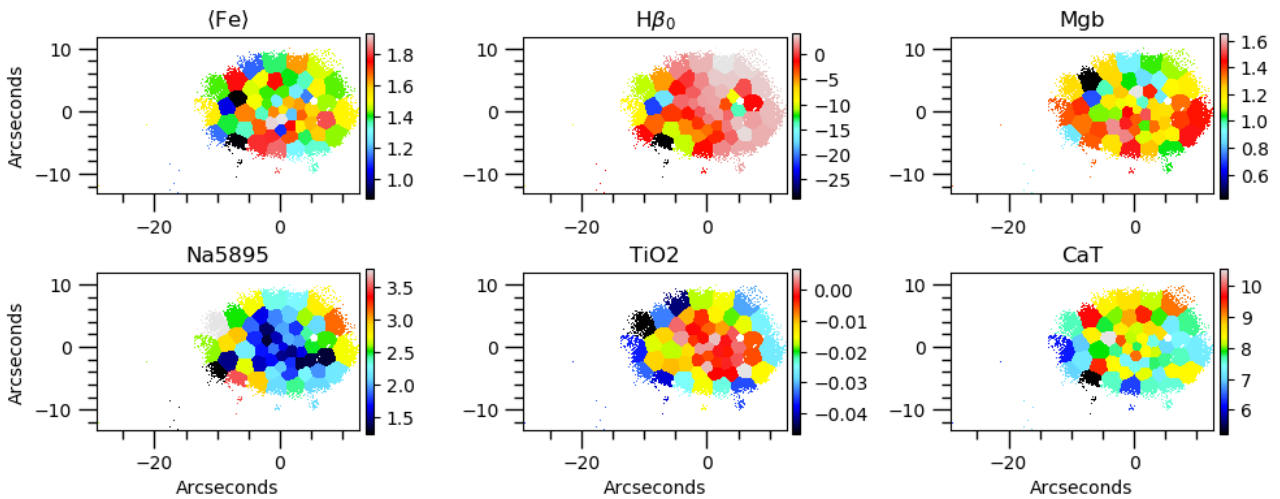

Figure A.5: FCC113 - maps of ⟨Fe⟩ *(top left)*, Hβ_0 *(top middle)*, Mgb *(top right)*, NaD [5895] *(bottom left)*, TiO2 *(bottom middle)*, and CaT *(bottom right)* (Chapter 2.2.3)

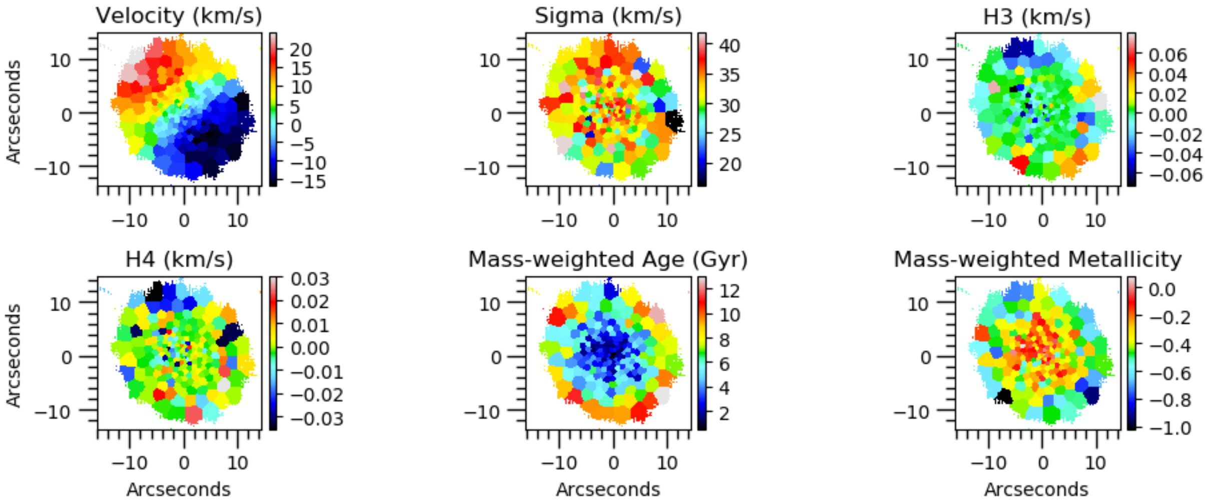

Figure A.6: FCC119 - velocity, velocity dispersion, 3rd and 4th kinematic moments as well as the non-regularised age and metallicity found from pPXF (Chapter 2.2.2)

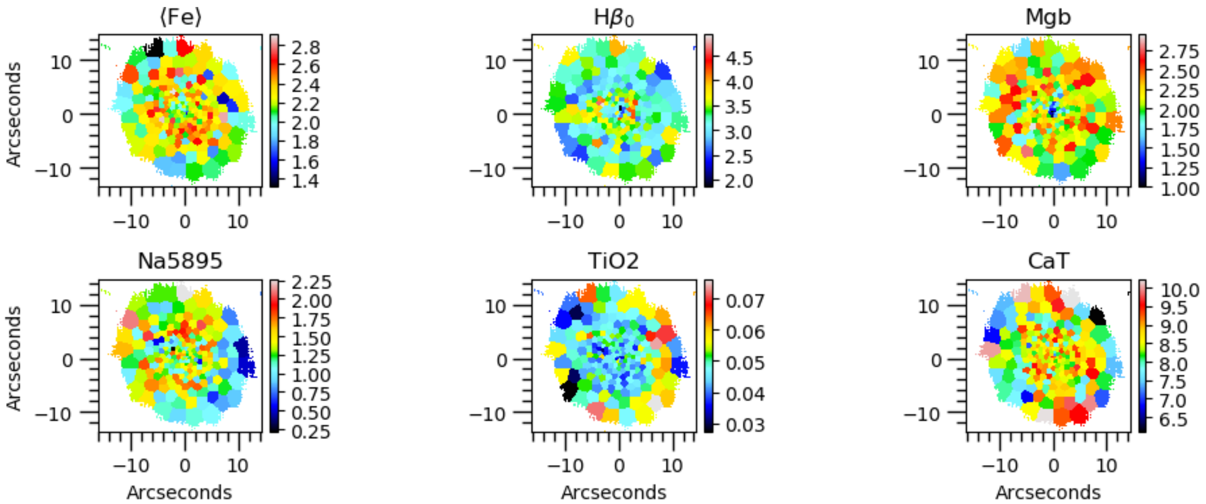

Figure A.7: FCC119 - maps of ⟨Fe⟩ *(top left)*, Hβ_0 *(top middle)*, Mgb *(top right)*, NaD [5895] *(bottom left)*, TiO2 *(bottom middle)*, and CaT *(bottom right)* (Chapter 2.2.3)

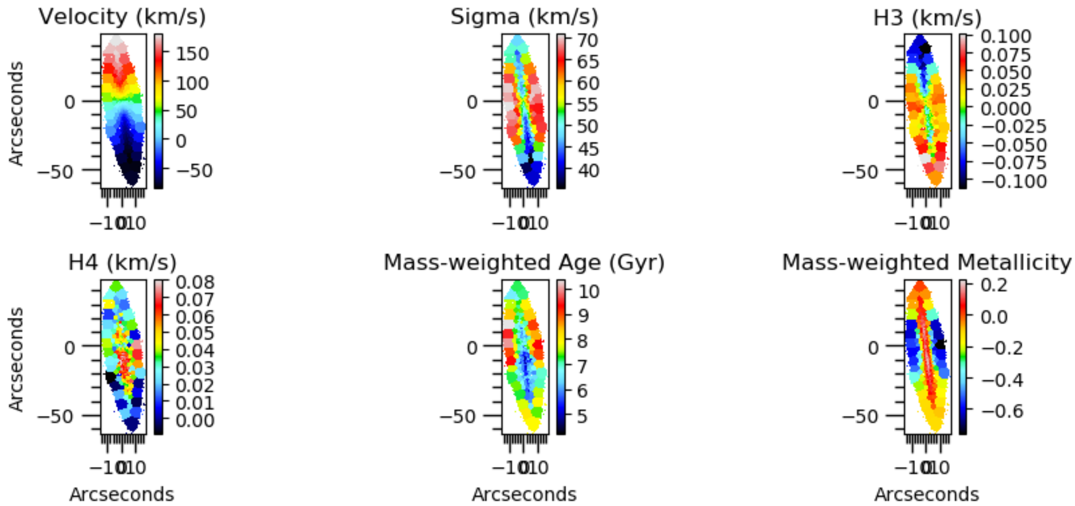

Figure A.8: FCC153 - velocity, velocity dispersion, 3rd and 4th kinematic moments as well as the non-regularised age and metallicity found from pPXF (Chapter 2.2.2)

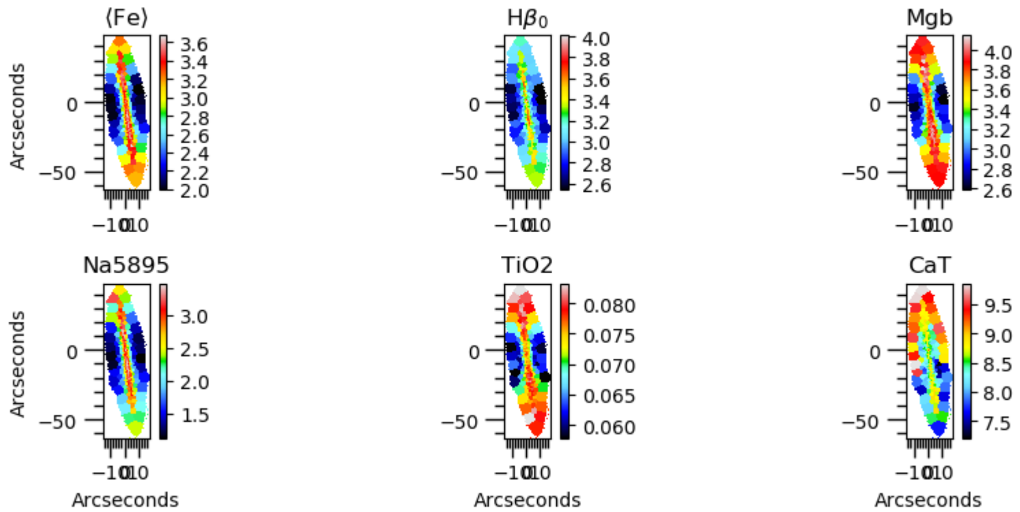

Figure A.9: FCC153 - maps of ⟨Fe⟩ *(top left)*, Hβ_0 *(top middle)*, Mgb *(top right)*, NaD [5895] *(bottom left)*, TiO2 *(bottom middle)*, and CaT *(bottom right)* (Chapter 2.2.3)

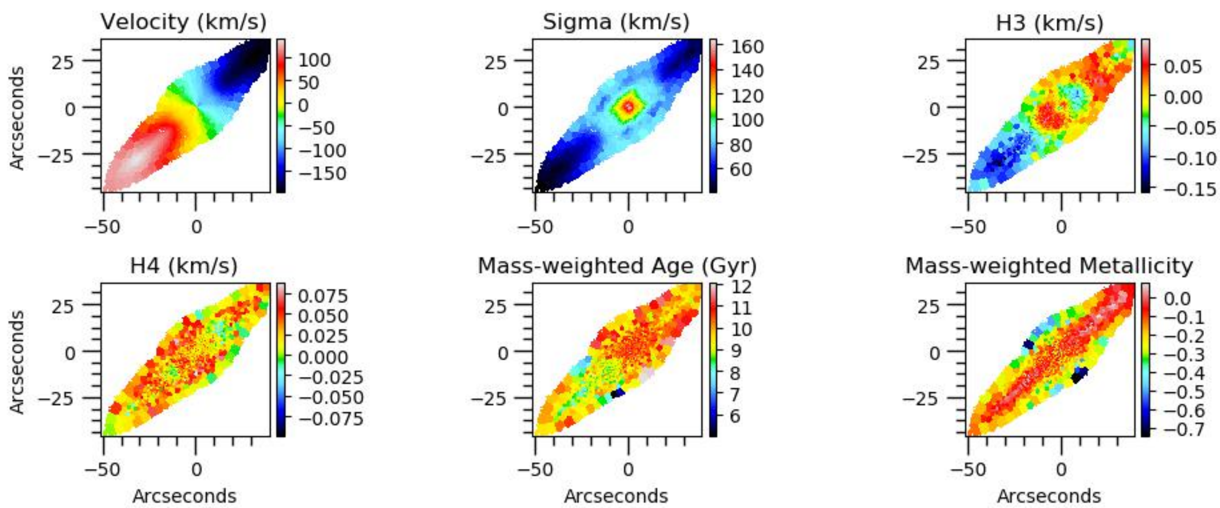

Figure A.10: FCC170 - velocity, velocity dispersion, 3rd and 4th kinematic moments as well as the non-regularised age and metallicity found from pPXF (Chapter 2.2.2)

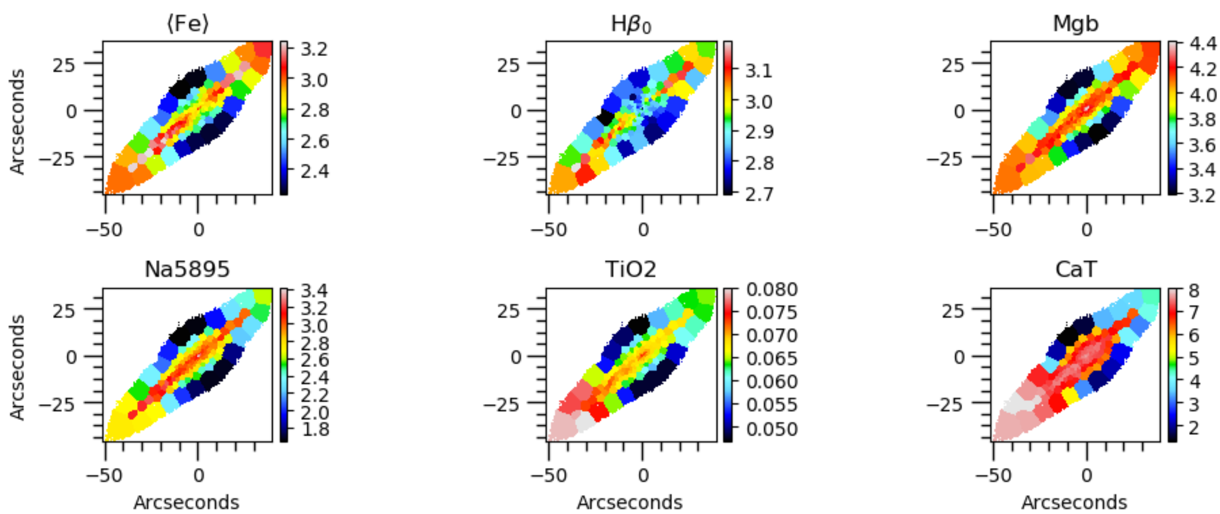

Figure A.11: FCC170 - maps of ⟨Fe⟩ *(top left)*, Hβ_0 *(top middle)*, Mgb *(top right)*, NaD [5895] *(bottom left)*, TiO2 *(bottom middle)*, and CaT *(bottom right)* (Chapter 2.2.3)

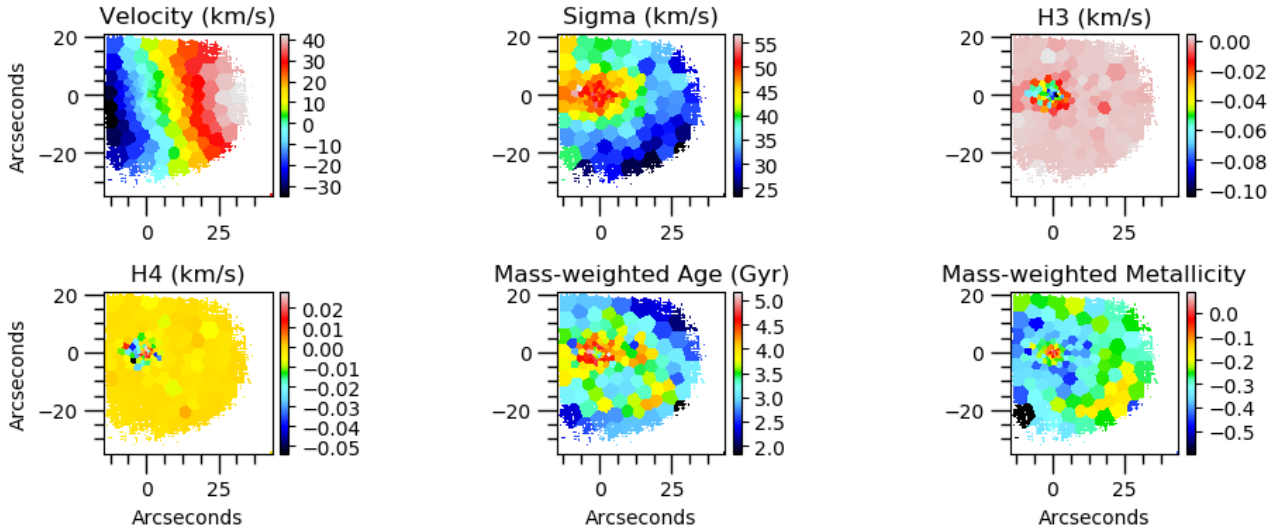

Figure A.12: FCC176 - velocity, velocity dispersion, 3rd and 4th kinematic moments as well as the non-regularised age and metallicity found from pPXF (Chapter 2.2.2)

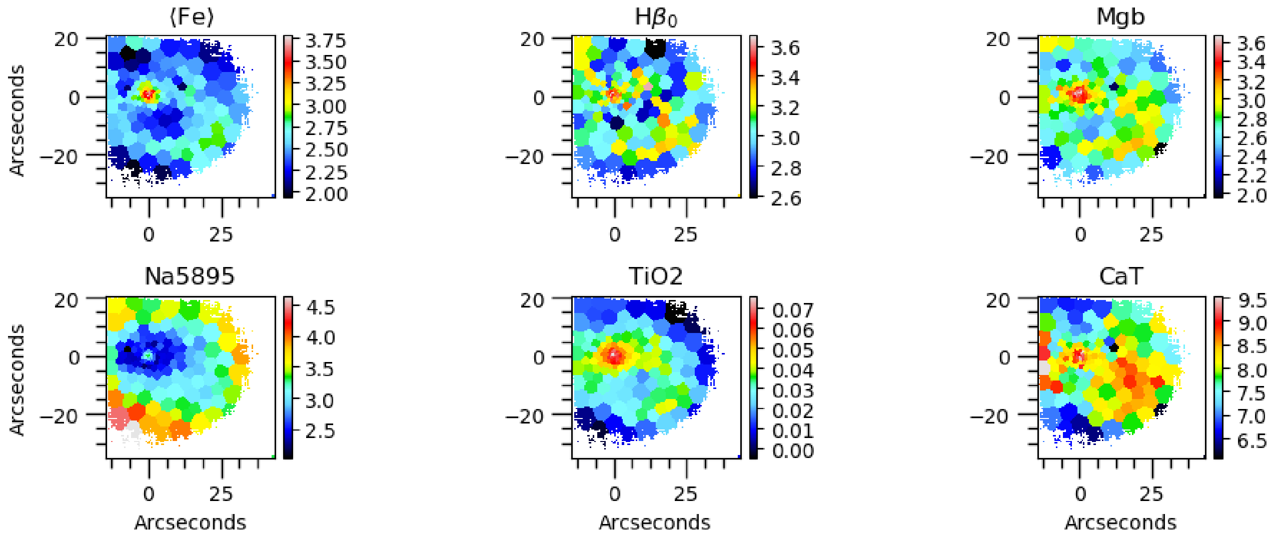

Figure A.13: FCC176 - maps of ⟨Fe⟩ *(top left)*, Hβ_0 *(top middle)*, Mgb *(top right)*, NaD [5895] *(bottom left)*, TiO2 *(bottom middle)*, and CaT *(bottom right)* (Chapter 2.2.3)

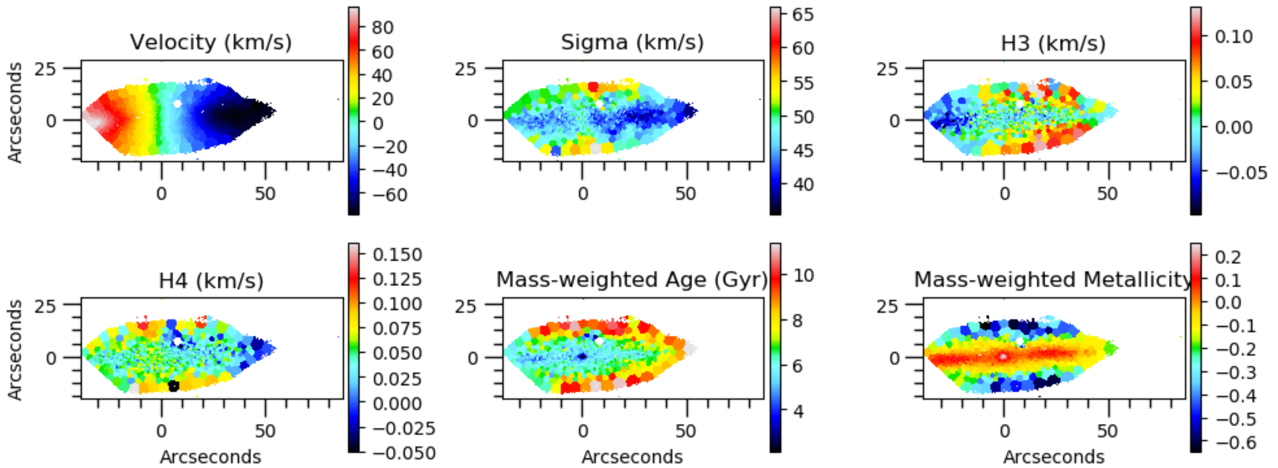

Figure A.14: FCC177 - velocity, velocity dispersion, 3rd and 4th kinematic moments as well as the non-regularised age and metallicity found from pPXF (Chapter 2.2.2)

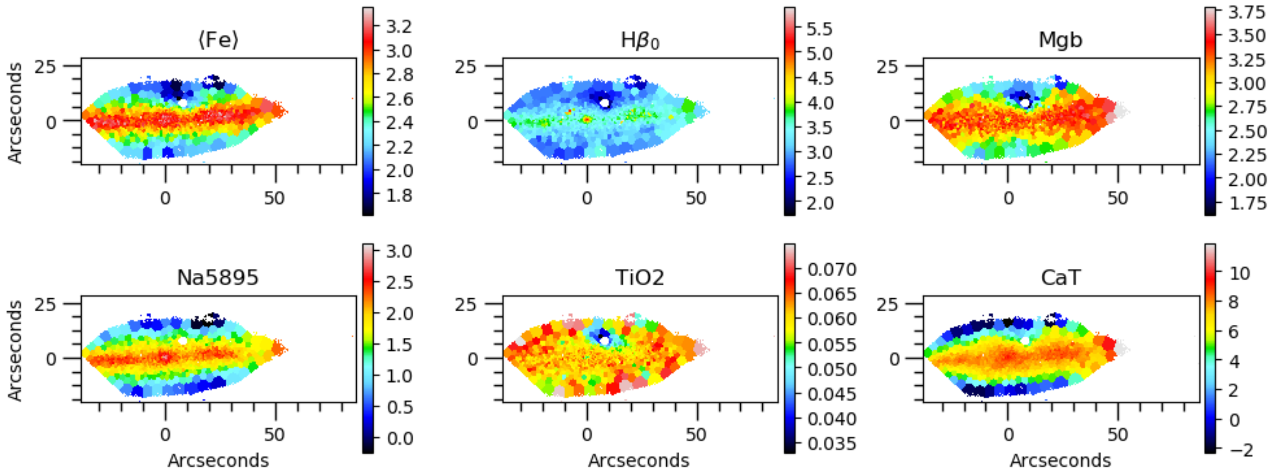

Figure A.15: FCC177 - maps of ⟨Fe⟩ *(top left)*, Hβ_0 *(top middle)*, Mgb *(top right)*, NaD [5895] *(bottom left)*, TiO2 *(bottom middle)*, and CaT *(bottom right)* (Chapter 2.2.3)

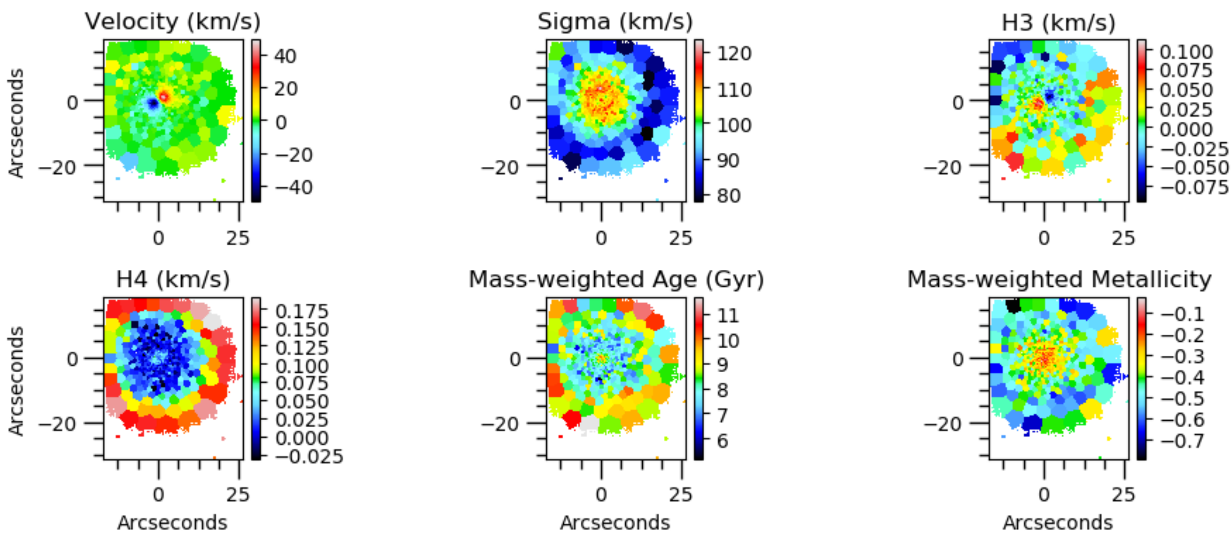

Figure A.16: FCC249 - velocity, velocity dispersion, 3rd and 4th kinematic moments as well as the non-regularised age and metallicity found from pPXF (Chapter 2.2.2)

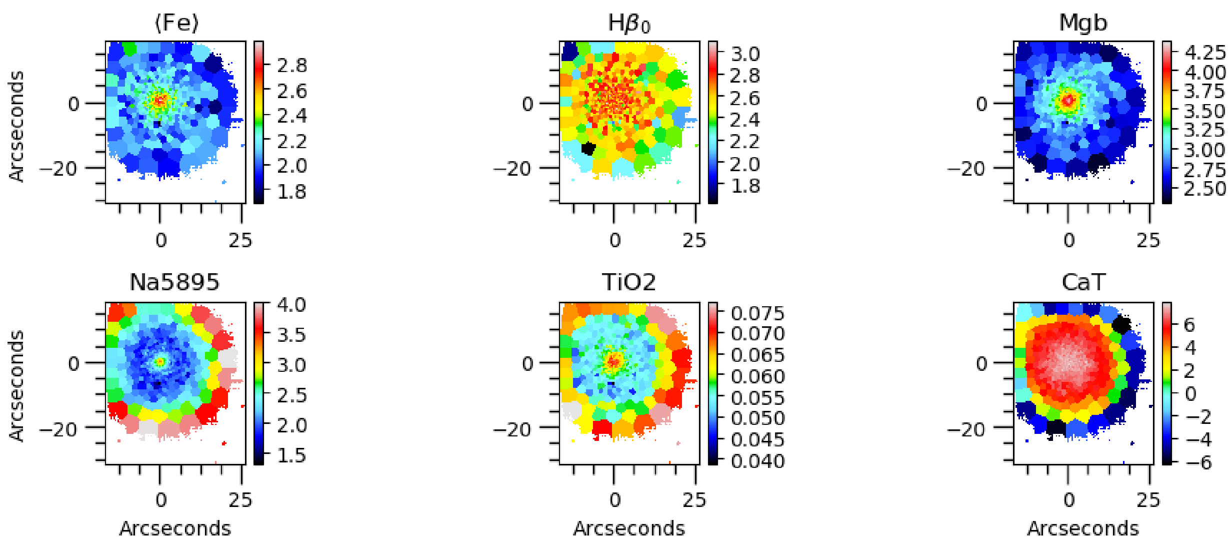

Figure A.17: FCC249 - maps of ⟨Fe⟩ *(top left)*, Hβ_0 *(top middle)*, Mgb *(top right)*, NaD [5895] *(bottom left)*, TiO2 *(bottom middle)*, and CaT *(bottom right)* (Chapter 2.2.3)

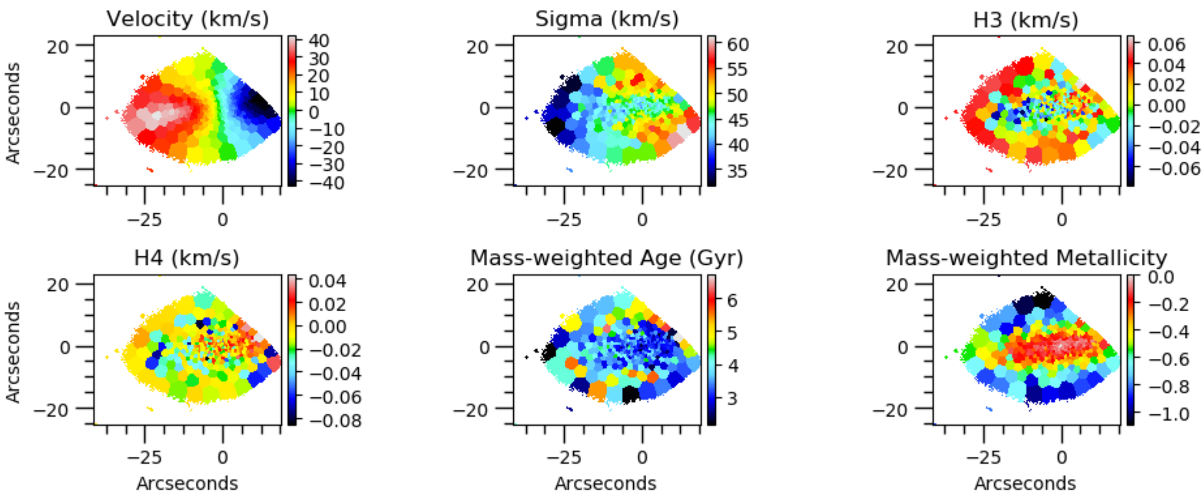

Figure A.18: FCC255 - velocity, velocity dispersion, 3rd and 4th kinematic moments as well as the non-regularised age and metallicity found from pPXF (Chapter 2.2.2)

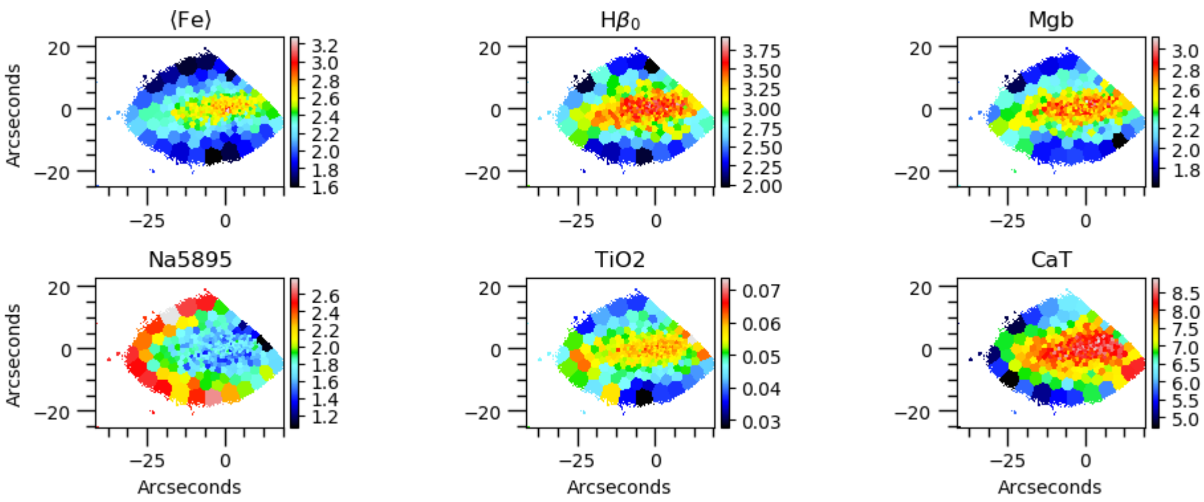

Figure A.19: FCC255 - maps of ⟨Fe⟩ *(top left)*, Hβ_0 *(top middle)*, Mgb *(top right)*, NaD [5895] *(bottom left)*, TiO2 *(bottom middle)*, and CaT *(bottom right)* (Chapter 2.2.3)

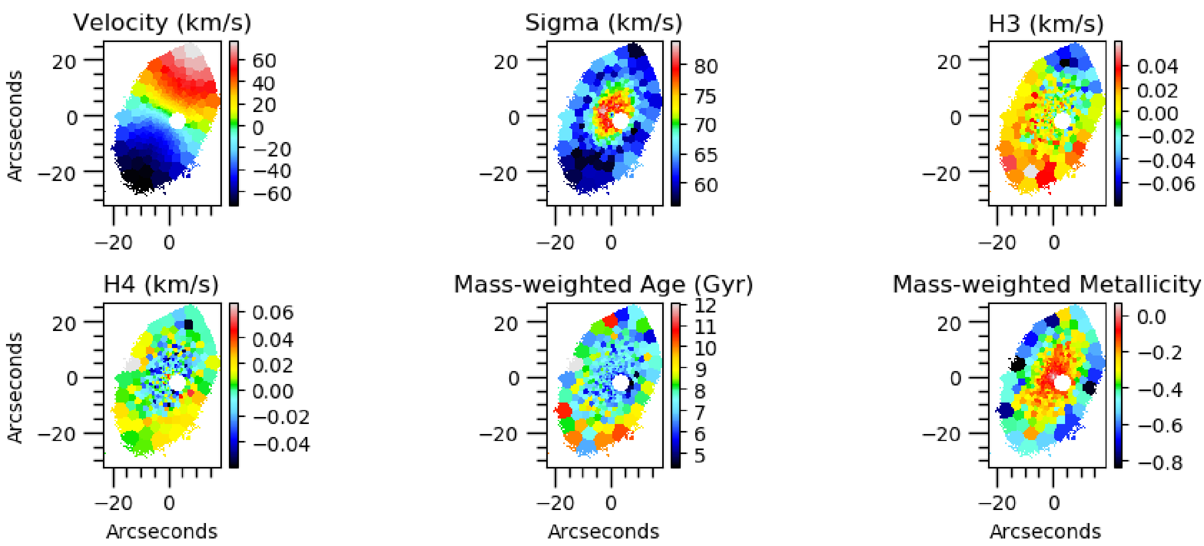

Figure A.20: FCC277 - velocity, velocity dispersion, 3rd and 4th kinematic moments as well as the non-regularised age and metallicity found from pPXF (Chapter 2.2.2)

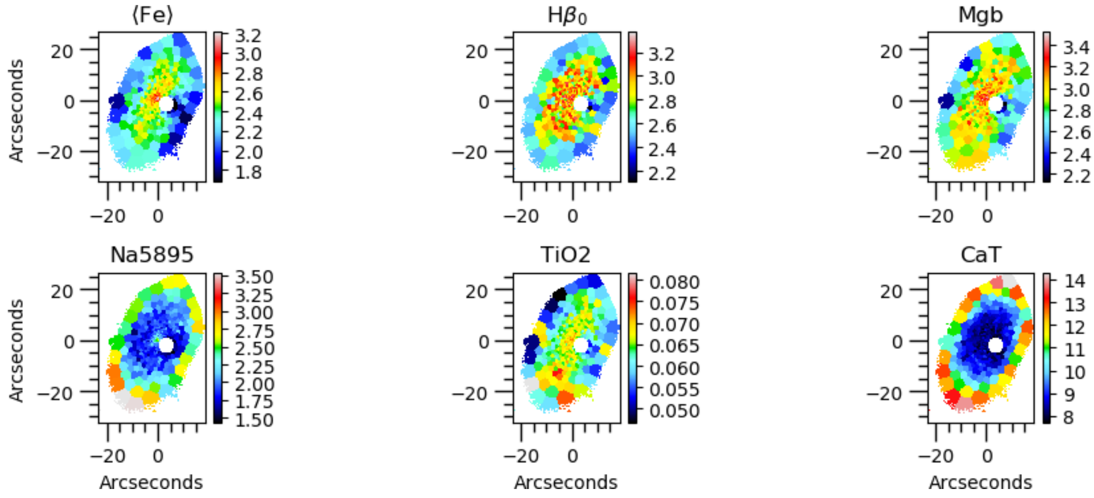

Figure A.21: FCC277 - maps of ⟨Fe⟩ *(top left)*, Hβ_0 *(top middle)*, Mgb *(top right)*, NaD [5895] *(bottom left)*, TiO2 *(bottom middle)*, and CaT *(bottom right)* (Chapter 2.2.3)

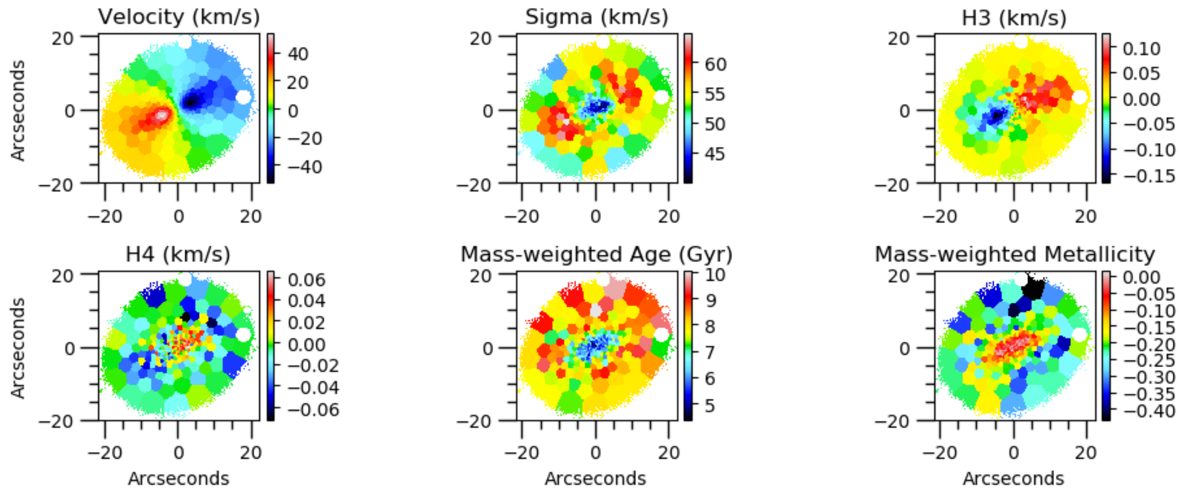

Figure A.22: FCC301 - velocity, velocity dispersion, 3rd and 4th kinematic moments as well as the non-regularised age and metallicity found from pPXF (Chapter 2.2.2)

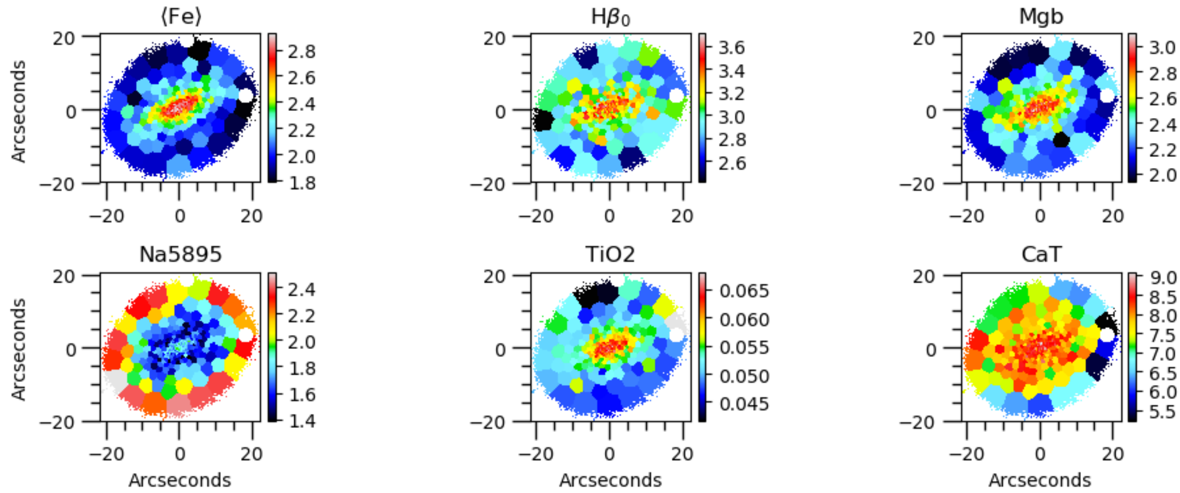

Figure A.23: FCC301 - maps of ⟨Fe⟩ *(top left)*, Hβ_0 *(top middle)*, Mgb *(top right)*, NaD [5895] *(bottom left)*, TiO2 *(bottom middle)*, and CaT *(bottom right)* (Chapter 2.2.3)

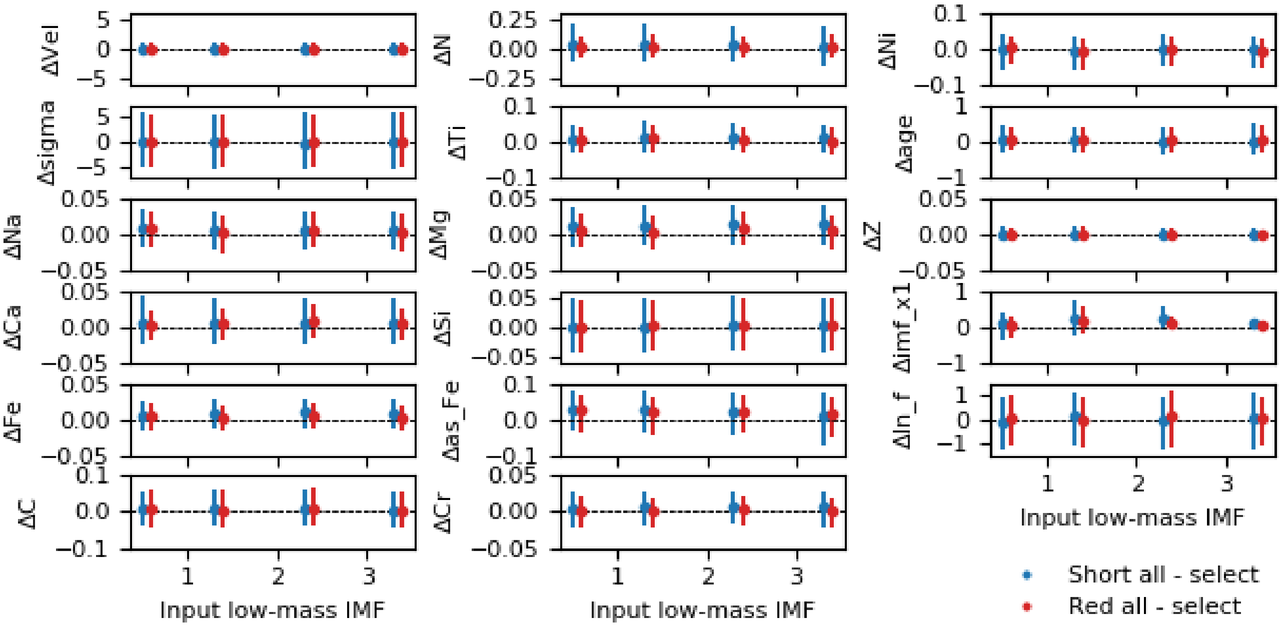

Figure A.24: Selected free PyStaff variables plotted as the difference between the value found when all variables were left free and when selected variables were left free against the known model low-mass IMF for the Conroy models, offset horizontally for clarity for both shortened (blue points) and red-inclusive (red points) wavelength ranges (see Chapter 3.1.4).

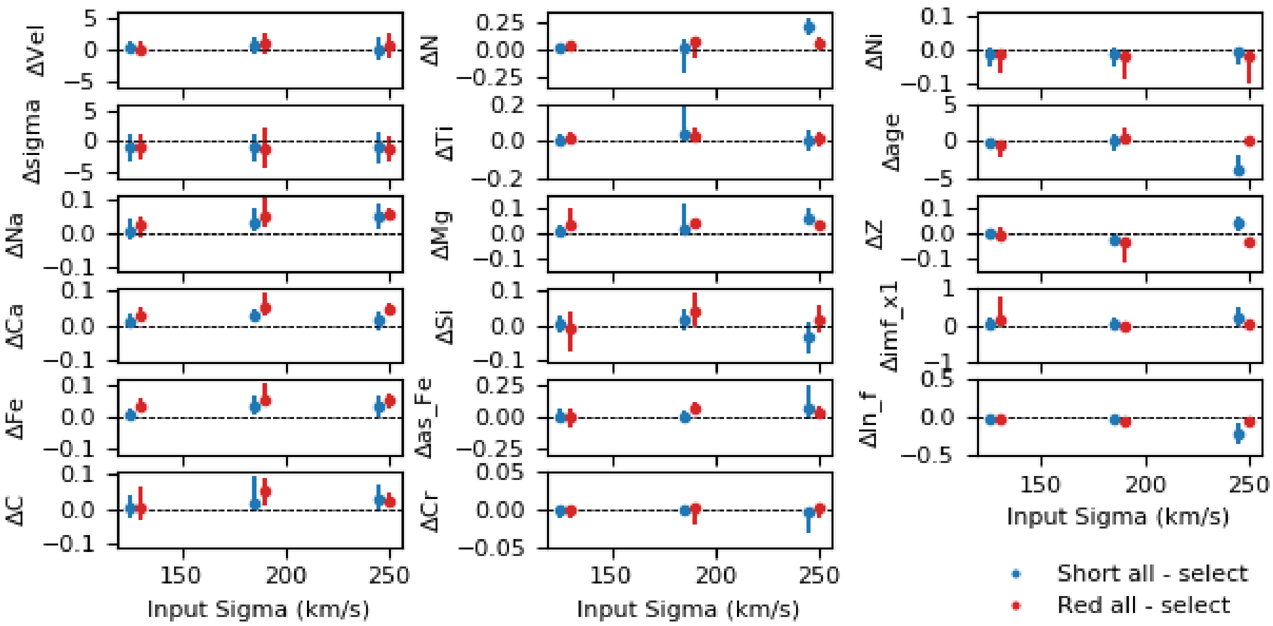

Figure A.25: Selected free PyStaff variables plotted as the difference between the value found when all variables were left free and when selected variables were left free against the known velocity dispersion for the SDSS spectra, offset horizontally for clarity for both shortened (blue points) and red-inclusive (red points) wavelength ranges (see Chapter 3.1.4).

References

Abazajian, K. N., Adelman-McCarthy, J. K., Agüeros, M. A., Allam, S. S., Prieto, C. A., An, D., Anderson, K. S., Anderson, S. F., Annis, J., Bahcall, N. A. et al. (2009), 'The seventh data release of the sloan digital sky survey', *The Astrophysical Journal Supplement Series* **182**(2), 543.

Adelman-McCarthy, J. K., Agüeros, M. A., Allam, S. S., Prieto, C. A., Anderson, K. S., Anderson, S. F., Annis, J., Bahcall, N. A., Bailer-Jones, C., Baldry, I. K. et al. (2008), 'The sixth data release of the Sloan Digital Sky Survey', *The Astrophysical Journal Supplement Series* **175**(2), 297.

Alton, P. D., Smith, R. J. & Lucey, J. R. (2017), 'Kinetys: constraining spatial variations of the stellar initial mass function in early-type galaxies', *Monthly Notices of the Royal Astronomical Society* **468**(2), 1594–1615.

Audouze, J. & Tinsley, B. M. (1976), 'Chemical evolution of galaxies', *Annual Review of Astronomy and Astrophysics* **14**(1), 43–79.

Auger, M., Treu, T., Gavazzi, R., Bolton, A., Koopmans, L. & Marshall, P. (2010), 'Dark matter contraction and the stellar content of massive early-type galaxies: Disfavoring âĂIJlightâĂİ initial mass functions', *The Astrophysical Journal Letters* **721**(2), L163.

Bacon, R., Accardo, M., Adjali, L., Anwand, H., Bauer, S., Biswas, I., Blaizot, J., Boudon, D., Brau-Nogue, S., Brinchmann, J. et al. (2010), The MUSE second-generation VLT instrument, *in* 'Ground-based and Airborne Instrumentation for Astronomy III', Vol. 7735, International Society for Optics and Photonics, p. 773508.

Baldry, I. K. & Glazebrook, K. (2003), 'Constraints on a universal stellar initial mass function from ultraviolet to near-infrared galaxy luminosity densities', *The Astrophysical Journal* **593**(1), 258.

Bastian, N., Covey, K. R. & Meyer, M. R. (2010), 'A Universal Stellar Initial Mass Function? A Critical Look at Variations', *Annual Review of Astronomy and Astrophysics* **48**(1), 339–389.

Becker, S., Iben Jr, I. & Tuggle, R. (1977), 'On the frequency-period distribution of Cepheid variables in galaxies in the Local Group', *The Astrophysical Journal* **218**, 633–653.

Burki, G. (1977), 'Observational tests on star formation. III-Variation of the upper mass spectrum with the size of very young clusters', *Astronomy and Astrophysics* **57**, 135–140.

Cappellari, M. (2009), 'Voronoi binning: Optimal adaptive tessellations of multi-dimensional data', *arXiv preprint arXiv:0912.1303* .
URL: *https://arxiv.org/pdf/0912.1303.pdf*

Cappellari, M. (2017), 'Improving the full spectrum fitting method: accurate convolution with Gauss-Hermite functions', *Monthly Notices of the Royal Astronomical Society* **466**(1), 798–811.

Cappellari, M. & Copin, Y. (2003), 'Adaptive spatial binning of integral-field spectroscopic data using Voronoi tessellations', *Monthly Notices of the Royal Astronomical Society* **342**(2), 345–354.

Cappellari, M. & Emsellem, E. (2004), 'Parametric recovery of line-of-sight velocity distributions from absorption-line spectra of galaxies via penalized likelihood', *Publications of the Astronomical Society of the Pacific* **116**(816), 138.

Cappellari, M., Emsellem, E., Krajnović, D., McDermid, R. M., Scott, N., Verdoes Kleijn, G., Young, L. M., Alatalo, K., Bacon, R., Blitz, L. et al. (2011), 'The atlas3d project–i. a volume-limited sample of 260 nearby early-type galaxies: science goals and selection criteria', *Monthly Notices of the Royal Astronomical Society* **413**(2), 813–836.

Cappellari, M., McDermid, R. M., Alatalo, K., Blitz, L., Bois, M., Bournaud, F., Bureau, M., Crocker, A. F., Davies, R. L. & Davis, T. A. (2012), 'Systematic variation of the stellar initial mass function in early-type galaxies', *Nature* **484**(7395), 485–488.

Cappellari, M., McDermid, R. M., Alatalo, K., Blitz, L., Bois, M., Bournaud, F., Bureau, M., Crocker, A. F., Davies, R. L., Davis, T. A. et al. (2013), 'The ATLAS3D project–XX. Mass–size and mass–σ distributions of early-type galaxies: bulge fraction drives kinematics, mass-to-light ratio, molecular gas fraction and stellar initial mass function', *Monthly Notices of the Royal Astronomical Society* **432**(3), 1862–1893.

Carter, D., Visvanathan, N. & Pickles, A. (1986), 'The dwarf star content of elliptical and lenticular galaxies', *The Astrophysical Journal* **311**, 637–650.

Cenarro, A., Cardiel, N., Gorgas, J., Peletier, R., Vazdekis, A. & Prada, F. (2001), 'Empirical calibration of the near−infrared Ca II triplet−I. The stellar library and index definition', *Monthly Notices of the Royal Astronomical Society* **326**(3), 959–980.

Cenarro, A., Gorgas, J., Vazdekis, A., Cardiel, N. & Peletier, R. (2003), 'Near-infrared line-strengths in elliptical galaxies: evidence for initial mass function variations?', *Monthly Notices of the Royal Astronomical Society* **339**(1), L12–L16.

Chabrier, G. (2003), 'Galactic stellar and substellar initial mass function', *Publications of the Astronomical Society of the Pacific* **115**(809), 763.

Choi, J., Conroy, C., Moustakas, J., Graves, G. J., Holden, B. P., Brodwin, M., Brown, M. J. & Van Dokkum, P. G. (2014), 'The assembly histories of quiescent galaxies since z= 0.7 from absorption line spectroscopy', *The Astrophysical Journal* **792**(2), 95.

Choi, J., Dotter, A., Conroy, C., Cantiello, M., Paxton, B. & Johnson, B. D. (2016), 'Mesa isochrones and stellar tracks (MIST). I. Solar-scaled models', *The Astrophysical Journal* **823**(2), 102.

Cohen, J. (1978), 'Near-infrared luminosity-sensitive features in m dwarfs and giants, and in m31 and m32', *The Astrophysical Journal* **221**, 788–796.

Collett, T. E., Oldham, L. J., Smith, R. J., Auger, M. W., Westfall, K. B., Bacon, D., Nichol, R. C., Masters, K. L., Koyama, K. & van den Bosch, R. (2018), 'A precise extragalactic test of general relativity', *Science* **360**(6395), 1342–1346.

Conroy, C., Graves, G. J. & van Dokkum, P. G. (2013), 'Early-Type Galaxy Archeology: Ages, Abundance Ratios, and Effective Temperatures from Full-Spectrum Fitting', *The Astrophysical Journal* **780**(1), 33.

Conroy, C. & van Dokkum, P. (2012a), 'Counting Low-Mass Stars in Integrated Light', *The Astrophysical Journal* **747**(1), 69.

Conroy, C. & van Dokkum, P. G. (2012b), 'The Stellar Initial Mass Function in Early-Type Galaxies from Absorption Line Spectroscopy. II. Results', *The Astrophysical Journal* **760**(1), 71.

Conroy, C., van Dokkum, P. & Villaume, A. (2017), 'The stellar initial mass function in early-type galaxies from absorption line spectroscopy. IV. A super-Salpeter IMF in the center of NGC 1407 from non-parametric models', *The Astrophysical Journal* .

Conroy, C., Villaume, A., van Dokkum, P. & Lind, K. (2018), 'Metal-rich, Metal-poor: Updated Stellar Population Models for Old Stellar Systems', *arXiv preprint arXiv:1801.10185* .
URL: *https://arxiv.org/pdf/1801.10185.pdf*

Davis, T. A. & McDermid, R. M. (2016), 'Spatially resolved variations of the IMF mass normalization in early-type galaxies as probed by molecular gas kinematics', *Monthly Notices of the Royal Astronomical Society* **464**(1), 453–468.

Delisle, S. & Hardy, E. (1992), 'Near-infrared spectral gradients in ellipticals and bulges, and the nature of the na feature near 8200 a', *The Astronomical Journal* **103**, 711–727.

Dennefeld, M. & Tammann, G. (1980), 'Birthrate and mass function in the Magellanic Clouds', *Astronomy and Astrophysics* **83**, 275–286.

Dotter, A. (2016), 'MESA Isochrones and Stellar Tracks (MIST) 0: Methods for the Construction of Stellar Isochrones', *The Astrophysical Journal Supplement Series* **222**(1), 8.

Faber, S. & French, H. (1980), 'Possible M dwarf enrichment in the semistellar nucleus of M31', *The Astrophysical Journal* **235**, 405–412.

Falcón-Barroso, J., Sánchez-Blázquez, P., Vazdekis, A., Ricciardelli, E., Cardiel, N., Cenarro, A., Gorgas, J. & Peletier, R. (2011), 'An updated MILES stellar library and stellar population models', *Astronomy & Astrophysics* **532**, A95.

Ferguson, H. C. (1989), 'Galaxy populations in the Fornax and Virgo clusters', *Astrophysics and Space Science* **157**(1-2), 227–233.

Ferreras, I., Barbera, F. L., Rosa, I. G. d. l., Vazdekis, A., Carvalho, R. R. d., Falcón-Barroso, J. & Ricciardelli, E. (2012), 'Systematic variation of the stellar initial mass function with velocity dispersion in early-type galaxies', *Monthly Notices of the Royal Astronomical Society: Letters* **429**(1), L15–L19.

Foreman-Mackey, D., Hogg, D. W., Lang, D. & Goodman, J. (2013), 'emcee: The MCMC Hammer', *Publications of the Astronomical Society of the Pacific* **125**.

Freudling, W., Romaniello, M., Bramich, D., Ballester, P., Forchi, V., García-Dabló, C., Moehler, S. & Neeser, M. (2013), 'Automated data reduction workflows for astronomy-The ESO Reflex environment', *Astronomy & Astrophysics* **559**, A96.

Gerhard, O. E. (1993), 'Line-of-sight velocity profiles in spherical galaxies: breaking the degeneracy between anisotropy and mass', *Monthly Notices of the Royal Astronomical Society* **265**(1), 213–230.

Girardi, L., Bressan, A., Bertelli, G. & Chiosi, C. (2000), 'Evolutionary tracks and isochrones for low- and intermediate-mass stars: From 0.15 to $7M_{\odot}$, and from $z = 0.0004$ to 0.03', *Astronomy and Astrophysics Supplement Series* **141**(3), 371–383.

Grillmair, C. J., Mould, J. R., Holtzman, J. A., Worthey, G., Ballester, G. E., Burrows, C. J., Clarke, J. T., Crisp, D., Evans, R. W., Gallagher III, J. S. et al. (1998), 'Hubble Space Telescope observations of the Draco dwarf spheroidal galaxy', *The Astronomical Journal* **115**(1), 144.

Hardy, E. & Couture, J. (1988), 'Detection and measurement of the wing-ford band in the near-infrared spectra of elliptical galaxies', *The Astrophysical Journal* **325**, L29–L31.

Hunter, D. A., Baum, W. A., O'Neil Jr, E. J. & Lynds, R. (1996a), 'The intermediate stellar mass population in NGC 604 determined from Hubble Space Telescope images', *The Astrophysical Journal* **456**, 174.

Hunter, D. A., Baum, W. A., O'Neil Jr, E. J. & Lynds, R. (1996b), 'The Intermediate Stellar Mass Population in the M31 OB Association NGC 206', *The Astrophysical Journal* **468**, 633.

Jaschek, C. & Jaschek, M. (1957), 'The Mass Frequency-Function in Open Clusters', *Publications of the Astronomical Society of the Pacific* **69**(409), 337–341.

Kennicutt Jr, R. (1983), 'The rate of star formation in normal disk galaxies', *The Astrophysical Journal* **272**, 54–67.

Kroupa, P. (2001), 'On the variation of the initial mass function', *Monthly Notices of the Royal Astronomical Society* **322**(2), 231–246.
URL: *http://dx.doi.org/10.1046/j.1365-8711.2001.04022.x*

Kroupa, P. (2002), 'The initial mass function of stars: evidence for uniformity in variable systems', *Science* **295**(5552), 82–91.

Kroupa, P., Tout, C. A. & Gilmore, G. (1993), 'The distribution of low-mass stars in the galactic disc', *Monthly Notices of the Royal Astronomical Society* **262**(3), 545–587.

La Barbera, F., Ferreras, I. & Vazdekis, A. (2015), 'The initial mass function of early-type galaxies: no correlation with [mg/fe]', *Monthly Notices of the Royal Astronomical Society: Letters* **449**(1), L137–L141.

La Barbera, F., Ferreras, I., Vazdekis, A., de la Rosa, I., de Carvalho, R., Trevisan, M., Falcón-Barroso, J. & Ricciardelli, E. (2013), 'SPIDER VIII – constraints on the stellar initial mass function of early-type galaxies from a variety of spectral features', *Monthly Notices of the Royal Astronomical Society* **433**(4), 3017–3047.

La Barbera, F., Vazdekis, A., Ferreras, I., Pasquali, A., Allende Prieto, C., Röck, B., Aguado, D. & Peletier, R. (2016b), 'IMF and [Na/Fe] abundance ratios from optical and NIR spectral features in early-type galaxies', *Monthly Notices of the Royal Astronomical Society* **464**(3), 3597–3616.

La Barbera, F., Vazdekis, A., Ferreras, I., Pasquali, A., Cappellari, M., Martín-Navarro, I., Schönebeck, F. & Falcón-Barroso, J. (2016a), 'Radial constraints on the initial mass function from TiO features and Wing–Ford band in early-type galaxies', *Monthly Notices of the Royal Astronomical Society* **457**(2), 1468–1489.

Larson, R. B. & Tinsley, B. M. (1978), 'Star formation rates in normal and peculiar galaxies', *The Astrophysical Journal* **219**, 46–59.

Leier, D., Ferreras, I., Saha, P., Charlot, S., Bruzual, G. & La Barbera, F. (2016), 'Strong gravitational lensing and the stellar IMF of early-type galaxies', *Monthly Notices of the Royal Astronomical Society* **459**(4), 3677–3692.

Lequeux, J. (1979), 'Comparison of the Rates of Formation of Massive Stars and of the Initial Mass Functions in Galaxies of the Local Group', *Astronomy and Astrophysics* **71**, 1.

Luyten, W. (1941), 'The luminosity function', *Annals of the New York Academy of Sciences* **42**(1), 201–210.

Lyubenova, M., Martín-Navarro, I., van de Ven, G., Falcón-Barroso, J., Galbany, L., Gallazzi, A., García-Benito, R., González Delgado, R., Husemann, B., La Barbera, F. et al. (2016), 'IMF shape constraints from stellar populations and dynamics from CALIFA', *Monthly Notices of the Royal Astronomical Society* **463**(3), 3220–3225.

Martín-Navarro, I., Barbera, F. L., Vazdekis, A., Falcón-Barroso, J. & Ferreras, I. (2014), 'Radial variations in the stellar initial mass function of early-type galaxies', *Monthly Notices of the Royal Astronomical Society* **447**(2), 1033–1048.

Martín-Navarro, I., Vazdekis, A., La Barbera, F., Falcón-Barroso, J., Lyubenova, M., van de Ven, G., Ferreras, I., Sánchez, S., Trager, S., García-Benito, R. et al. (2015), 'IMF–METALLICITY: A TIGHT LOCAL RELATION REVEALED BY THE CALIFA SURVEY', *The Astrophysical Journal Letters* **806**(2), L31.

McConnell, N. J., Lu, J. R. & Mann, A. W. (2016), 'Radial trends in imf-sensitive absorption features in two early-type galaxies: Evidence for abundance-driven gradients', *The Astrophysical Journal* **821**(1), 39.

McDermid, R. M., Cappellari, M., Alatalo, K., Bayet, E., Blitz, L., Bois, M., Bournaud, F., Bureau, M., Crocker, A. F., Davies, R. L. et al. (2014), 'Connection between dynamically derived initial mass function normalization and stellar population parameters', *The Astrophysical Journal Letters* **792**(2), L37.

Miller, G. E. & Scalo, J. M. (1979), 'The initial mass function and stellar birthrate in the solar neighborhood', *The Astrophysical Journal Supplement Series* **41**, 513–547.

MUSE Pipeline Team (2017), *MUSE Pipeline User Manual (Version 0.15)*, ESO.

Oldham, L. & Auger, M. (2017), 'Galaxy structure from multiple tracers–III. Radial variations in M87âĂŹs IMF', *Monthly Notices of the Royal Astronomical Society* **474**(3), 4169–4185.

Parikh, T., Thomas, D., Maraston, C., Westfall, K. B., Goddard, D., Lian, J., Meneses-Goytia, S., Jones, A., Vaughan, S., Andrews, B. H. et al. (2018), 'SDSS-IV MaNGA: the spatially resolved stellar initial mass function in 400 early-type galaxies', *Monthly Notices of the Royal Astronomical Society* .

Posacki, S., Cappellari, M., Treu, T., Pellegrini, S. & Ciotti, L. (2014), 'The stellar initial mass function of early-type galaxies from low to high stellar velocity dispersion: homogeneous analysis of ATLAS3D and Sloan Lens ACS galaxies', *Monthly Notices of the Royal Astronomical Society* **446**(1), 493–509.

Ricciardelli, E., Vazdekis, A., Cenarro, A. & Falcón-Barroso, J. (2012), 'MIUSCAT: extended MILES spectral coverage–II. Constraints from optical photometry', *Monthly Notices of the Royal Astronomical Society* **424**(1), 172–189.

Rosani, G., Pasquali, A., La Barbera, F., Ferreras, I. & Vazdekis, A. (2018), 'The Influence of Galaxy Environment on the Stellar Initial Mass Function of Early-Type Galaxies', *Monthly Notices of the Royal Astronomical Society* .

Salpeter, E. E. (1955), 'The luminosity function and stellar evolution.', *The Astrophysical Journal* **121**, 161.

Salpeter, E. E. (2005), Introduction to IMF@ 50, *in* 'The Initial Mass Function 50 Years Later', Springer, pp. 3–10.

Sanchez-Blazquez, P., Peletier, R., Jiménez-Vicente, J., Cardiel, N., Cenarro, A. J., Falcon-Barroso, J., Gorgas, J., Selam, S. & Vazdekis, A. (2006), 'Medium-resolution Isaac Newton Telescope library of empirical spectra', *Monthly Notices of the Royal Astronomical Society* **371**(2), 703–718.

Sandage, A. (1957), 'Observational Approach to Evolution. I. Luminosity Functions.', *The Astrophysical Journal* **125**, 422.

Sarzi, M., Iodice, E., Coccato, L., Corsini, E., de Zeeuw, P., Falcón-Barroso, J., Gadotti, D., Lyubenova, M., McDermid, R., van de Ven, G. et al. (2018b), 'The Fornax3D project: overall goals, galaxy sample, MUSE data analysis and initial results', *arXiv preprint arXiv:1804.06795* .

Sarzi, M., Spiniello, C., La Barbera, F., Krajnović, D. & van den Bosch, R. (2018a), 'MUSE observations of M87: radial gradients for the stellar initial-mass function and the abundance of sodium', *Monthly Notices of the Royal Astronomical Society* **478**(3), 4084–4100.

Scalo, J. (1998), The IMF Revisited: A Case for Variations, *in* G. Gilmore & D. Howell, eds, 'The Stellar Initial Mass Function (38th Herstmonceux Conference)', Vol. 142 of *Astronomical Society of the Pacific Conference Series*, p. 201.

Scalo, J. M. (1986), 'The stellar initial mass function', *Fundamentals of cosmic physics* **11**, 1–278.

Schmidt, M. (1959), 'The rate of star formation.', *The Astrophysical Journal* **129**, 243.

Searle, L., Sargent, W. & Bagnuolo, W. (1973), 'The history of star formation and the colors of late-type galaxies', *The Astrophysical Journal* **179**, 427–438.

Searle, L. & Sargent, W. L. (1972), 'Inferences from the composition of two dwarf blue galaxies', *The Astrophysical Journal* **173**, 25.

Shields, G. & Tinsley, B. (1976), 'Composition gradients across spiral galaxies. II-The stellar mass limit', *The Astrophysical Journal* **203**, 66–71.

Smette, A., Sana, H., Noll, S., Horst, H., Kausch, W., Kimeswenger, S., Barden, M., Szyszka, C., Jones, A., Gallenne, A. et al. (2015), 'Molecfit: A general tool for telluric absorption correction-I. Method and application to ESO instruments', *Astronomy & Astrophysics* **576**, A77.

Smith, R. J. (2014), 'Variations in the initial mass function in early-type galaxies: a critical comparison between dynamical and spectroscopic results', *Monthly Notices of the Royal Astronomical Society: Letters* **443**(1), L69–L73.

Soto, K. T., Lilly, S. J., Bacon, R., Richard, J. & Conseil, S. (2016), 'ZAP–enhanced PCA sky subtraction for integral field spectroscopy', *Monthly Notices of the Royal Astronomical Society* **458**(3), 3210–3220.

Spiniello, C. (2016), The Low-Mass End of the Initial Mass Function in Massive Early-Type-Galaxies, *in* 'The Universe of Digital Sky Surveys', Springer, pp. 219–223.

Spiniello, C., Barnabè, M., Koopmans, L. & Trager, S. (2015b), 'Are the total mass density and the low-mass end slope of the IMF anticorrelated?', *Monthly Notices of the Royal Astronomical Society: Letters* **452**(1), L21–L25.

Spiniello, C., Napolitano, N., Coccato, L., Pota, V., Romanowsky, A. J., Tortora, C., Covone, G. & Capaccioli, M. (2015c), 'Vimos mosaic integral-field spectroscopy of the bulge and disc of the early-type galaxy ngc 4697', *Monthly Notices of the Royal Astronomical Society* **452**(1), 99–114.

Spiniello, C., Trager, S. C. & Koopmans, L. V. (2015a), 'The non-universality of the low-mass end of the IMF is robust against the choice of SSP model', *The Astrophysical Journal* **803**(2), 87.

Spiniello, C., Trager, S., Koopmans, L. & Chen, Y. (2012), 'Evidence for a mild steepening and bottom-heavy initial mass function in massive galaxies from sodium and titanium-oxide indicators', *The Astrophysical Journal Letters* **753**(2), L32.

Spiniello, C., Trager, S., Koopmans, L. V. & Conroy, C. (2014), 'The stellar IMF in early-type galaxies from a non-degenerate set of optical line indices', *Monthly Notices of the Royal Astronomical Society* **438**(2), 1483–1499.

Spinrad, H. (1962), 'Stellar populations in the nuclei of galaxies.', *The Astrophysical Journal* **135**, 715.

Spinrad, H. & Taylor, B. J. (1971), 'The stellar content of the nuclei of nearby galaxies. i. m31, m32, and m81', *The Astrophysical Journal Supplement Series* **22**, 445.

Strauss, M. A., Weinberg, D. H., Lupton, R. H., Narayanan, V. K., Annis, J., Bernardi, M., Blanton, M., Burles, S., Connolly, A., Dalcanton, J. et al. (2002), 'Spectroscopic target selection in the Sloan Digital Sky Survey: the main galaxy sample', *The Astronomical Journal* **124**(3), 1810.

Tinsley, B. M. (1977), 'Chemical evolution in the solar neighborhood. III-Time scales and nucleochronology', *The Astrophysical Journal* **216**, 548–559.

Tinsley, B. M. (1981), 'Chemical evolution in the solar neighborhood. IV-Some revised general equations and a specific model', *The Astrophysical Journal* **250**, 758–768.

Trager, S., Faber, S., Worthey, G. & González, J. J. (2000), 'The stellar population histories of local early-type galaxies. I. Population parameters', *The Astronomical Journal* **119**(4), 1645.

Trager, S., Worthey, G., Faber, S., Burstein, D. & González, J. J. (1998), 'Old stellar populations. VI. absorption-line spectra of galaxy nuclei and globular clusters', *The Astrophysical Journal Supplement Series* **116**(1), 1.

Treu, T., Auger, M. W., Koopmans, L. V., Gavazzi, R., Marshall, P. J. & Bolton, A. S. (2010), 'The initial mass function of early-type galaxies', *The Astrophysical Journal* **709**(2), 1195.

Trumpler, R. J. & Weaver, H. F. (1953), *Statistical astronomy*, Univ of California Press.

van den Bergh, S. (1957), 'The Luminosity Function of Population I.', *The Astrophysical Journal* **125**, 445.

van der Marel, R. P., Franx, M. et al. (1993), 'A new method for the identification of non-gaussian line profiles in elliptical galaxies', *Astrophysical Journal* **407**, 525.

van Dokkum, P., Conroy, C., Villaume, A., Brodie, J. & Romanowsky, A. J. (2017), 'The Stellar Initial Mass Function in Early-type Galaxies from Absorption Line Spectroscopy. III. Radial Gradients', *The Astrophysical Journal* **841**(2), 68.
URL: *http://stacks.iop.org/0004-637X/841/i=2/a=68*

van Dokkum, P. G. & Conroy, C. (2010), 'A substantial population of low-mass stars in luminous elliptical galaxies', *Nature* **468**(7326), 940–2.
URL: *https://www.ncbi.nlm.nih.gov/pubmed/21124316*

van Dokkum, P. G. & Conroy, C. (2012), 'The Stellar Initial Mass Function in Early-Type Galaxies from Absorption Line Spectroscopy. I. Data and Empirical Trends', *The Astrophysical Journal* **760**(1), 70.

van Rhijn, P. (1925), 'On the Frequency of the Absolute Magnitudes of the Stars', *Publications of the Kapteyn Astronomical Laboratory Groningen* **38**.

van Rhijn, P. J. (1936), 'The absorption of light in interstellar galactic space and the galactic density distribution', *Publications of the Kapteyn Astronomical Laboratory Groningen* **47**, 1–34.

Vaughan, S. P., Davies, R. L., Zieleniewski, S. & Houghton, R. C. (2017), 'Radial measurements of imf-sensitive absorption features in two massive etgs', *Monthly Notices of the Royal Astronomical Society* **475**(1), 1073–1092.

Vaughan, S. P., Davies, R. L., Zieleniewski, S. & Houghton, R. C. (2018), 'The stellar population and initial mass function of NGC 1399 with MUSE', *Monthly Notices of the Royal Astronomical Society* .

Vazdekis, A., Casuso, E., Peletier, R. & Beckman, J. (1996), 'A new chemo-evolutionary population synthesis model for early-type galaxies. i: Theoretical basis', *arXiv preprint astro-ph/9605112* .

Vazdekis, A., Coelho, P., Cassisi, S., Ricciardelli, E., Falcón-Barroso, J., Sánchez-Blázquez, P., Barbera, F. L., Beasley, M. & Pietrinferni, A. (2015), 'Evolutionary stellar population synthesis with miles–ii. scaled-solar and α-enhanced models', *Monthly Notices of the Royal Astronomical Society* **449**(2), 1177–1214.

Vazdekis, A., Koleva, M., Ricciardelli, E., Röck, B. & Falcón-Barroso, J. (2016), 'UV-extended E-MILES stellar population models: young components in massive early-type galaxies', *Monthly Notices of the Royal Astronomical Society* **463**(4), 3409–3436.

Vazdekis, A., Ricciardelli, E., Cenarro, A., Rivero-González, J., Díaz-García, L. & Falcón-Barroso, J. (2012), 'Miuscat: extended miles spectral coverage–i. stellar population synthesis models', *Monthly Notices of the Royal Astronomical Society* **424**(1), 157–171.

Vazdekis, A., Sánchez-Blázquez, P., Falcón-Barroso, J., Cenarro, A., Beasley, M., Cardiel, N., Gorgas, J. & Peletier, R. (2010), 'Evolutionary stellar population synthesis with MILES–I. The base models and a new line index system', *Monthly Notices of the Royal Astronomical Society* **404**(4), 1639–1671.

Villaume, A., Brodie, J., Conroy, C., Romanowsky, A. J. & van Dokkum, P. (2017b), 'Initial Mass Function Variability (or Not) among Low-velocity Dispersion, Compact Stellar Systems', *The Astrophysical Journal* **850**(1), L14.

Villaume, A., Conroy, C., Johnson, B., Rayner, J., Mann, A. W. & van Dokkum, P. (2017a), 'The extended IRTF spectral library: expanded coverage in metallicity, temperature, and surface gravity', *The Astrophysical Journal Supplement Series* **230**(2), 23.

Walcher, C. J., Coelho, P., Gallazzi, A. & Charlot, S. (2009), 'Differential stellar population models: how to reliably measure [Fe/H] and [α/Fe] in galaxies', *Monthly Notices of the Royal Astronomical Society: Letters* **398**(1), L44–L48.

Warner, B. (1961), 'The Initial Mass Function and the Occurrence of Stars of Small Mass', *Publications of the Astronomical Society of the Pacific* **73**(435), 439–445.

Weilbacher, P. M., Streicher, O. & Palsa, R. (2016), 'MUSE-DRP: MUSE Data Reduction Pipeline', *Astrophysics Source Code Library* .

Weilbacher, P., Streicher, O., Urrutia, T., Jarno, A., Pécontal-Rousset, A., Bacon, R., Böhm, P., Radziwill, N. & Chiozzi, G. (2012), Proc. SPIE Conf. Ser. Vol. 8451, Software and Cyberinfrastructure for Astronomy II, SPIE Bellingham.

Wielen, R. (1974), 'The kinematics and ages of stars in GlieseâĂŹs catalogue', *Highlights of Astronomy* **3**, 395–407.

Wing, R. F. & Ford Jr, W. K. (1969), 'The infrared spectrum of the cool dwarf Wolf 359', *Publications of the Astronomical Society of the Pacific* **81**, 527–529.

Worthey, G., Faber, S., Gonzalez, J. J. & Burstein, D. (1994), 'Old stellar populations. 5: Absorption feature indices for the complete LICK/IDS sample of stars', *The Astrophysical Journal Supplement Series* **94**, 687–722.

York, D. G., Adelman, J., Anderson Jr, J. E., Anderson, S. F., Annis, J., Bahcall, N. A., Bakken, J., Barkhouser, R., Bastian, S., Berman, E. et al. (2000), 'The Sloan Digital Sky Survey: Technical summary', *The Astronomical Journal* **120**(3), 1579.

Zieleniewski, S., Houghton, R. C. W., Thatte, N., Davies, R. L. & Vaughan, S. P. (2017), 'Radial gradients in initial mass function sensitive absorption features in the Coma brightest cluster galaxies', *Monthly Notices of the Royal Astronomical Society* **465**(1), 192–212.
URL: *http://dx.doi.org/10.1093/mnras/stw2712*